THE LEFT HAND OF ELECTROMAGNETISM: METAMATERIALS

A THESIS
SUBMITTED TO THE DEPARTMENT OF PHYSICS
AND THE INSTITUTE OF ENGINEERING AND SCIENCES
OF BILKENT UNIVERSITY
IN PARTIAL FULLFILMENT OF THE REQUIREMENTS
FOR THE DEGREE OF
DOCTOR OF PHILOSOPHY

By
Kamil Boratay ALICI
October, 2010

I certify that I have read this thesis and that in my opinion it is fully adequate, in scope and in quality, as a thesis for the degree of Doctor of Philosophy.

_____

Prof. Dr. Ekmel Özbay (Supervisor)

I certify that I have read this thesis and that in my opinion it is fully adequate, in scope and in quality, as a thesis for the degree of Doctor of Philosophy.

_____

Prof. Dr. Atilla Erçelebi

I certify that I have read this thesis and that in my opinion it is fully adequate, in scope and in quality, as a thesis for the degree of Doctor of Philosophy.

_____

Assoc. Prof. Dr. Vakur B. Ertürk

I certify that I have read this thesis and that in my opinion it is fully adequate, in scope and in quality, as a thesis for the degree of Doctor of Philosophy.

_____

Assoc. Prof. Dr. M. Özgür Oktel

I certify that I have read this thesis and that in my opinion it is fully adequate, in scope and in quality, as a thesis for the degree of Doctor of Philosophy.

_____

Assoc. Prof. Dr. Hamza Kurt

Approved for the Institute of Engineering and Sciences:

_____

Prof. Dr. Levent Onural
Director of Institute of Engineering and Sciences

ABSTRACT

THE LEFT HAND OF ELECTROMAGNETISM: METAMATERIALS

Kamil Boratay ALICI
PhD in Physics
Supervisor: Prof. Dr. Ekmel Özbay

October, 2010

Metamaterials are artificial periodic structures whose electromagnetic response is solely dependent on the constituting unit cells. In the present thesis, we studied unit cell characteristics of metamaterials that has negative permeability and permittivity. We investigated negative permeability medium elements, especially in terms of their electrical size and resonance strength. Experimental and numerical study of μ-negative (MNG) materials: multi split ring resonators (MSRRs), spiral resonators (SRs) and multi-spiral resonators are presented. The resonance frequency of the structures is determined by the transmission measurements and minimum electrical size of $\lambda_0/17$ for the MSRRs and of $\lambda_0/82$ for the SRs observed. We explain a method for tuning the resonance frequency of the multi-split structures. We investigated scalability of MNG materials and designed a low loss double negative composite metamaterial that operates at the millimeter wave regime. A negative pass-band with a peak transmission value of -2.7 dB was obtained experimentally at 100 GHz. We performed transmission based qualitative effective medium theory analysis numerically and experimentally, in order to prove the double negative nature of the metamaterial. These results were supported by the standard retrieval analysis method. We confirmed that the effective index of the metamaterial was indeed negative by performing far field angular scanning measurements for a metamaterial prism. Moreover, we illuminated the split-ring resonator based metamaterial flat lens with oblique incidence and observed from the scanning experiments, the shifting of the beam to the negative side. The first

device was a horn antenna and metamaterial lens composite whose behavior was similar to Yagi-Uda antenna.

We numerically and experimentally investigated planar fishnet metamaterials operating at around 20 GHz and 100 GHz and demonstrated that their effective index is negative. The study is extended to include the response of the metamaterial layer when the metamaterial plane normal and the propagation vector are not parallel. We also experimentally studied the transmission response of a one dimensional rectangle prism shaped metamaterial slab for oblique incidence angles and confirmed the insensitivity of split-ring resonator based metamaterials to the angle of incidence. After the demonstration of complete transmission enhancement by using deep subwavelength resonators into periodically arranged subwavelength apertures, we designed and implemented a metamaterial with controllable bandwidth.

The metamaterial based devices can be listed under the categories of antennas absorbers and transmission enhancement. We studied electrically small resonant antennas composed of split ring resonators (SRR) and monopoles. The electrical size, gain and efficiency of the antenna were $\lambda_0/10$, 2.38 and 43.6%, respectively. When we increased the number of SRRs in one dimension, we observed beam steerability property. These achievements provide a way to create rather small steerable resonant antennas. We also demonstrated an electrically small antenna that operates at two modes for two perpendicular polarizations. The antenna was single fed and composed of perpendicularly placed metamaterial elements and a monopole. One of the metamaterial elements was a multi split ring resonator and the other one was a split ring resonator. When the antenna operates for the MSRR mode at 4.72 GHz for one polarization, it simultaneously operates for the SRR mode at 5.76 GHz, but for the perpendicular polarization. The efficiencies of the modes were 15% and 40% with electrical sizes of $\lambda/11.2$ and $\lambda/9.5$. Finally, we experimentally verified a miniaturization method of circular patch antennas. By loading the space between

the patch and ground plane with metamaterial media composed of multi-split ring resonators and spiral resonators, we manufactured two electrically small patch antennas of electrical sizes $\lambda/3.69$ and $\lambda/8.26$. The antenna efficiency was 40% for the first mode of the multi-split ring resonator antenna with broad far field radiation patterns similar to regular patch antennas.

We designed, implemented, and experimentally characterized electrically thin microwave absorbers by using the metamaterial concept. The absorbers consist of i) a metal back plate and an artificial magnetic material layer; ii) metamaterial back plate and a resistive sheet layer. We investigated absorber performance in terms of absorbance, fractional bandwidth and electrical thickness, all of which depend on the dimensions of the metamaterial unit cell and the distance between the back plate and metamaterial layer. As a proof of concept, we demonstrated a $\lambda/4.7$ thick absorber of type i), with a 99.8% absorption peak along with a 8% fractional bandwidth. We have also demonstrated experimentally a $\lambda/4.7$ and a $\lambda/4.2$ thick absorbers of type ii), based on SRR and MSRR magnetic metamaterial back plates, respectively. The absorption peak of the SRR layout is 97.4%, while for the MSRR one the absorption peak is 98.4%. We conveyed these concepts to optical frequencies and demonstrated a metamaterial inspired absorber for solar cell applications.

We finalized the study by a detailed study of split ring resonators at the infrared and visible band. We studied i) frequency tuning, ii) effect of resonator density, iii) shifting magnetic resonance frequency by changing the resonator shape, iv) effect of metal loss and plasma frequency and designed a configuration for transmission enhancement at the optical regime. By using subwavelength optical split ring resonator antennas and couplers we achieved a 400-fold enhanced transmission from a subwavelength aperture area of the electrical size $\lambda^2/25$. The power was transmitted to the far field with 3.9 dBi directivity at 300 THz.

Keywords: Metamaterial, Antenna, Absorber, Solar Cell, Miniaturization, Multiple Split Ring Resonator, Spiral Resonator, Multiple Spiral Resonator, Negative Permittivity, Negative Permeability, Negative Refraction, Planar Metamaterial, Oblique Response, Split Ring Resonator Antenna, Dual Band Antenna, Electrically Thin Absorber, Photonic Metamaterial.

ÖZET

ELEKTROMANYETİĞİN SOL ELİ: METAMALMEZELER

Kamil Boratay ALICI
Fizik Bölümü, Doktora
Tez Yöneticisi: Prof. Dr. Ekmel Özbay
Ekim 2010

Metamalzemeler elektromanyetik özellikleri onları oluşturan birim hücrelere bağlı olan periyodik yapay yapılardır. Bu tezde, ilk olarak metamalzemelerin negatif permeabilite ve negatif permitivite birim hücre özelliklerini inceledik. Negatif permeabilite sağlayan birim hücreleri özellikle elektriksel boyut ve rezonans gücü açılarından araştırdık. Çoklu yarıklı halka rezonatörlerinin (MSRR) ve sarmal rezonatörlerin (SR) deneysel ve sayısal çalışmasını sunduk. İletim ölçümlerinden bu yapıların rezonans frekansını belirledik ve SR'lar için $\lambda_0/82$, MSRR'lar için $\lambda_0/17$ minimum elektriksel boyutları elde ettik. Bu ölçümlerde λ_0 serbest uzay dalga boyunu ifade etmektedir. Çok yarıklı yapılar için rezonans frekansını ayarlama yöntemi keşfettik. Çifte negatif kompozit metamalzemelerin ölçeklenebilirliğini kullanarak bu yapıları milimetre dalgaboyunda düşük kayıpla çalışır halde tasarladık ve ölçtük. Geçirgen banttaki zirve değeri -2,7 dB olan ve 100 GHz'de çalışan yapıları deneysel olarak gösterdik. Çifte negatif özelliği kanıtlamak için sayısal ve deneysel olarak iletim tabanlı etkisel ortam kuramını uyguladık. Bu sonuçları standart alım analizi ile destekledik. Prizma şeklindeki bir metamalzeme yapıp etkin kırınım indeksinin açısal tarama ölçümleri ile negatif olduğu doğruladık. Dahası, yarıklı halka rezonatör tabanlı düz bir metamalzemeyi eğik açıyla aydınlatıp iletilen gücü tarama deneyleri ölçerek ışığın negatif tarafa kırıldığını gözlemledik. Son olarak bu düz metamalzemeyi boynuz antenin önüne koyduğumuzda davranışının Yagi-Uda antene benzer olduğunu gördük.

Sayısal ve deneysel olarak düzlemsel balık ağı metamalzemelerini yaklaşık 20 GHz ve 100 GHz'de çalıştığını gösterdik ve onların etkin kırınım indislerinin negatif olduğunu kanıtladık. Çalışmamız metamalzeme tabakaları ile yayılma vektörünün paralel olmadığı durumu da içermektedir. Eğik açılarla gelen dalgalar için yarıklı halka rezonatörü temelli metamalzemelerin yanıtı değişmemektedir. Ayrıca dalga boyu altı boyutlu periyodik deliklerden geçen güç dalga boyu altı rezonatörler kullanılarak arttırıldı ve tam iletim sağlanabileceği gösterildi.

Metamalzeme tabanlı cihazlar, antenler, soğurucular ve arttırılmış iletim yapıları olarak sıralanabilir. Elektriksel olarak küçük, yarıklı halka rezonatörü ve tel antenden oluşan antenler tasarladık. Bu antenlerin elektriksel boyutu, kazancı ve verimliliği sırasıyla $\lambda_0/10$, 2.38 ve % 43.6 idi. Bu antendeki yan yana dizilmiş SRR sayısı arttığında yaydığı radyasyonun yönü de değişmektedir. Bu küçük antenler fazlı dizi antenlerinin birim elemanı olarak kullanılabilir. Ayrıca, iki çoklu halka rezonatörü birbirine dik konumda kullanarak iki değişik frekansta ve polarizasyonda çalışan bir elektriksel olarak küçük anten gösterdik. Bu anten bir polarizasyon için 4.72 GHz'de diğer polarizasyon için 5.76 GHz'de çalışmaktadır. Verimliliği ise sırasıyla % 15 ve % 40, elektriksel boyutu ise sırasıyla $\lambda/11.2$ ve $\lambda/9.5$'tur. Son olarak, yuvarlak yama antenlerini minyatürleştirmek için bir yöntem gösterdik. Bu antendeki yama ve toprak düzlemi arasındaki boşluğa rezonatörleri dizerek $\lambda/3.69$ ve $\lambda/8.26$ elektriksel boyuta sahip yama antenler gösterdik. Bu antenin radyasyon yayılımı, normal yama anteninkine benzerken boyutu daha küçük ve verimi % 40'tır.

Metamalzemelerin küçük elektriksel boyutlarından faydalanarak ince mikrodalga radyasyon soğurucular tasarladık. Bu soğurucular i) metal bir arka plaka ve yapay bir manyetik metamalzeme tabakasından, ii) metamalzeme arka plaka ve dirençli sac tabakadan oluşur. Soğurucu performansını çalıştığı kesirli bant genişliği ve elektriksel kalınlığı açılarından inceledik. Tip i) soğurucu için

% 8 kesirli bant genişliği ve % 99.8 tepe soğurma değeri olan λ/4.7 kalınlıkta bir soğurucu gösterdik. Kullanılan rezonatörün elektriksel boyutuna bağlı olarak soğurucu kalınlığı değişmektedir. Bu kavramlar optik frekanslar için de geçerlidir ve güneş pili gibi birçok uygulama için ümit vericidir.

Periyodik yarıklı halka rezonatörleri kızılötesi ve görünür bantlarda da çalışılabilir. Biz bu çalışmada i) rezonatör şeklini değiştirerek manyetik rezonans frekansının değiştiğini, ii) periyodik dizilimde rezonatör yoğunluğunun etkisini iii) metal kaynaklı kayıpları ve metal plazma frekansının etkisini gösterdik. Optik rejimde arttırılmış iletim için dalga boyu altı yarıklı halka rezonatör antenleri ve kuplörleri kullanarak elektriksel boyutu $\lambda^2/25$ olan bir delikten 400 kat arttırılmış iletim elde ettik. Bu güç uzak alana 300 THz frekansta 3.9 dBi yönlülük ile aktarılmaktadır.

Anahtar Kelimeler: Metamalzeme, Anten, Soğurucu, Solar Hücre, Minyatür çoklu yarıklı halka rezonatörü, Sarmal rezonatör, Çoklu Sarmal rezonatör, Negatif kırınım indisi, Negatif Kırılma, Düzlemsel Metamalzeme, Eğik açıyla gelen ışık durumu, yarıklı halka rezonatör Anteni, Dual Bant Anten, Elektriksel olarak ince soğurucu , fotonik Metamalzeme.

Acknowledgements

I would like to thank Prof. Dr. Ekmel Özbay for his great patience and excellent guidance throughout my PhD study.

I would like to thank to The Scientific and Technological Research Council of Turkey (TUBITAK) for awarding me with the graduate scholarship.

I would like to thank to the members of my thesis committee, Assoc. Prof. Dr. Vakur B. Ertürk, Assoc. Prof. Dr. Mehmet Özgür Oktel, Assoc. Prof. Dr. Hamza Kurt, and Prof. Dr. Atilla Erçelebi for reading the manuscript and commenting on the thesis.

I would like to thank to Advanced Research Laboratory staff, Physics Department Laboratory staff and Nanotechnology Research Center group members who had a positive effect on my research.

I would like to thank my friends Serkan Bütün for fruitful scientific discussions and Onur Atuğ for listening my complaints throughout the graduate study.

I would like to thank to my parents, my sister and especially my fiancée for her great support without which I could not be successful.

Table of Contents

List of Figures

List of Tables

Chapter 1

Introduction

Electromagnetism plays a major role in today's technology from radio waves to X-Rays. The basics of information and communication technology (ICT) depend on the developments in the electromagnetism. It started with low frequency radio waves, television broadcasts, radar and continued with cell phones and wide bandwidth information transfer. The operation frequencies of ICT devices cover almost all bands of the electromagnetic spectrum from KHz to THz frequencies. On the other hand, at the infrared and optical regime the light emitting and absorbing semiconductor devices play a critical role. The detector and display technologies are improving quite fast. The field of photovoltaic devices is one of the most promising green energy harvesting tools. However, it was recently noted that all these electromagnetic devices are using half of the possible electromagnetic medium i.e. the propagation in these media is right handed. The electric field, magnetic field and wave vector constitute a right handed coordinate system that limits the control of fundamental device properties. Another possible medium is left handed that excited many researchers and named it as metamaterial meaning a material that has properties beyond the limits of the right handed material.

Metamaterials utilize the magnetic resonance frequency to obtain negative permeability at any frequency band of the electromagnetic spectrum. The common unit cell is the split ring resonator that was first proposed by Pendry et al. in 1999. Since then negative permeability medium elements became a very important part of the metamaterial study and supplied very important characteristics for transmission, reflection, refraction and absorption based devices. Later researchers developed the double negative medium in which the propagation of the electromagnetic wave constitutes a left-handed system. The exciting properties of this media are negative index of refraction, negative phase velocity, reversed Cherenkov radiation and Doppler Effect.

Today metamaterial concepts started to be used to create new devices such as electromagnetic cloaks and to increase the current performance of radiation sources and absorbers. Utilization of metamaterial theory enables us to design and implement devices for specific purposes with desired control of wave propagation.

1.1. Outline of this thesis

In this thesis, we studied metamaterial elements and demonstrated unusual phenomena such as negative refraction, negative phase velocity, miniaturization of antennas, novel thin absorbers and enhanced transmission.

In chapter 2, we have studied limits of electrically small negative permeability medium particles. We demonstrated how increasing the side length of the particles and using higher permittivity substrates affects the electrical size. On the other hand, we also studied the resonance strength of these particles. We analyzed a novel particle: the multi-spiral resonator in terms of resonance strength and electrical size. Our particles are low profile and can be easily packed into three-dimensional arrays for antenna, superlens and absorber applications. We explained a method for digitally tuning the resonance

frequency of the multi split structures. Finally, we have demonstrated that by inserting deep subwavelength resonators into periodically arranged subwavelength apertures complete transmission enhancement can be obtained at around the magnetic resonance frequency. Even though periodically arranged metallic resonators can produce a negative permeability medium, the resonant response weakens at extreme regimes under certain conditions, which is the major problem of obtaining a negative index at the visible regime. We report that by decreasing the operation temperature, the metal conductivity can be increased, enhanced negative permeability can be obtained and the operation range of the negative permeability media, and thereby the negative index media, can be extended.

In chapter 3, we characterized split ring resonator-based metamaterial operating at 100 GHz by using transmission based qualitative effective medium theory and standard retrieval analysis. We analyzed transmission response for increasing the number of layers at the propagation direction. We observed a stop-band for the SRR-only medium and pass-band for the CMM medium at around 100 GHz. We studied radiation of horn antenna and metamaterial slab composite at the far field both numerically and experimentally. By constructing a metamaterial prism and performing angular scan experiments we confirmed the retrieved negative index property of a split ring resonator based metamaterial. We confirmed by direct field scan measurements, a one-dimensional metamaterial lens that is designed to be double negative by using the qualitative effective medium theory, in which it indeed refracts the obliquely incident waves to the negative direction. The study was performed both experimentally and numerically at around 100 GHz.

In chapter 4, characterization of a planar metamaterial operating at 100 GHz is demonstrated in terms of the qualitative effective medium theory and the standard retrieval analysis. When the linear polarization of the incident field changes, the transmission data remains the same if the angle between the

structure plane and propagation vector is kept fixed. This is due to the x-y plane symmetric design of the metamaterial. We also characterized a planar metamaterial operating at 21 GHz by using a quantitative effective medium theory. The planar metamaterial was the fishnet structure, which is symmetric with respect to the $x = \pm y$ plane. The operation frequency of the fishnet metamaterial is higher than the corresponding cut-wire pair magnetic resonance frequency. The left-handed nature of the transmission peak is identified unambiguously by using the shorted CMM structure. The experimental phase data strengthens the indication of the negative index of refraction. By investigating the planar metamaterials at microwave frequencies several contributions can be added to the study of metamaterials at optical frequencies.

In chapter 5, we demonstrated the fishnet metamaterial case for which the incidence angle is nonzero. The response of the medium changes very quickly as we increase the angle of incidence. We also systematically studied a three-layered SRR-based metamaterial slab oblique response and showed that the negative index characteristics remain nearly the same up to incidence angle of 45°. The negative transmission band remained almost the same for two different bases of rotation. The insensitivity of SRR based metamaterials to the angle of incidence makes them a good candidate for metamaterial applications especially the superlens.

In chapter 6, we studied resonant antennas with efficiencies exceeding 40% by electrically exciting the SRRs placed on a ground plane. The sizes of the antenna were less than $\lambda_0/10$. We studied the fundamental limits of metamaterial loaded ESAs. We show that when excited properly, SRRs above a ground plane radiate efficiently. These results can have applications in future wireless systems and in the development of the steerable phased array antennas. Secondly, by introducing multi-SRRs we can observe the antenna beam direction shifts. This property might lead us to steerable antennas that are composed of SRRs. By electrically exciting two perpendicularly placed SRRs with different electrical

sizes, we were able to obtain an electrically small, single fed, resonant antennas. The dual polarization nature of this antenna enables operation for the two modes at perpendicular polarization states. This antenna has applications as a single receiver element or a unit cell element of a metamaterial based phased array antenna. We also studied electrically small single layer metamaterial loaded patch antennas. These results constitute proof for the usefulness of metamaterial concepts in the antenna miniaturization problem. An MSRR medium loaded antenna has been studied. We demonstrated that by loading the patch via an SR medium, a further miniaturization is possible. This miniaturization technique is potentially promising for antenna applications. However, rather sophisticated fabrication and characterization facilities are needed in order to demonstrate the limits of these antennas.

In chapter 7, we showed that the concept of metamaterials has proven to be useful in yet another field of microwave engineering, i.e. microwave absorbers. For a metal backed metamaterial absorber, we demonstrated the relation between the electrical thickness and the absorbance peak. The origin of the absorbance was proven to be the magnetic resonance of the constituting artificial magnetic material inclusions. For approximately $\lambda/5$ of total electrical thickness, we achieved an almost perfect absorption with a *8%* fractional bandwidth by using SRR of $\lambda/10$ electrical size. As we used metamaterial elements of a smaller electrical size, such as MSRR, we were able to reduce the absorber thickness accordingly. Moreover, we demonstrated another type of absorber: a metamaterial backed resistive sheet. Almost perfect absorbance was also achieved for this case, with $\lambda/5$ total electrical thickness and *8%* fractional bandwidth. These proofs of concepts may open the door to a) even more miniaturized microwave absorbers, employing deeply sub-wavelength magnetic inclusions and b) tunable devices employing either externally controlled capacitors connected to the magnetic resonators or light-induced conductivity changes of the material filling the splits of the SRR and MSRR.

In chapter 8, we clearly demonstrated the possible effects of split ring resonator orientations on the transmission response at the optical regime. Depending on the application, a different orientation and correspondingly different modes can be utilized. For a densely packed split ring resonator array, a stronger coupling yielded an increased the fractional bandwidth of the magnetic stop band, as well as an increased the resonance strength. When the split ring resonators were loosely packed, the response was very weak and very similar to that in a single resonator case. The magnetic resonance frequency was strongly dependent on the parameter: arm length (L) of the split ring resonators. A slight change in the arm length leads to a significant shift of the magnetic resonance frequency. The resonant behavior of metamaterials at the optical regime strongly depends on the characteristics of the utilized metal.

We incorporated the split ring resonators in the numerical domain to provide an alternative solution to the problem of enhanced transmission. Compared to the previously demonstrated results, we obtained a 31 times larger enhancement from a 2000 times smaller radiating aperture area. Furthermore, the fields were radiated to the far field with 3.9 dBi directivity, which is suitable for real world applications at the optical regime.

Finally, we demonstrated metamaterial incorporated absorber configurations operating at the optical regime. For a metal backed metamaterial absorber, we demonstrated the relation between the electrical thickness and the absorbance peak. The origin of the absorbance was proven to be the magnetic resonance of the constituting artificial magnetic material inclusions. For approximately $\lambda/6$ of total electrical thickness, we achieved an almost full absorption with a 42% fractional bandwidth by using subwavelength SRRs. As a proof of concept, we demonstrated a composite absorber with 185 nm thickness and obtained minimum 90% absorption between 1078 nm to 2183 nm free space wavelengths. As the next step we demonstrated a design that is polarization independent and wider bandwidth that composed of an electrical screen in addition to the present magnetic metamaterial screen. We finalized the analysis by demonstrating the oblique response of the superior absorber design. We observed up to 60°

incidence angle the absorption remains above 70%. Utilization of magnetic resonance at the optical regime can have applications in various important areas such as photovoltaic thin film solar cells, military stealth technologies, thermal isolation, infrared photodetectors, and biosensors.

Chapter 2

Metamaterial Elements for Artificial Magnetism

2.1. Introduction

The fundamental parameters: electric permittivity (ε) and magnetic permeability (μ) of metamaterials can be controlled by specifying the shape and content of their periodically arranged elements. Metamaterial media can thereby have negative and near zero permeability (MNG, MNZ). Particles composed of non-magnetic metal and dielectric substrates were used as the unit cell of the metamaterials [1]. Shaped metallic resonators provided a negative permittivity medium around the resonance frequency (f_0) [2]. Metamaterials in the form of rectangular slab were realized by utilizing planar substrate based fabrication techniques such as printed circuit board technology [3], optical [4], deep x-ray [5], and e-beam lithography [6] techniques. The performance of current devices in the fields of radiation [7-12], reflection [13, 14], transmission [15-17], absorption, and refraction [18, 19] have been improved and novel devices such as electromagnetic cloak [20-23] have been invented as a consequence of the metamaterial study. In these applications, the subwavelength resonators provided the magnetic response and a rather small electrical size is of importance for the performance of the metamaterial loaded devices.

The most common negative permeability medium element is a split ring resonator (SRR): a metallic flat ring with a split etched on the substrate [1, 24]. The typical electrical size of the SRR is $\lambda_0/10$, where λ_0 is the free space wavelength at the magnetic resonance frequency. Loading an SRR gap with

lumped elements, especially capacitors, is one way to reduce its electrical size [25-27]. However, the synthesis of a negative permeability medium via capacitor loaded particles is a tedious procedure. Another method is to wind metal sheets as coils, by which an electrical size of $\lambda_0/68$ can be achieved as in the case of a 'Swiss Roll' structure [28]. The drawback of the Swiss Roll type and lumped element loaded resonators [29] is that it is rather difficult to realize their multi-dimensional arrays to compose a slab with negative permeability. Spiral resonators form a good example of the utilization of the available space with proper metal geometry [30-34]. These particles are well known in microwave engineering as lumped inductors [35].

In the present chapter, we studied electrically small negative permeability medium particles that can be fabricated via the standard planar substrate based fabrication techniques and can be packed into one-, two- and three- dimensional arrays for the metamaterial applications. The particles are multiple split ring resonators (MSRRs), spiral resonators (SRs), and multiple split spiral resonators (MSRs). The MSR states a compromise between the electrical size and resonant response strength. We investigated dependence of miniaturization factor on the physical parameters of the resonators. Furthermore, we discuss the size scalability of the particles to higher frequencies under the limitations of printed circuit board technology. We finalize the study by demonstrating a method for tuning the multi-split structures and, low temperature response of spiral resonators.

At this point, it is necessary to identify a standard for the determination of the size of the MNG materials. We follow a rather fundamental paper that discusses the theoretical limits of the antennas [36]. While defining the electrical size of a structure, we consider the minimum sphere that can enclose it. If the radius of the sphere is a, then the larger linear dimension of the structure is 2a. The electrical size (2a) is identified in terms of the free space wavelength (λ_0) at which the structure operates: $u = 2a/\lambda_0$. The calculated minimum radius (a) and

electrical size (u) of the miniaturized MNG materials in the literature are shown in Table 2.1.

	Swiss Roll	Cylindrical SRR	C. L. Loop	C. L. Ring	C. L. Double Sided Spiral	C. L. SRR
a (mm)	100.1	8.2	6.8	14.0	6.5	3.7
f_0 (MHz)	22.1	1440.0	60.0	46.2	156.4	990.0
u (λ_0)	1/68	1/13	1/367	1/232	1/148	1/41

Table 2.1. Comparison of the MNG materials in the literature in terms of electrical size (u), resonance frequency (f_0), and radius of the minimum sphere (a). The free space wavelength is denoted as λ_0. (Capacitance loaded is abbreviated as C. L.).

2.1.1. Experiment Setup

The resonant response of a single MNG material is measured by using two coaxial probe antennae operating at the reactive near field region as transmitter and receiver antennae. There are several reasons for preferring probe antennae over the loop antennae. We found using probe antennae is rather easy in terms of alignment and we obtained a better coupling to the resonators by using probe antenna. The sample is inserted into the space between the antennae, wherein we obtained the strongest response, as shown in Figure 2.1. First, we measure the transmission spectra of the free space, i.e. without the MNG material. We use this data for calibration and then repeat the experiment with the MNG material inserted. The distance between the receiver and transmitter probes is kept fixed during the measurements. There were absorbers placed under the sample and an Agilent N5230A or HP8510C Vector Network Analyzer was used during the experiments. At the magnetic resonance frequency of the particles, we observed a stop-band at the transmission spectra.

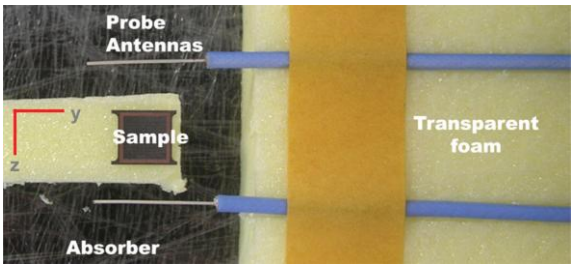

Figure 2.1. Single element free space transmission setup

2.1.2. Numerical Method

Resonance frequencies of the MNG materials are calculated numerically by using the commercial software CST MICROWAVE STUDIO. This tool is a three dimensional full-wave solver employing the finite integration technique [37]. We excite a layer of MNG materials with a plane wave and obtain the transmission amplitudes. In our calculations, the B-field was at the x-direction, the E-field was at the y-direction, and the propagation direction was at the –z-direction. Dip of the transmission data gives an estimate of the resonance frequency of the structure. The structure shows the μ-negative behavior at around the resonance frequency.

2.2. Multiple Split Ring Resonators

The geometry and parameters of the MSRR particle are shown in Figure 2.2(a). The substrate used in our particles was Rogers RT/Duroid 5880 with ε_r = 2.0 and tanδ = 0.0009. The thickness of the substrate, t = 254 μm and deposited copper thickness, h = 9 μm. The MSRR parameters were as follows: width of the strips, w = 100 μm, separation between the strips, s = 100 μm, the split width, g = 100 μm, side length of the particles varies from l = 2.4 mm to l = 8.0 mm, and number of rings varies from N = 5 to N = 20. In Figure 2.2, we show how the resonant response and electrical size change as we change the side length and the number of rings of the MSRRs, simultaneously. We observed that

as we increase the side length via adding new rings to the particle, the operation frequency decreases, as shown in Figure 2.2(c). This result was expected because the increase of physical size decreases the operation frequency in general. On the other hand, the results shown in Figure 2.2(d) demonstrated that the electrical size also reduced. These results are in good agreement with the numerical calculations and can be explained by using the quasi-static LC-circuit models as developed in the theoretical paper of Bilotti et al. [33, 38]. In Figure 2.2(b), the resonant response of the MSRRs are shown, in which we obtained quite strong responses and the average of the dip values was on the order of -35 dB. As to the MSRRs, multiple resonances can be seen. However, higher order modes are not under interest for metamaterial related applications since the first magnetic resonance mode provides us the smallest electrical size. In addition, the more we go up in frequency, the electrically larger are the inclusions and, thus, they are not useful anymore as building blocks of metamaterials. Since these structures were composed of discrete elements such as splits, rings and gaps, it was not possible to change their parameters such as side length, number of rings, strip width and separation between the strips, independently. Thereby, we studied several possible parameter changes that are linked to each other.

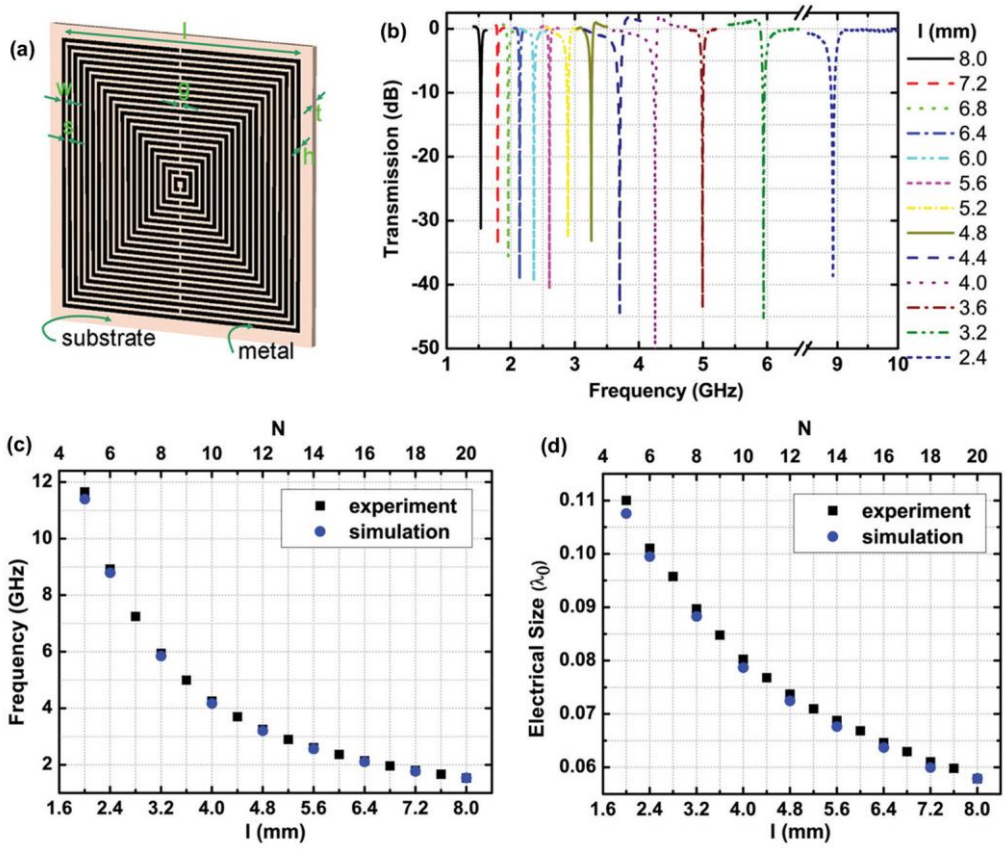

Figure 2.2. The multi-split ring resonator (MSRR) response (a) Geometry of the multi-split ring resonator (MSRR), l = 8 mm, w = s = g = 100 µm, h = 9 µm, t = 254 µm. (b) Experimental transmission data as a function of the frequency. (c) Resonance frequency (d) Calculated electrical size as a function of the simultaneously changing N and l.

2.3. Spiral Resonators

We also studied the effect of changing the side length and number of turns for the spiral resonators, whose schematic is shown in Figure 2.3(a). Similar to the MSRR behavior: as we increased the number of turns the operation frequency decreased and the electrical size also reduced. In Figures. 2.3(c) and 2.3(d), after some point the miniaturization factor saturates i.e. adding more turns does not lead to a much smaller electrical size. The miniaturization factor for SRs is larger than MSRRs. The drawback of SRs is that we did not see a strong

resonant response. As shown in Figure 2.3(b), the minima of the stop-bands are on the order of -2.5 dB on average, which is due to the long length of the metal strips with respect to the operation wavelength. This drawback encouraged us to investigate a novel resonator: multi-spiral resonator (MSR). According to the theory developed in Ref [33], the magnetic inclusion can be represented as an RLC series circuit. Therefore, the related quality factor is given by the equation: $Q=\left(\sqrt{L/C}\right)/R$. R accounts for the losses in the material. In the case of the SR, the strip is much longer and the related ohmic losses are quite high. In addition, the capacitance C is higher than in the case of any other resonator here presented. Consequently, the resonance of the SR is expected to be less pronounced if compared to the one of the MSRR. Another way around to see this is to write the quality factor, by definition, as $Q=w_0\left(P_{stored}/P_{diss}\right)=w_0\left(L/R\right)$. Once we substitute $w_0=1/\sqrt{LC}$ we get the previous expression. Anyhow, in this form, it is clear that the lower is the resonance frequency, the less pronounced is the resonance. The effect of losses, then, further lowers the resonance strength.

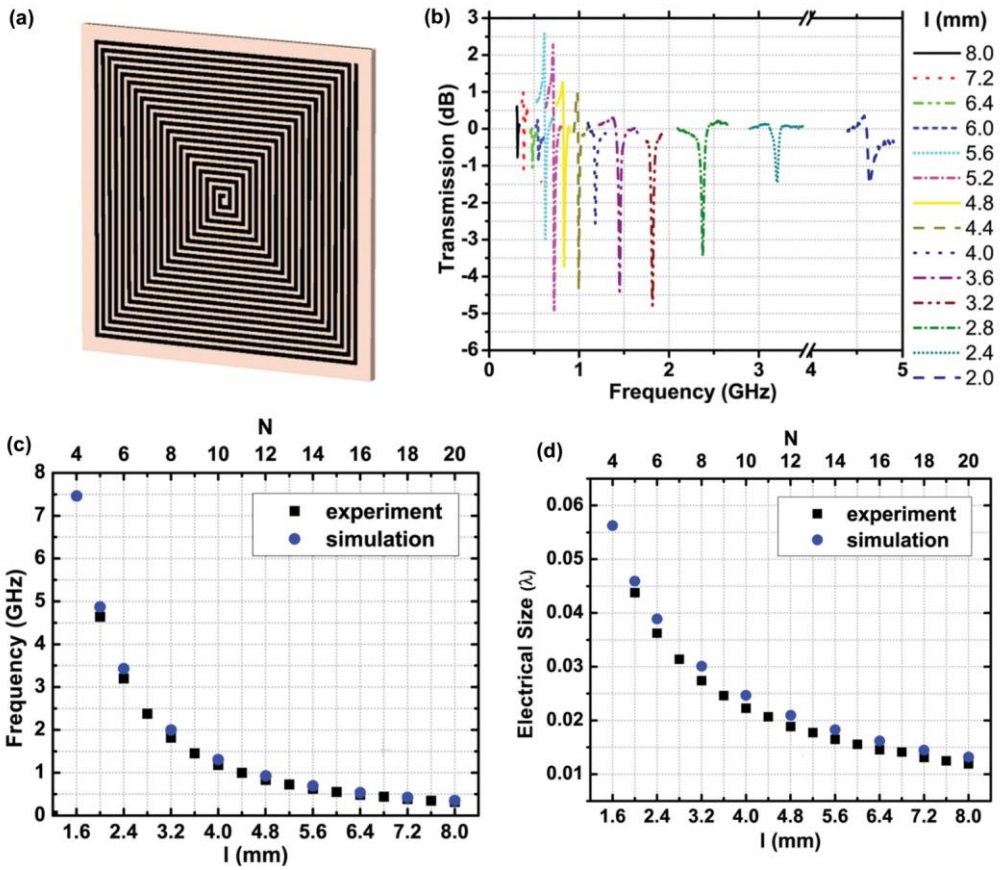

Figure 2.3. The spiral resonator (SR) response (a) Geometry of the spiral resonator (SR), l = 8 mm, w = s = 100 µm, h = 9 µm, t = 254 µm. (b) Experimental transmission data as a function of the frequency. (c) Resonance frequency (d) Calculated electrical size as a function of the simultaneously changing N and l.

2.4. Multi-Spiral Resonators

We introduced several splits to the SRs to increase the strength of the resonant response. We fabricated six examples, which are shown in Figure 2.4. We introduced one split to the SR particle with N = 20 and l = 8 mm, and changed the position of the split as shown in Figures 2.4(a)-2.4(c). We increased the number of the splits to 4, as shown in Figure 2.4(d). However, for these particles the resonant strength was similar to the corresponding SR particle, and we did

not observe a significant increase in the resonance strength. We continued in this fashion and obtained the particles as shown in Figures 2.4(e) and 2.4(f) for which a much stronger resonance strength was obtained. The MSR shown in Figure 2.4(f) is similar to MSRR shown in Figure 2.2(a) geometrically. In this MSR structure, we had a split at every turn similar to the MSRR. As expected the resonance frequency of this structure is almost the same as the MSRR with the same l, N, s and w parameters. The shift at the resonance frequency of the multi-spiral resonator that is shown in Figure 2.4(e) is acceptable and it constitutes a good trade-off between the resonance strength and electrical size. Its side length, l = 8 mm and resonance frequency, f_0 = 0.81 GHz, electrical size, u = $\lambda_0/30$, and stop-band minimum is -27 dB. This particle is low profile and easy to fabricate, and thereby it is a good candidate for metamaterial applications.

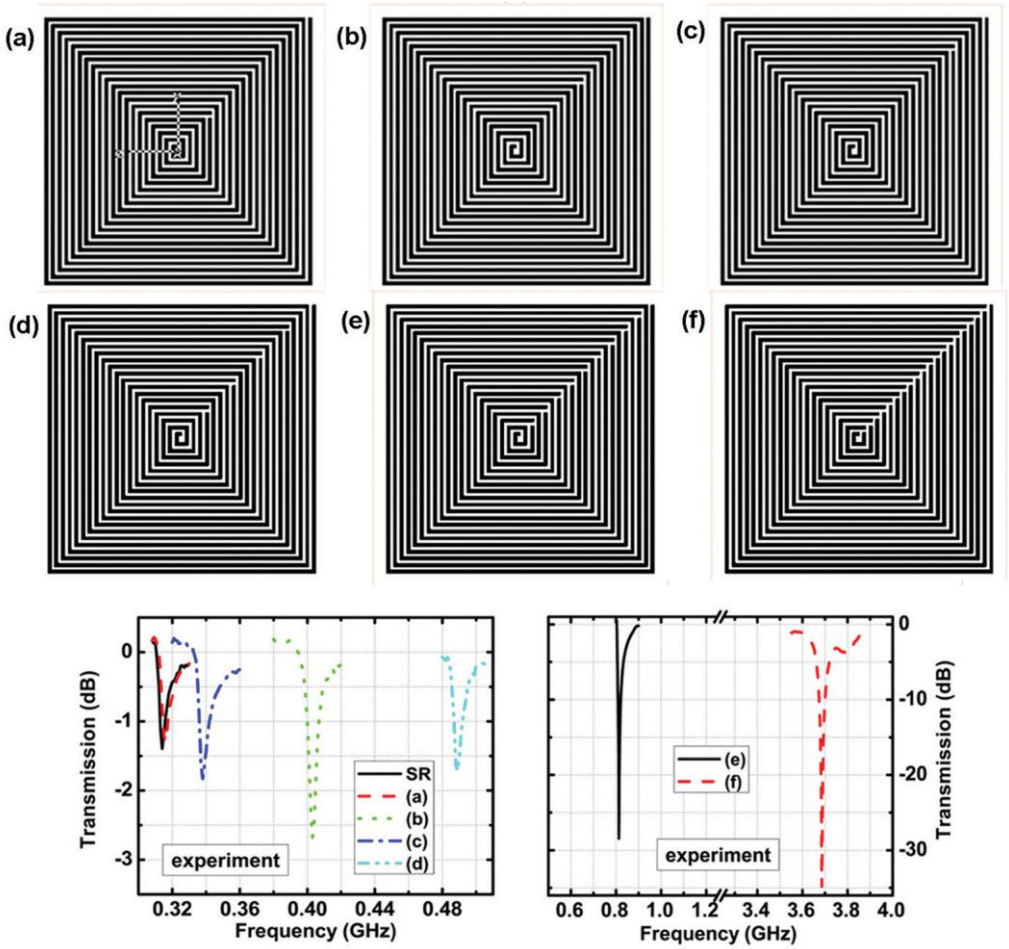

Figure 2.4. The multi-spiral resonator (MSR) response. Geometry of the particles analyzed (top). Experimental transmission data of each resonator as a function of frequency (bottom).

2.5. Effect of Resonator Parameters on the Electrical Size

The experimental and numerical results are shown in Figure 2.5 and Figure 2.6. For the MSRR and SR materials, as we increase the number of rings or number of turns, the resonance frequency shifts towards smaller values. The miniaturization factor for the SRs is higher than the MSRRs. In Figure 2.6, we see that increasing the number N above a critical point does not reduce the

resonance frequency any more. The resonance frequency of the MSRR can be significantly reduced up to 4-5 rings (N = 5). From Figure 2.6 we conclude that it is not necessary to completely fill the inner part of the SR in order to obtain a good reduction of the resonance frequency. Similar to the case of the MSRR, we see that after some point, increasing the number N does not affect the resonance frequency. The calculated electrical size (u), radius of the minimum sphere (a), and resonance frequency (f_0) for the optimum structures are shown in Table 2.1. The reduction of the resonance frequency is comparable with the examples found in the literature. The MNG materials are relatively easy to fabricate, low profile and thereby can be packed into arrays in several dimensions. For the two MSRR examples, we see that increasing the number of rings can reduce the electrical size. This principle is also valid for the SRs. Moreover, using a higher permittivity substrate will lead us to the further reduction of the resonance frequency. These results can be explained by the aid of theoretical analysis and modeling of the SRs in literature [39]. Moreover, a detailed analysis and circuit model of our structures is given in Ref. [38].

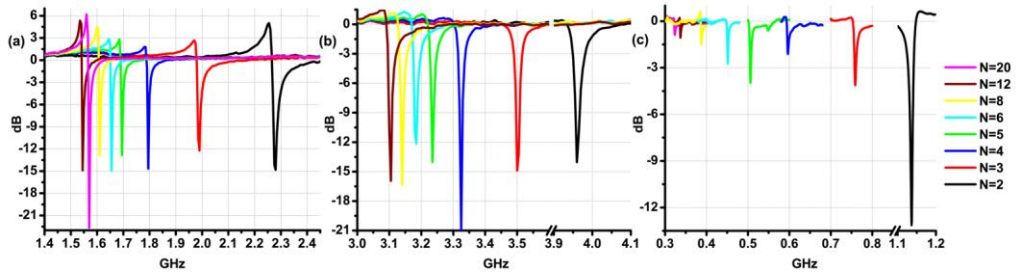

Figure 2.5. Experimental transmission data as a function of the frequency (a) Multi split ring resonators with the side length l = 8 mm. (b) Multi split ring resonators with the side length l = 5 mm. (c) Spiral resonators with the side length l = 8 mm.

The incident electromagnetic wave induces current on the resonators. At the resonance frequency the electric and magnetic energy in the structure increases dramatically. Since the structures are small compared to the wavelength, the results can be explained by a quasi-static approach. We consider the change of

the total inductance (L) and capacitance (C) of the structures as the number of rings or turns increases. The significant parameters to determine the L and C are the average length of the strips and their filling ratio [38]. There are three important results to be explained: the decrease of the resonance frequency, miniaturization factor difference between the MSRR and SR structures, and the saturation behavior.

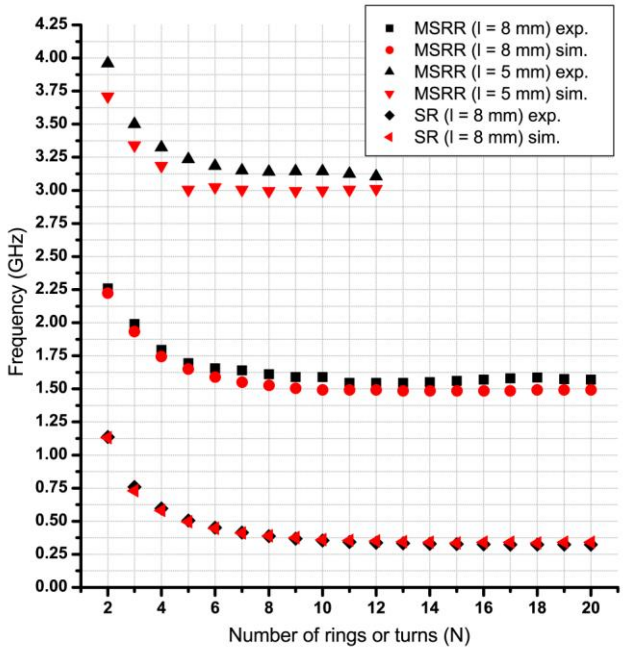

Figure 2.6. Resonance frequency as a function of the number of rings and turns (Experiment and simulation)

As N gets larger values the capacitance of the structures increases while the inductance decreases. Since the proportion decrease of the inductance is smaller than the proportion increase of the capacitance we observe a shift of the resonance frequency to lower values. The proportion capacitance difference between the MSRRs and SRs is due to the split capacitance of the MSRRs. The total split capacitance of the MSRRs is significantly smaller than the distributed one. Therefore, as we change the number of rings (turns), the proportion capacitance change of the MSRRs and SRs shows a similar behavior. The

miniaturization factor difference of the MSRRs and SRs is related to inductance [38]. For the MSRRs in addition to the average length of the strips, the filling ratio has an additional decreasing effect on the inductance. Therefore, the proportion decrease of the inductance is higher for the MSRRs that give a smaller miniaturization factor. The saturation of the resonance frequency is due to the saturation of both the inductance and the capacitance of the structures. The average length and the filling ratio increase with a decreasing rate, which yields a saturation behavior.

2.6. Substrate Effects and Size Scaling

We numerically studied the substrate effects on the design of electrically small negative permeability medium particles. As shown in Figures. 2.7(a) and 2.7(d), we selected the MSRR and SR resonators with l = 4 mm, and N = 10 for this analysis. The resonance frequency and electrical size of the particles were calculated for different substrates that are available in the standard printed circuit board and optical lithography processes. In these calculations we ignored the metallic and substrate losses, which do not have any significant effect on the resonance frequency, but do on the simulation time. In Figures 2.7(b) and 2.7(c) we plotted the resonance frequency in reduced units, i.e. we scaled the frequency to the case in which Rogers RT/Duroid 5880 substrate was used. We see that even though the substrate permittivity is a universal scale factor to first order, the MSRR and SR cases do not overlap exactly in Figure 2.7. The root of this difference is in the effect of the split capacitance of the MSRR. These capacitances, in fact, sum up with the distributed capacitance between two adjacent rings and do not have a counterpart in the SR case. In Figures 2.7(e) and 2.7(f) we showed that increasing the substrate permittivity approx. 6 times reduced the electrical size by approx. 2 times. Therefore, the miniaturization factor can be improved by using higher permittivity substrates. In our experiments, the substrate was RT/duroid 5880 with ε_r = 2.0 and we expect

higher miniaturization factors for different substrates, which are shown in Figure 2.7.

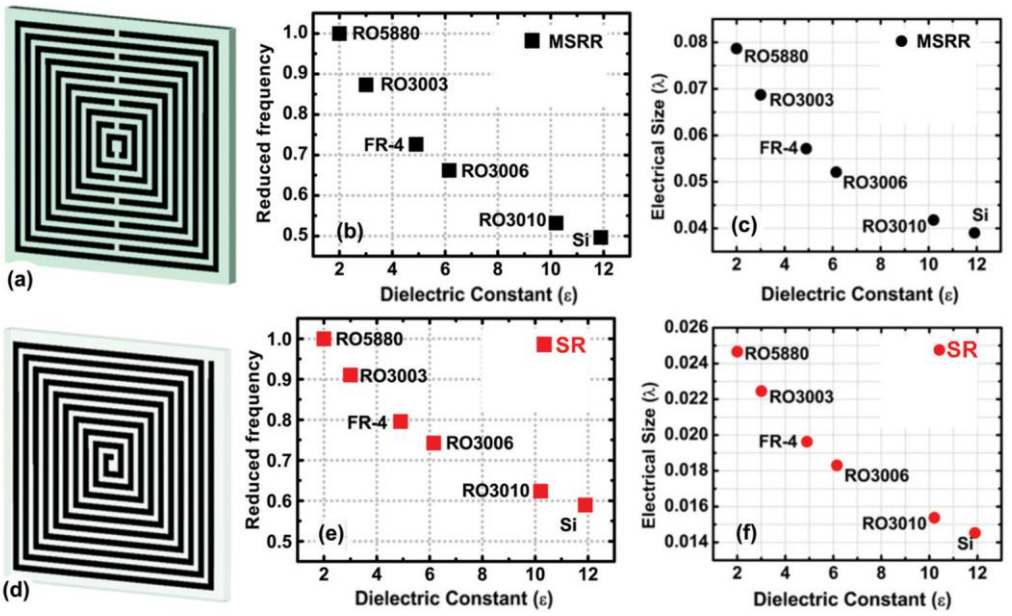

Figure 2.7. (a) Geometry of the multi-split ring resonator (MSRR) particle, N = 10, l = 4 mm, s = w = g = 100 µm. (b), (e) Resonance frequency in reduced units (f_{red}). For the MSRR $f_{red} = f_0$ / (4.17), for SR $f_{red} = f_0$ / (1.307), where 4.17 and 1.307 are the resonance frequency for RT5880 substrate in GHz units, respectively. (d) Geometry of the spiral resonator (SR) particle, N = 10, l = 4 mm, s = w = 100 µm. (c), (f) Calculated electrical size as a function of the substrate permittivity. The permittivity of the substrates: RO5880: ε = 2.0, RO3003: ε = 3.0, FR-4: ε = 4.9, RO3006: ε = 6.15, RO3010: ε = 10.2, Si: ε = 11.9.

We finalize this section by searching the limits of the particles that can be produced via the current printed circuit board technology. In Table 2.2, we showed the measured resonance frequency of the MSRR and SR particles with N = 20, $l=20(s+w)$ and the separation between the strips (s) and width of the strips (w) were pushed simultaneously down to 50 µm. As the overall particle size reduced the resonance frequency shifted to higher frequencies. By the size scaling of composing individual particles many different combinations of media with controllable permeability can be designed.

s = w (μm)		1	1	7	5
f_0 (GHz)	*MSRR*	1.26	1.55	2.03	3.09
	SR	-	0.31	0.41	0.60

Table 2.2. Geometric parameters and resonance frequencies for the particles (MSRRs and SRs) with a number of rings (turns) N = 20 scaled to operate at higher frequencies. The side length (l), strip width (w), separation between the strips (s), and resonance frequency (f_0) are shown.

2.7. Tunability of Multi Split Resonators

One of the key advantages of the multi-split elements is that they can be tuned by shorting the split-rings independently. We investigated the resonance of a MSRR when one of the splits is closed at a time. Here we fabricated the resonators as shorted. Figure 2.8 displays the results of digital tunability. As we shorted the second outer most ring (Ring # 3) of the MSRR with N = 12, l = 8 mm, we saw that the resonance frequency shifts from 1.53 GHz to 2.17 GHz. Measurements for the other cases shown in Figure 2.8 were also performed. It is possible to short any arbitrary combination of splits, for the MSRR resonator there are 2^{11} combinations each of which will yield to a different resonance frequency. One of the most suitable techniques for tuning multi-split elements is to incorporate photo-switches at the split area of the rings. Photoconducting switches for microwave applications were discussed by Vardaxoglou et al. [40]. In the presented technique a semiconductor substrate is placed or deposited to cover the split area of the rings. When a light is focused on the split region the photoconductor shorts the corresponding ring and the resonator starts to operate at another frequency.

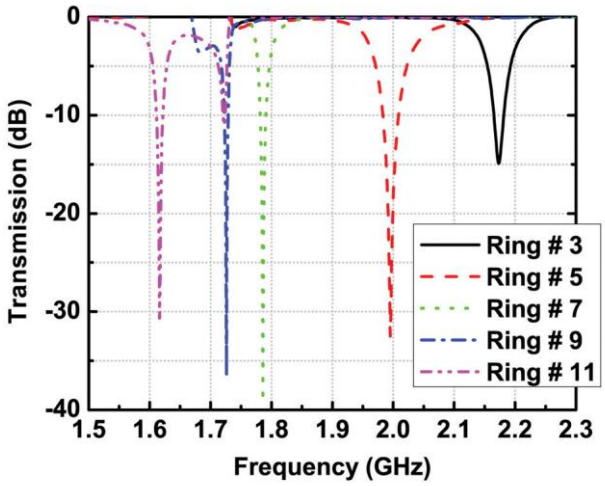

Figure 2.8. The shorted multi-split ring resonator (MSRR) response. Here the resonators were fabricated as shorted and photoconductive switches were not used.

2.8. Temperature Dependent Resonator Response

In order to obtain metamaterials operating at higher frequencies, the physical size of the metamaterial unit cells has to be smaller. In the process of unit cell size scaling it was observed that due to the losses at the metallic components, the magnetic resonance strength saturates [41]. In addition, the fabrication of circularly shaped metallic resonators becomes more complicated as the operation frequency increased [42, 43]. These obstacles led researchers to come up with novel designs called planar metamaterials [6, 42-45]. Cut-wire pairs, which provide magnetic resonance, had a smaller total capacitance compared to the same size split ring resonator. Therefore, cut-wire based metamaterials can operate at higher frequencies, which proposed a solution to the saturation and fabrication problems [45]. The design and fabrication solutions provided in this direction, especially to demonstrate negative index metamaterials at optical frequencies, has attracted much attention [41, 46]. One critique should be emphasized at this point: in order to be able to obtain an effective medium, the electrical size of the composing elements should be at least an order of magnitude smaller than the operation wavelength. The planar metamaterial

approach fails to provide this condition: the electrical size of the cut-wire pairs were close to λ/2 and not much smaller than the operation wavelength. In the present section, we would like to discuss another possible solution to the weakening response of metamaterial elements. It is well known that the properties of metallic features are strongly dependent on the environment temperature [47]; surprisingly, there has been no direct observation of the low temperature behavior of metamaterials that are composed of metallic elements. We propose to decrease the operation temperature of the metamaterial elements, which could be a candidate solution to the weak response of negative permeability media.

We noticed very recently that: while trying to obtain deep subwavelength magnetic metamaterial elements at microwave frequencies, due to the ohmic losses of the constituting metallic elements with thin features, their magnetic resonance saturates [32]. The saturation was directly related to the resistance and electrical size of the resonators. Thereby, we expected that the reduction of conductive losses would increase the resonance strength and thereby larger negative permeability values could be obtained. In order to understand the underlying physics, we selected a specific type of element, as shown in Figure 2.9, and investigated the theoretical formalism that is developed in the literature [2, 7]. The effective permeability of a medium composed of periodically arranged subwavelength resonators can be written as:

$$\mu_{eff} = 1 - \frac{F}{1 - \frac{\omega_0^{\,2}}{\omega^2} + i\frac{1}{Q}} \tag{2.1}$$

Here, F is the fractional volume constant, ω_0 is the resonance frequency, ω is the frequency of the incident electromagnetic wave, and Q is the resonator quality factor. The Q-factor related to the metal losses of the spiral resonators (SR) as: $Q_c = \omega_0 L / R_c$. The Q-factor related to the dielectric losses (Q_d) [48] was found to be negligible and we used $Q = Q_c$. Whereas L is resonator

inductance, R_c is the resistance associated with the metallic losses: $R_c = L/\sigma_c v h \mu_0$. Here, σ_c is the conductivity, h is the deposited metal thickness and $\sigma_c = ne^2\tau/m$. The free electron density is represented by n, e is the magnitude of the electronic charge, τ is the mean free time, and m is the electronic mass [47]. The temperature dependent quantity is the mean free time τ. For copper, τ = 0.27 fs at 0°C and τ = 2.1 fs at the liquid nitrogen temperature [48]. At lower temperatures the mean free path, conductivity, and Q-factor increase in turn leading to larger negative effective permeability values.

In Figure 2.9, the electrically small element that was used as the unit cell of a μ-negative medium is shown. Metallic features are obtained by etching the deposited copper with a thickness of h = 9 μm coated on the RT/duroid substrate with a thickness of t = 254 μm. The listed relative permittivity and dissipation factor at 10 GHz are ε = 2.0 and tanδ = 0.0009. However, we used a slightly different relative permittivity which was ε = 1.54. The parameters of the SR elements are as follows: width of the strips, v = 100 μm; separation between the strips, s = 100 μm; side length, l = 8.0 mm; and number of turns, N = 3.

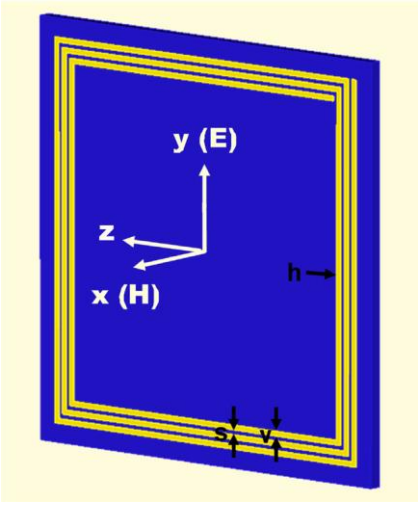

Figure 2.9. The spiral resonator (SR) geometry: side length, l = 8.0 mm, width of the strips, v = 100 μm, separation between the strips, s = 100 μm, and number of turns, N = 3, thickness of the substrate, t = 254 μm and deposited copper thickness, h = 9 μm.

The effective permittivity of the medium of densely packed resonators was found to be [7]:

$$\varepsilon_{eff} = \varepsilon_0 \varepsilon (1 + \frac{p_y l}{p_x p_z} \frac{K(\sqrt{1-k^2})}{K(\sqrt{k})}) \tag{2.2}$$

Here, K denotes the complete elliptic integral of the first kind while $k = s/(s+2v)$. The period in the x- y- and z- directions are denoted by p_x, p_y and p_z respectively. We assumed a closely packed medium with p_x = 4.1 mm, p_y = p_z = 8.2 mm. This formula is the low frequency permittivity of the medium due to the inter-cell coupling of the resonators.

We observed that as we attempt to decrease the electrical size of the spiral resonators by introducing more turns, the resonant strength obtained from the transmission measurements reduced and saturated. When we changed the resonator geometry by introducing splits on the rolled long metal thin strips, we obtained higher resonance strengths. These studies led us to investigate the effect of another parameter, temperature, which would increase the resonance strength while keeping the element geometry and electrical size the same.

The temperature dependent resistivity of copper was given by the Mathissen rule as [48] $\rho_{tot} = \rho_{res} + \rho(T)$. Here ρ_{res} denotes the residual resistivity that is independent of temperature and $\rho(T)$ is the resistivity for ideal lattice of the material: $\rho(T) = \rho(0) r(T)/r(0)$. Here r is the reduced resistance: $r(T) = 1.056(T/\theta)F(T/\theta)$, T/θ is the reduced temperature and θ is the Debye temperature and θ = 347 K for copper. The values of $F(T/\theta)$ between the temperature range of interest were taken from resistivity tables given in Ref [49]. By using the tabulated experimental data [48], we calculated ρ_{res} = 0.0151 μΩ.cm and $r(0)$ = 0.7604. By using the specific formulas [38] we calculated the capacitance, the inductance and Q-factor of our resonator and derived the

effective permeability and effective permittivity values for the temperature range under interest. Note that instead of the formula given for the calculation of effective substrate permittivity: $\varepsilon_r^{sub} = 1 + (2/\pi)\arctan(t/2\pi(v+s))(\varepsilon - 1)$ [38] we used ε directly. In Figure 2.10, the enhancement of negative permeability for lower temperatures can be clearly seen.

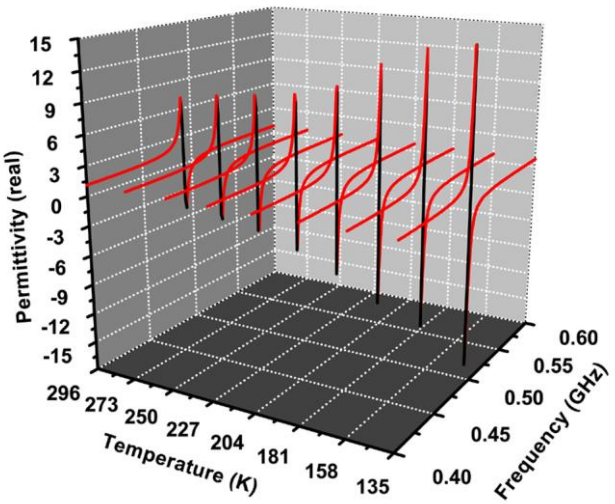

Figure 2.10. Theoretically calculated real part of the effective permeability of spiral resonator based closely packed metamaterial medium. Data is shown for the selected temperature values.

As we obtained the permeability and permittivity values, the transmission and reflection coefficients can be calculated by using the formalism developed for a homogeneous slab. After the calculation of S_{21} amplitude, we commented on the resonance strength. First, we found the effective index and impedance values by using $n_{eff} = \sqrt{\varepsilon_{eff}\mu_{eff}}$, $z_{eff} = \sqrt{\mu_{eff}/\varepsilon_{eff}}$. Then the transmission amplitude was found by:

$$S_{21} = \left[\cos(n_{eff}kd) - \frac{i}{2}\frac{z^2+1}{z}\sin(n_{eff}kd)\right]^{-1} \qquad (2.3)$$

Here, k is the wavevector, $k = \omega/c$, and d is the slab thickness at the propagation direction : $d = p_z$ in our case. In Figure 2.11, we show the

temperature dependent S_{21} data. As we decreased the temperature, the resonance strength increased in accordance with enhanced negative permeability.

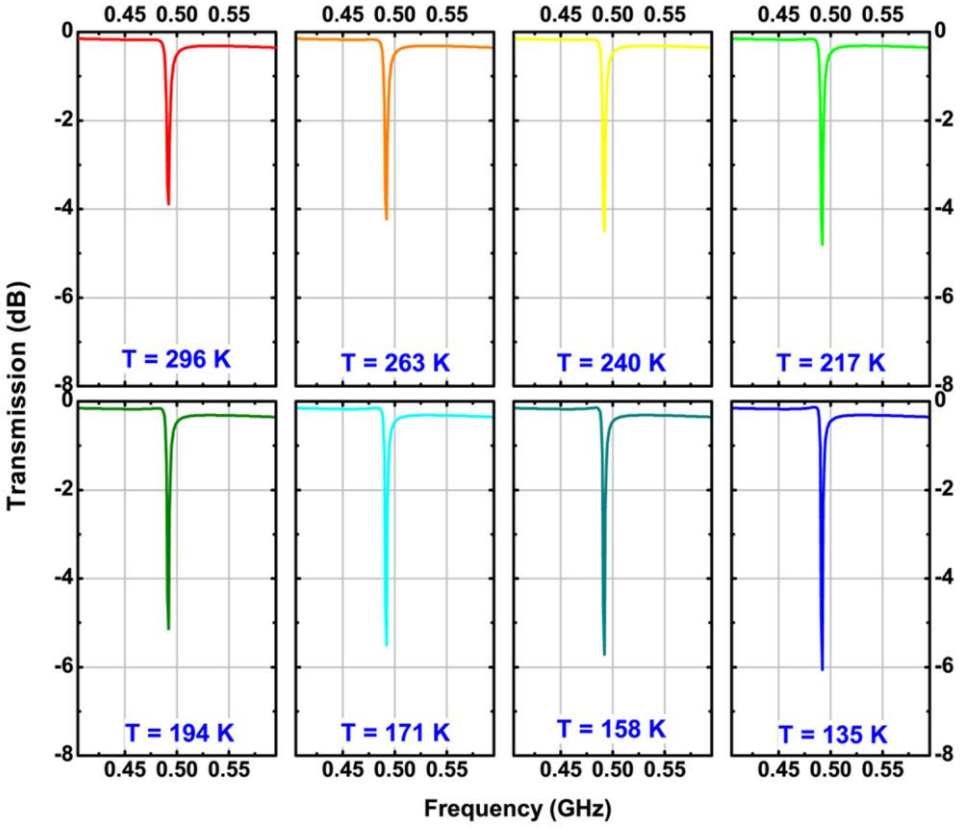

Figure 2.11. Theoretically calculated transmission amplitude data as a function of frequency. The results are plotted with 23 K temperature steps.

To verify these theoretical results, we constructed an experiment setup and investigated temperature dependence of resonance quality of the SR elements as shown in Figure 2.12. The setup consists of two commonly grounded microwave probe antennas, liquid nitrogen, a platinum resistance, and computer controlled instruments: Agilent N5230A Vector Network Analyzer and an Agilent AG34401 high performance digital multi-meter. The probe antennas operate at the reactive near field regime. During the transmission measurement, we placed a single element between the antennas wherein we obtained the

strongest response. The transmission spectra of free space i.e. before the element was inserted, was used as calibration data. Instead of through calibration, we used this method in order to clearly see the changes of the resonant response during the experiment. When everything is placed, we pour the liquid nitrogen into the can up to the antennas' level. The temperature of the sample was read from the multi-meter by the aid of a platinum sensor, which was placed at the same level as the sample. As the liquid nitrogen evaporates the temperature of the sample increases and eventually reaches room temperature. The computer aided automatic setup records the transmission response during the evaporation process. The temperature dependent free space calibration data was obtained similarly. We repeated the experiment for different samples and obtained their temperature dependent calibrated transmission responses.

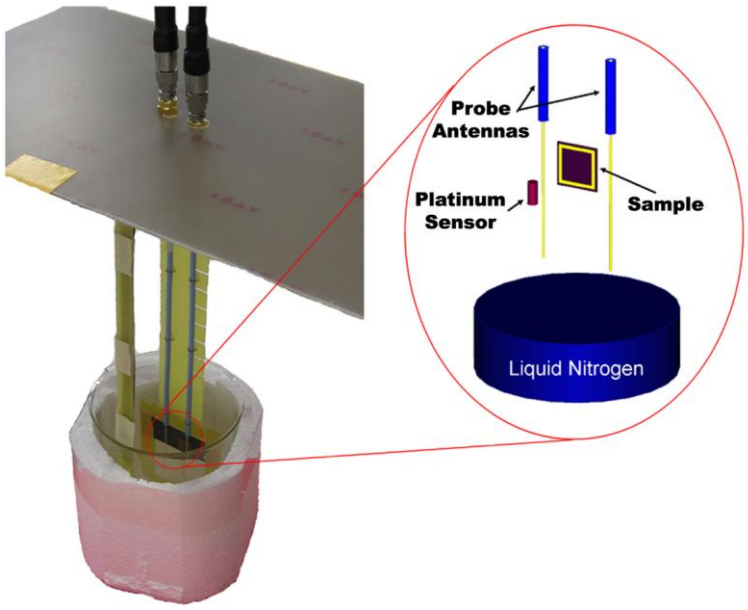

Figure 2.12. Experiment setup for temperature dependent resonator free space transmission response.

In Figure 2.13 we show the transmission response of the SR at different temperatures. Starting from the laboratory temperature, the transmission data was shown down to 135 K in steps of 23 K. In this setup, since we kept the antennas at a higher level than the liquid nitrogen as shown in Figure 2.12, the

lowest temperature value we obtained was around 125 K higher than the liquid nitrogen temperature 77 K. We saw that the decreasing temperature did not have any effect on the resonance frequency. On the other hand, due to the increased conductivity, the resonance strength significantly increased. We also tested SRs with N=4 and N=20. For the N=4 case the effect was minor and for the N=20 case we did not see any change. In order to be able to increase the resonance strength of the samples with a longer metal length, we had to reduce the temperature further, which was only possible with a cryogenic experimental setup. In Figure 2.13, we showed the results of the obtained dip and peak values at the resonance frequency as the temperature changed. For this particle, even its electrical size kept the same, the resonant strength doubled by decreasing its temperature 150 K. Doubling the resonance strength means larger negative permeability values, or in other words the negative permeability values for saturated elements at room temperature.

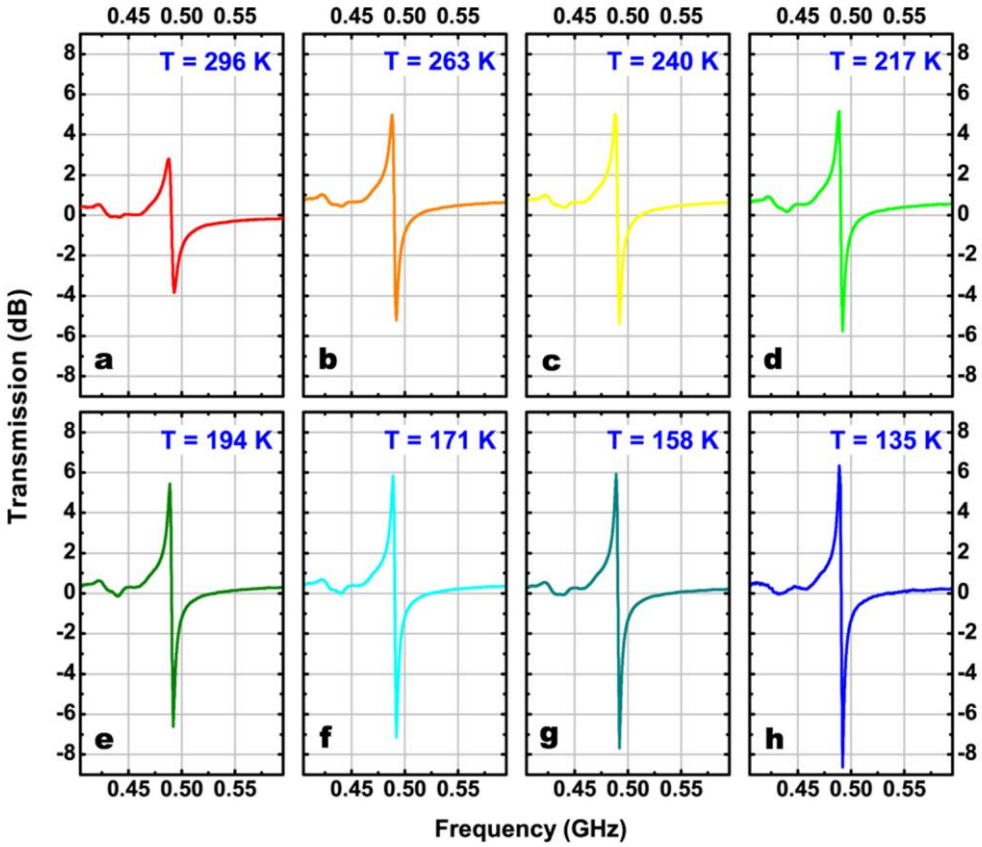

Figure. 2.13. Calibrated experimental transmission amplitude data as a function of frequency. The results are plotted with 23 K temperature steps.

In principle, we can obtain a negative permeability medium by using electrically small split-ring resonators under a low temperature environment at optical frequencies. The mechanism works by decreasing the losses and not by inhibiting the saturation of resonance frequency due to the kinetic energy of the electrons in the metal. By using subwavelength elements together with wire mesh at a low temperature, we can also obtain a negative index flat lens and convey the current metrology to a higher level.

Chapter 3

Millimeter-Wave Scale Metamaterials With Negative-Index of Refraction

3.1. Introduction

Most solid materials are in crystalline form, i.e. on the microscopic level the ions are arranged in a periodic array [48]. In the presence of an applied electromagnetic field, the materials' linear response is described by (electric) permittivity (ε) and (magnetic) permeability (μ) parameters. By introducing an artificial periodic array wherein repeated elements of the so-called metamaterial are arranged, we can obtain a medium with a controllable linear response at any desired narrow frequency band up to ultraviolet. The unit cells of metamaterials are commonly composed of metallic-dielectric structures of several shapes [1, 2, 50]. Recently, ferroelectric and ferromagnetic materials were also utilized as constituting elements leading to negative effective permeability media [51-54]. One can also obtain double negative medium by using all dielectric media at microwave and optical regimes [55-58].

A medium of periodically arranged, subwavelength, high permittivity ferroelectric rods was demonstrated to have effective negative permeability due to the induced large displacement currents that create magnetic resonance in the presence of the applied electromagnetic field at the GHz regime [51]. A temperature tunable μ-negative medium, which operates at the first Mie resonance mode of the constituting ferroelectric cubes, was observed between 13.65 - 19.65 GHz [52]. The properties of ferromagnetic materials have led to novel opportunities for μ-negative medium designs. In the vicinity of ferromagnetic resonance (FMR), the effective permeability of ferromagnetic

materials can be negative. This phenomenon was demonstrated experimentally by using YIG slabs at 10 GHz [53] and (La:Sr)MnO_3 layers at 90 GHz [54]. These are the few examples of metamaterials utilizing ferro-substances. A rather widespread technique of realizing metamaterials involves nonmagnetic metal-dielectric components.

Electrically small nonmagnetic metallic resonators are proposed as constituting elements of a μ-negative medium [2] and metallic wire mesh structures provide a low frequency plasma system with negative permittivity [50]. An experimental demonstration of a double negative ($\varepsilon < 0, \mu < 0$) medium (DNG) as a superposition of split ring resonators (SRR) and wire mesh medium was realized [1] and its unusual properties, such as negative index of refraction, negative phase velocity, reversal of Cherenkov radiation, and Doppler shift have attracted much attention. Applications of DNG and single negative (SNG) media involve the electromagnetic phenomena of reflection, absorption, radiation, cloaking, refraction, and subwavelength imaging. Planar reflectors that operate like an artificial magnetic conductor (AMC) with high surface impedance have been demonstrated at GHz frequencies [13, 14]. A miniaturized rectangular patch antenna with a μ-negative medium substrate operating at 250 MHz [7] as well as an electrically small circular patch antenna loaded with a μ-negative medium are characterized experimentally and theoretically [8]. A negative permeability medium element loaded monopole antenna was demonstrated experimentally at around 4 GHz in terms of its fundamental limitations [9] and multiple element effects [10]. A negative permittivity shell loaded monopole antenna was developed analytically [11]. In principle, one can enhance the transmission through a subwavelength aperture by utilizing a μ-negative medium cover [12]. This topic was demonstrated theoretically for the periodically arranged subwavelength holes by using deep subwavelength resonators [59] in addition to the previous photonic crystal and surface grating aided enhanced transmission studies [60-63]. By using a metamaterial cover it is possible to nearly cloak a subwavelength object at a particular frequency [20-22]. The negative refraction property of metamaterials

[1, 18] leads to a rather important application: the subwavelength imaging [64].

It is important to demonstrate a μ-negative medium at different regimes of the electromagnetic spectrum. At the MHz region, μ-negative medium elements lead to the improvement of magnetic resonance imaging by guiding the flux from the object to the receiver [28]. Electrically small metallic elements on planar substrates that operate at the MHz and GHz region and their potential applications have been extensively studied theoretically and experimentally [24, 32, 65]. E-beam lithography techniques allow us to obtain single ring SRRs of a 110 nm side length [66]. By scaling the physical size of the SRRs, a magnetic response at around 5 THz [5], 6 THz [67], 100 THz [46], and 370 THz [43] were demonstrated experimentally. On the other hand, it has been extensively studied that on the process of size scaling due to the ohmic losses of metallic features, the magnetic resonance of SRRs saturate as the operation frequency increases [41, 66, 68]. One way to overcome this problem was to introduce more splits [69, 70] or by using cut-wire pairs [71] and thereby reducing the total resonator capacitance. The resonant frequency increased via this method, but the physical size remained the same. Therefore, the electrical size of the element increased and became comparable to the operation wavelength. The realization of an effective medium becomes a problematic issue as we increase the electrical size of the constituting elements. Another method might be to decrease the environment temperature to enhance the negative permeability [72]. In the present work, we analyzed a split ring resonator based metamaterial medium operating at the millimeter wave regime.

3.2. Design and Experiment

Our design was realized by utilizing the well developed printed circuit board (PCB) technology. In Figure 3.1 we show the schematic view of the manufactured metamaterial layers. On the front face, we have the split ring resonators with parameters: width of the strips, w = 55 μm, separation between

the adjacent strips, s = 55 µm, split width, g = 55 µm, inner circle diameter, r = 110 µm. The period in the z- and y-direction are $a_z = a_y = 550$ µm. In terms of free space wavelength the period at the propagation direction (a_z) and one of the lateral directions (a_y) was approximately equal to $\lambda_0/6$ at around the resonance frequency. The substrate was Rogers RT/duroid 5880 with relative permittivity, $\varepsilon_r = 2.0$ and loss tangent, $\tan\delta = 0.0009$. The thickness of the substrate was 250 µm and the deposited copper thickness was 9 µm. On the back face of the PCB, we had continuous wires strips at a v = 275 µm width. The copper pattern tolerance values (55 µm) were nearly at the edge of the current PCB technology. For the slab characterization simulations we used a linearly polarized plane wave propagating at the –z- direction is incident upon the metamaterial layers, the E-field is at the y- direction and the H- field is at the x- direction. In these simulations we used the CST Microwave Studio [37]. The unit cell of the metamaterial medium under test is inserted into the simulation domain with periodic boundary conditions at the lateral directions (y- and x- directions). We simulated the reflected and transmitted time signals obtained the relevant complex S-parameters.

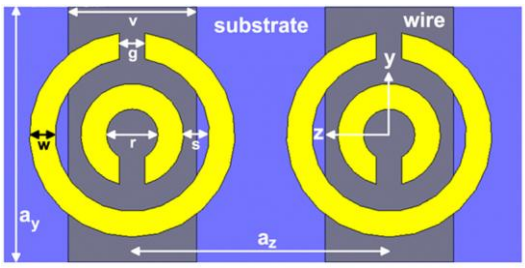

Figure 3.1. The parameters of the composite metamaterial medium (CMM).

The experiments were performed by using a millimeter-wave network analyzer with a 50 dB dynamic range from 75 GHz to 115 GHz. The transmission data in air was obtained by the aid of two standard gain horn antennae. The orientation of and distance between the antennae were kept fixed during the experiments. The media have 30 × 45 number of unit cells along the x- and y- directions, and the number of unit cells along the propagation direction

was varied as 3, 5, 7, and 9. The space between the metamaterial layers at the x-direction was 254 μm. We inserted the metamaterial slab between the horn antennae and measured its transmission response, and then removed the slab and noted the calibration data. By measuring the transmission response of the four different media, we characterized the composite metamaterial medium based on the qualitative effective medium theory [73, 74].

3.3. Transmission Based Qualitative Effective Medium Theory Analysis

In the effective medium theory analysis, we considered the transmission response of four different unit cell structures and concluded whether the composite metamaterial medium (CMM) was double negative. The SRR and closed ring resonator (CRR) geometry and corresponding induced surface current at the resonance frequency are all shown in Figure 3.2(a) and 3.2(b). Mostly due to the distributed capacitance between the two rings of the SRR, we observed induced circulating currents and a magnetic dipole-like response. By shorting the gaps of the SRR, we introduced the CRR structure on which the circulating currents disappear and at the operation frequency CRR acts like an electric dipole. In Figure 3.3, we showed the transmission spectra of the SRR and CRR media. There were 3 unit cells at the propagation direction. The media were transparent up to 75 GHz (not shown) and a stop-band for the SRR-only medium was observed. This gap was not present at the CRR transmission data, indicating its magnetic origin. Next, we considered the ε-negative wire-mesh medium. Its plasma frequency was designed to be at around 200 GHz. Even the wire-only medium might have negative-ε below the plasma frequency, the composite metamaterial acts as a different plasmonic system. The SRRs of the composite metamaterial kick in the effective permittivity and cause a downward shift of the wire-only medium plasma frequency. Therefore, instead of just considering the wire-only medium transmission response, we should also take

into account the transmission response of the CRR and wire composite (CCMM). We designed the medium parameters in such a way that the plasma frequency of the CCMM was around 150 GHz. We can guarantee thereby that the CMM medium is ε-negative below 150 GHz. Finally, we concluded that the transmission peak at around 100 GHz, as shown in Figure 3.3, was due to the double negative nature of the CMM medium. Our simulation and experimental results are in good agreement and we would like to emphasize that the experiment data is the average of many reproducible measurements. As expected, the transmission peak value ~ -2.5 dB was lower than the ideal simulation result. On the other hand, by using a low loss substrate and rather thick metal coating, we improved the ~ -25 dB transmission peak value of our group's previous 100 GHz metamaterial demonstration [4]. Moreover, instead of photolithography techniques, we achieved the desired double negative properties at the millimeter-wave regime by using a rather cheap technology. At the production step we stacked 30 planar layers of the medium under test in order to cover the entire incident beam. For the SRR-based metamaterial medium, the transmission response was not very sensitive to the angle between the antenna emission direction and metamaterial slab normal [75], or to the small misalignment of the layers [76]. This was not the case for the planar metamaterial media such as the fishnet structure [3].

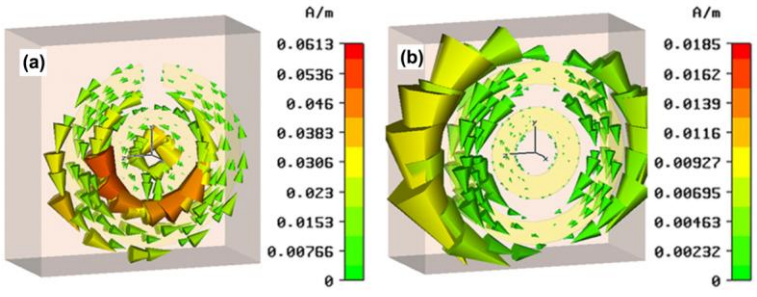

Figure 3.2. The schematic view and surface current (a) SRR. (b) shorted SRR, i.e. closed ring resonator (CRR).

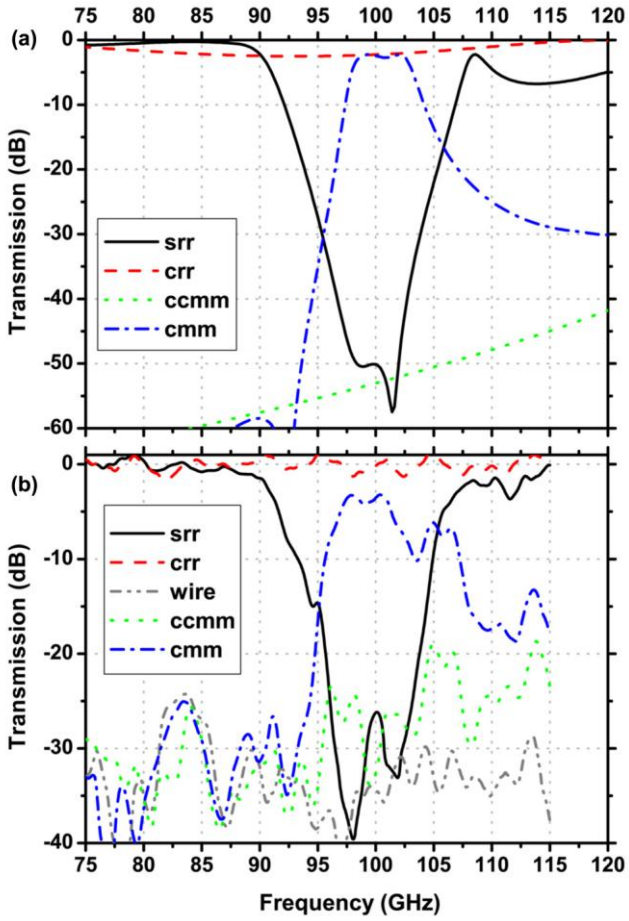

Figure 3.3. Transmission spectrum for 3 layered metamaterials in the propagation direction. Response of the SRR, CRR, CMM and shorted CMM i.e. closed composite metamaterial (CCMM) are shown. (a) simulation (b) experiment.

3.4. Retrieval Analysis

Another well-developed characterization method of metamaterials is the standard retrieval procedure [77-79]. The assigned effective refractive index (n) and relative impedance (z) values of the metamaterial slab can be extracted by using the complex scattering parameters with respect to 50 Ω. If the metamaterial slab under test is symmetric with respect to the x-y plane, i.e. $S_{11} = S_{22}$ and $S_{21} = S_{12}$, we can extract the effective medium parameters (n, z) of the metamaterial by using the terminology that was developed for the homogenous

slab. By using $\varepsilon = n\,z$, and $\mu = n / z$ formula, we derive the effective permittivity and permeability of the media. The complex scattering parameters for the case of our metamaterial were obtained from the simulations and by using the formalism of Refs. [77-79]. We extracted the n, z; ε, μ parameters of the CMM medium and showed as Figure 3.4. It is clear that at around 100 GHz the CMM medium is double negative.

At this point we would like to emphasize that just by itself the pass-band region shown in the qualitative effective medium theory can't be claimed to be double negative. Either the complete transmission analysis of the four structures should be studied or the pass-band region should be supported by the retrieval analysis. Here, we demonstrated the correlation between the two independent well developed effective medium theory analyses: the retrieval and transmission based effective medium theory.

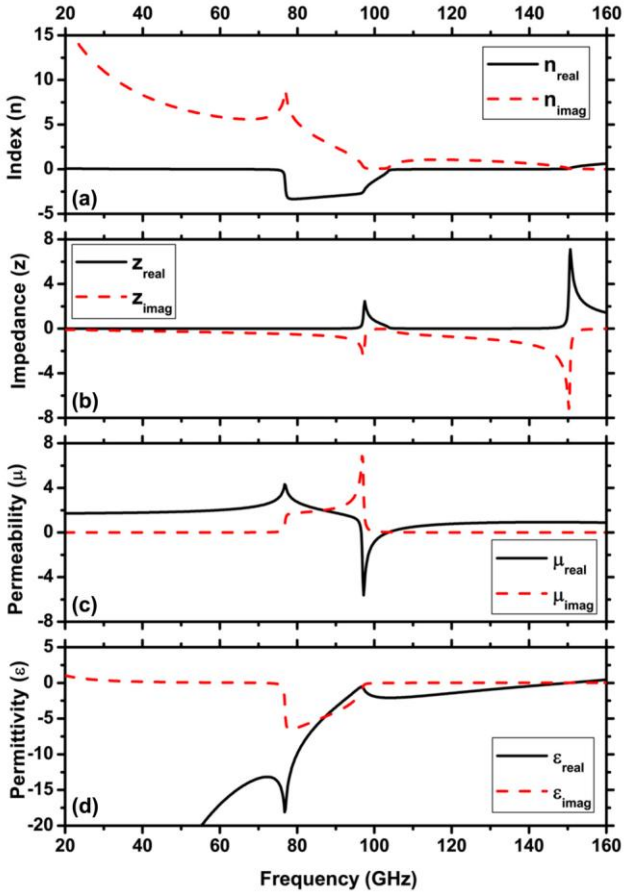

Figure 3.4. Extracted parameters as a function of frequency for the SRR-based metamaterial medium. (a) Refractive index (b) Impedance (c) Permeability (d) Permittivity

3.5. Loss and Bandwidth Analysis

The resonant nature leads the narrow bandwidth of metamaterials. We calculate the fractional bandwidth of the negative region via FBW = $\Delta f / f_0$, where Δf is the half power bandwidth and f_0 is the center frequency. We obtained for the 3 layer case $\Delta f = 4.8$ GHz, $f_0 = 99.9$ GHz and FBW = 4.8 %.

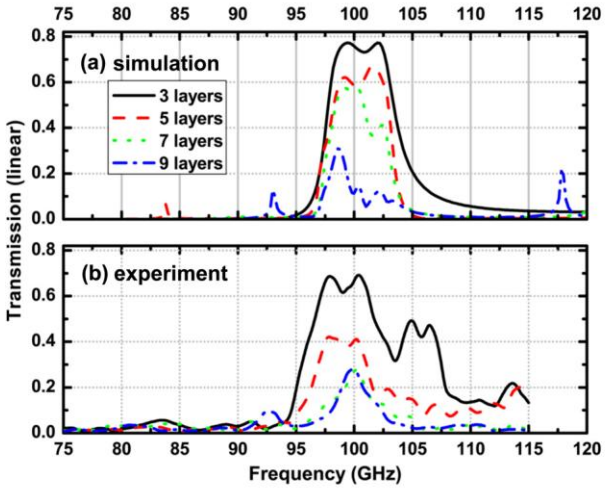

Figure 3.5. Transmission spectra in the linear scale for a several number of CMM layers in the propagation direction. (a) Simulations (b) Experiments.

In Figure 3.5 we show the effect of increasing the number of layers at the propagation direction to the transmission response. As expected the total loss (dB/mm) increases as the number of layers increase. We summarized the resulting loss and bandwidth data at 100 GHz in Table 3.1. We can clearly state that as we increase the number of metamaterial layers at the propagation direction, the total loss increases and the FBW decreases.

Number of Layers	3	5	7	9
Loss (dB / mm)	2.1	2.8	2.9	2.2
FBW(%)	7.5	5	3.9	3.3

Table 3.1. Calculated loss and FBW parameters for the increased number of metamaterial layers in the propagation direction.

3.6. Direct Observation of Negative Refraction

The schematic of the refraction spectra measurement setup is shown in Figure 3.6(a). The setup consists of a millimeter-wave network analyzer, automated

linear translation system, and two horn antennas as the transmitter and receiver. There were five metamaterial layers at the propagation direction. The transmitter horn antenna was on the right-hand side of the metamaterial with respect to its central axis. We scanned the spatial intensity distribution along the second metamaterial-air interface from 75 to 115 GHz. In Figure 3.6(b) we made an additional analysis related to anisotropy, in order to clarify that this anisotropic metamaterial has a negative index that indeed leads to the negative beam shift. In this analysis, we used the retrieval formalism developed in Ref. [79], which takes into account the asymmetry of the medium at the propagation direction. Even though the method of Ref. [79] was developed by considering a homogeneous media, it can be used to retrieve the effective medium parameters of anisotropic multi-dimensional metamaterials [79]. From the complex scattering parameters we extracted the metamaterial's refractive index and as shown in Figure. 3.6(b), we demonstrated that for oblique incidence with angle used in the experiment (22°) the metamaterial have a negative index of refraction at around 100 GHz. The refractive index, n was -1.0 at 99 GHz. Recently an experimental proof on the insensitivity of SRR-based metamaterials to the angle of incidence was provided. They are in parallel with the analyses' results given here [80].

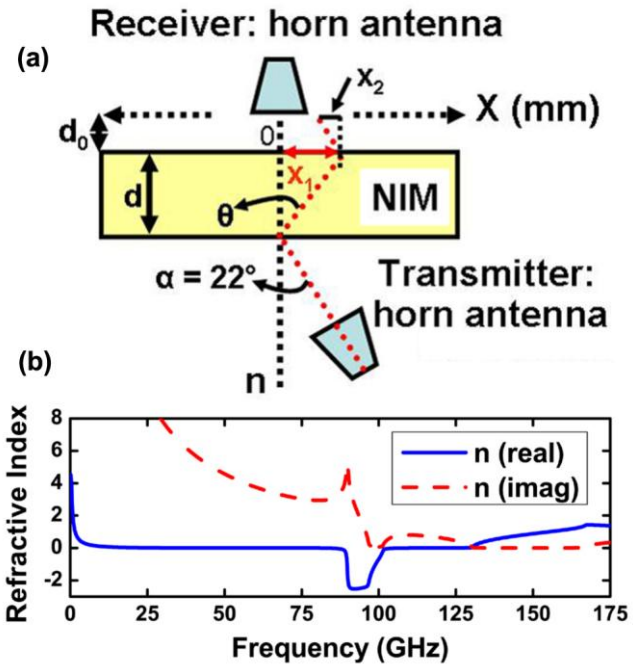

Figure 3.6. (a) Beam shifting experiment geometry, (b) Retrieved effective refractive index for the oblique incidence for α = 22°.

Figure 3.7 shows the transmission spectra as a function of frequency, in which the lateral position for the angle of incidence was α = 22°. For control purposes, we also measured the free space response. It is evident that for the metamaterial case, the transmitted beam appeared on the right-hand side. Thereby, the index of refraction of the metamaterial medium was negative. The frequency cuts at 99 GHz are shown in Figure 3.8, in which the appearance of a negatively refracted beam can be seen more clearly. By using the Snell's Law of refraction, we determined the refractive index from the experiment. The parameters shown in Figure 3.6(a) are as follows: thickness of the slab was d = 2.75 mm, distance of the horn antenna to the interface was d_0 = 1 mm, measured shift distance was x = 0.6 mm, and the incidence angle was α = 22°. By using simple geometric equations and Snell's Law: $n_{air}\sin\alpha = n_{NIM}\sin(-\theta)$, $x_1 = d\tan\theta$, $x_2 = d_0\tan\alpha$, $x = x_1 - x_2$, we derived the other parameters: refraction angle, $\theta = 20°$, shift distances, $x_1 = 1.0\,\text{mm}$, $x_2 = 0.4\,\text{mm}$ and refractive index, n = -1.0. The results are in good agreement with the theoretical

calculations. By just looking at the beam-shift we can't claim that the medium has a negative index. Thereby, here we demonstrated that there is a correlation between the negative band region determined by the qualitative effective medium theory analysis, retrieval analysis and the beam shifting experiment. We do not expect such a frequency dependent response from an arbitrary anisotropic medium.

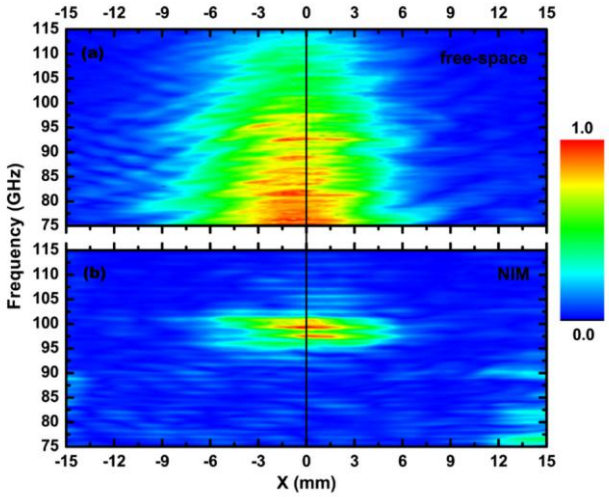

Figure 3.7. Transmission spectra as a function of frequency and scanning distance (a) Free-space (b) Negative-index metamaterial.

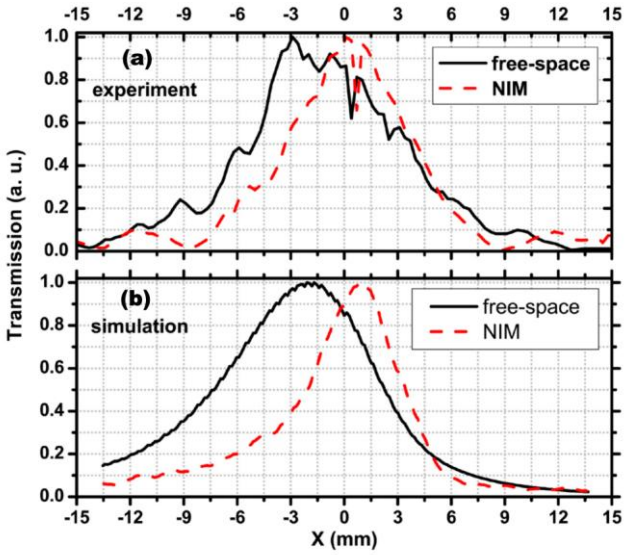

Figure 3.8. Frequency cuts at 99 GHz. (a) Experiment: free-space (solid curve), negative index metamaterial (NIM) (dashed curve) (b) Drude-Lorentz simulations.

We also confirmed the experimental results by using CST simulations. In these simulations, we modeled our negative index medium with the isotropic Drude-Lorentz model. The Drude model formula was: $\varepsilon(\omega) = \varepsilon_\infty + \omega_p{}^2 / \omega(\omega - i\upsilon_c)$ with the parameters: the plasma frequency, $\omega_p = 2\pi 130\,\text{GHz}$, the collision frequency, $\upsilon_c = 0.01$ Hz. For the magnetic dispersion Lorentz model formula was:

$$\mu(\omega) = \mu_\infty + (\mu_s - \mu_\infty)\omega_0{}^2 / (\omega_0{}^2 + i\omega\gamma - \omega^2) \qquad (3.1)$$

with the parameters permeability infinity, $\mu_\infty = 1$, permeability static, $\mu_s = 1.07$, resonance frequency, $\omega_0 = 2\pi 97.9$ GHz and the damping frequency, $\gamma = 1.3$ GHz were used. The Drude-Lorentz model parameters were selected in such a way that they were in good agreement with the retrieved effective parameters of the metamaterial medium at around 99 GHz. We made a Drude-Lorentz model fit to the retrieved effective medium parameters: permittivity (ε) and permeability (μ) and selected the model parameters by specifically paying attention to 99 GHz. We applied perfect electric conductor boundary conditions

at the vertical direction (y) and perfect absorbing boundary conditions in other directions. The transmitter horn antenna model that was used in the simulations has the same physical parameters as the one used in the experiments. It was fed with a waveguide port. By this method, the field propagation and far field profiles were simulated with efficient computation power. We demonstrated the field profile of the experiment in Figure 3.9 as an animation. The appearance of the beam on the right-hand side of the second interface, negative phase velocity inside the metamaterial medium, negative refraction and the reflection properties can all be seen in this animation. In Figure 3.9 instead of simulating the actual slab composed of many metamaterial unit cells, we used a homogeneous medium with assigned index and impedance. By this method, we could be able to observe the field profile in and around the negative index metamaterial slab. The main advantage of this method was the reduction of required computer power and memory.

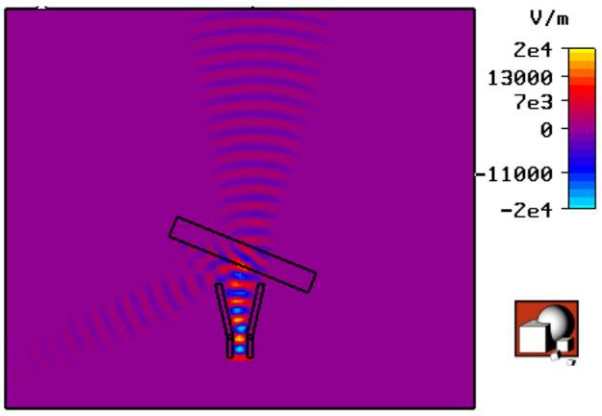

Figure 3.9. Electric field magnitude in **y**- direction at 99 GHz.

3.7. Study of a Metamaterial Prism

We synthesized a prism shaped metamaterial that was composed of stacked 7 layered blocks, in the lateral (**x**) direction. There were six different block types with unit cells in the propagation direction ranging from 3 to 9, as shown in

Figure 3.10. The angle between the prism's second interface and propagation vector was α = 8.4°. The setup consisted of a millimeter-wave network analyzer, an automated rotary scanner system, and two horn antennas as the transmitter and receiver. The transmitter horn antenna was parallel to the first meta-prism interface. We scanned the angular transmission intensity at a distance of R = 38 mm, which corresponded to the far field of the antennas from 75 to 115 GHz. Figure 3.11 shows the transmission spectra as a function of the frequency and scanning angle. As the frequency increases, the beam refracts from the negative to positive side. The transition can be seen from a negative index to positive index in Figure 3.11. We would like to point out the frequency band at which the beam was refracted to the negative side coincides with double-negative region predicted by the effective medium analyses. The unit cells of the metamaterial under study were adequately electrically small so that the periodicity related effects were minor.

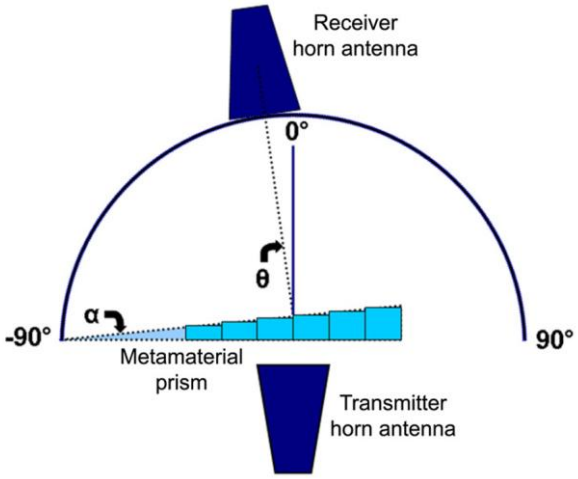

Figure 3.10. Schematic of the setup used in the millimeter-wave metamaterial prism experiment. The metamaterial sample, source and detector antennas, and air-prism second interface normal are shown. The prism angle α = 8.4° and scanning angle θ were changed from -60° to 60°.

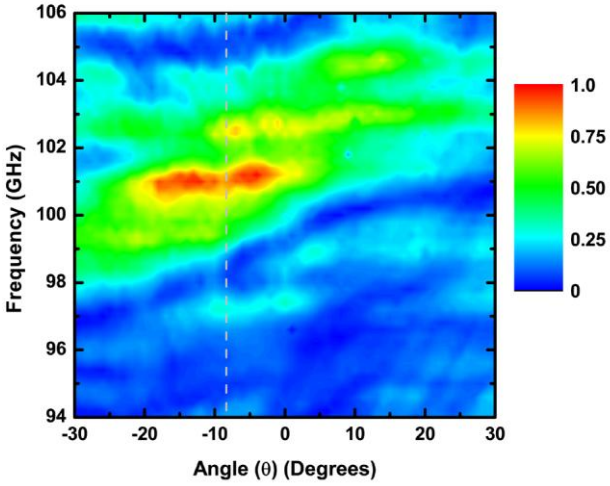

Figure 3.11. The transmission spectra as a function of the frequency and scanning angle θ.

In Figure 3.12, we showed the frequency cuts that were taken from the experimental data at 100 GHz. The normal of the second interface was demonstrated with a blue dashed line and arrow. We can compare the results of the free space and meta-prism cases in this figure. A negatively refracted beam emerges on the left-hand side of the prism normal, whereas the beam emerged on the right-hand side for the positive index medium. We also confirmed the experimental results by using CST simulations, in which the negative index prism was modeled with the Lorentz-Drude dispersion theory. The Drude-model parameters were as follows: the plasma frequency was equal to, $\omega_p = 2\ \pi\ 130$ GHz, the collision frequency was equal to, $\upsilon_c = 0.01$ Hz. For the magnetic dispersion, the following Lorentz-model parameters were used: permeability at infinity was equal to, $\mu_\infty = 1$, permeability static was $\mu_s = 1.07$, resonance frequency was $\omega_{res} = 2\ \pi\ 97.9$ GHz and the damping frequency was $\gamma = 1.3$ GHz. The retrieved parameters of the metamaterial medium were taken into account when determining the Drude-Lorentz model parameters. At around the frequency of interest, the retrieved ε and μ values were as close as possible to the Drude-Lorentz values. In this simulation, we applied the perfect electric conductor boundary conditions at the vertical direction (**y**) and in the other directions the perfect absorbing boundary conditions were applied. The physical

parameters of the transmitter horn antenna used in the simulations were the same as the experimental configuration except a waveguide port was placed instead of a coaxial probe feed. By this method, we obtained the field propagation and far field profiles with affordable computation power in a reasonable amount of time. Figure 3.13 shows the field profile. The negatively refracted beam emerging from the second prism interface, the negative phase velocity inside the metamaterial medium, as well as the reflection properties can be seen in this figure and corresponding animation.

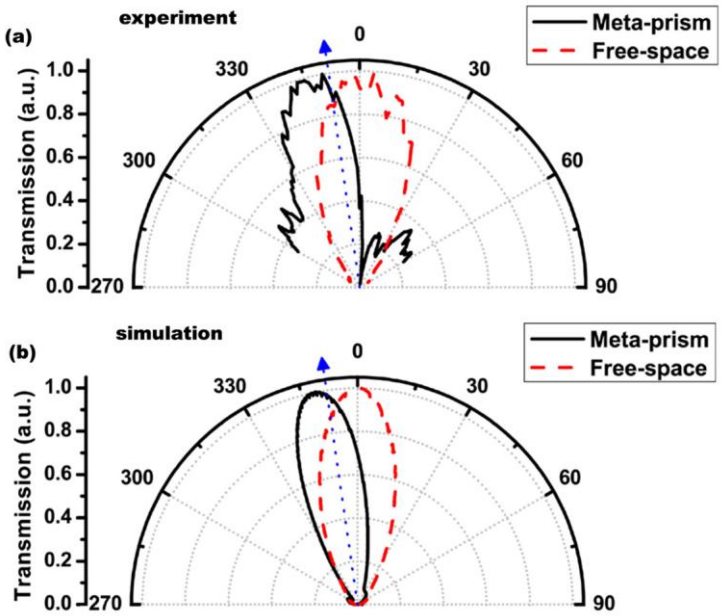

Figure 3.12. Frequency cuts of the transmission spectra at 100 GHz for the free-space and meta-prism (a) experiments (b) simulations.

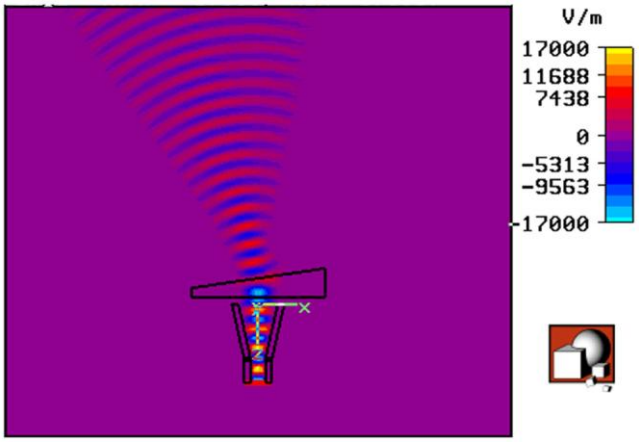

Figure 3.13. Two dimensional map of the electric field amplitude at the y-direction. Negative refraction and negative phase velocity can be seen.

3.8. Far Field Radiation Behavior of Horn Antenna and Metamaterial Composite

In this part, we investigated a novel composite antenna, which has two parts: i) horn antenna, ii) double negative metamaterial lens. Figure 3.14 displays measured and calculated far field pattern of the metamaterial lens/ horn antenna composite structure. We have modeled the homogeneous metamaterial by using Drude-Lorentz model in a way that at the frequency of interest the retrieved ε and μ values almost coincide. Other parameters in the simulations are kept the same as experiment. At the far field, R = 38 mm, by implementing an automated experiment setup we scanned the field intensity for both the horn antenna and for the hybrid structure. Being in good agreement the simulation, the experimental results showed that the metamaterial lens decreases the angular width of the hybrid structure's radiation pattern at the E-plane. Due to the experimental limitations we couldn't be able to scan the less interesting H-plane and couldn't comment on the directivity, gain and efficiency of the hybrid structure. We observed that the maximum transmitted peak value was 2-3 dB less than the horn-only case due to the lossy nature of the metamaterial lens. The behavior of the hybrid structure composed of a horn antenna as driven element

and DNG material as director can be considered as a novel phenomenon, which is similar to the behavior of Yagi-Uda antenna. The DNG part is passive and thin. It forms a rough image of the source. Its rough image and source itself can be used to explain the higher directivity of the composite system. In our millimeter-wave setup, we could only use horn antennas as the source and sink. Thereby we haven't tried to observe or optimize this effect with different sources. Moreover, the number of DNG materials at the propagation direction couldn't be increased due to our fabrication and measurement limitations. On the other hand, in Figure 3.14 (d) we showed the numerical result for the case of two DNG materials at the propagation direction. We showed that the directivity further increased in this case. The separation between the DNG materials was equal to their thicknesses and neither the thicknesses nor the separation between them was optimized. Here, we prefer to qualitatively demonstrate and explain the observed phenomenon.

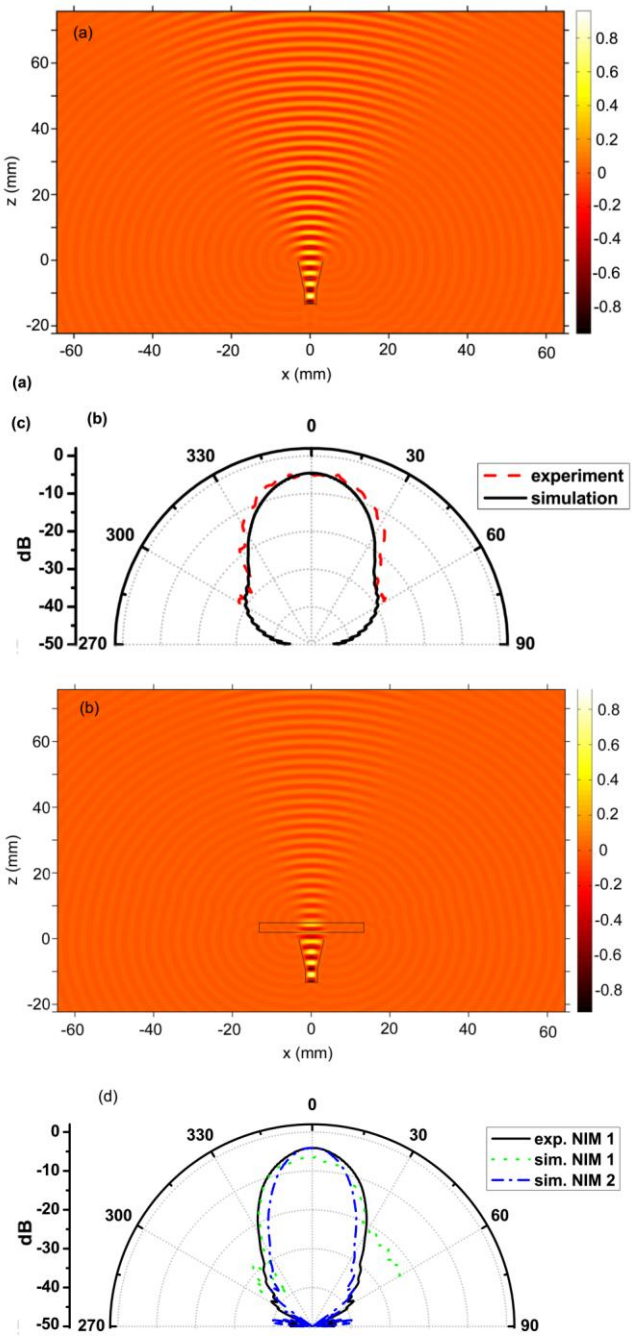

Figure 3.14. Simulated field map of (a) horn antenna, (c) horn antenna and metamaterial lens (hybrid structure) at 99 GHz. Focusing and redistribution of waves can be seen in part b. Far field patterns (b) horn antenna (d) hybrid structures with 1 and 2 NIM slabs at the propagation direction.

Chapter 4

Planar Metamaterials

4.1. Introduction

One of the major aims of the study of metamaterials is to achieve negative refraction at the visible range of the electromagnetic spectrum. By scaling the size of the SRR, a magnetic response at around 1 THz [81], 6 THz [67], 70 THz [82], 100 THz [46], and 200 THz [43] is achieved experimentally. However, metamaterials that are composed of layers of SRRs and wires have several restrictions. Firstly, as the size of the SRR is decreased, the magnetic resonance becomes weaker and approaches a limit [66]. A large number of SRR layers has to be produced and stacked in order to obtain the negative index medium. The fabrication of SRRs with resonance frequency at the visible range is rather difficult. Moreover, the alignment of the produced layers is a major problem. The restrictions of the conventional metamaterial construction are overcome by way of the introduction of planar metamaterials [43, 45, 66, 83].

Metamaterials for which the propagation direction is normal to the plane of the metamaterial layers are called planar metamaterials. A negative index metamaterial is experimentally demonstrated at 150 THz by using a pair of metal layers that are separated by a dielectric in order to provide resonant interactions along with a periodic array of holes [83] and at 200 THz by using a thin layer of pairs of parallel metal nanorods [84]. At this point, it is noteworthy that the imaginary part of the effective index of refraction for these works at the operation frequency was large, and thereby, the losses were significant. The systematic study and characterization of cut-wire pairs (cwp) operating at 300

THz [45] and the fishnet design at 200 THz [6] were performed experimentally. In the fishnet design, the cut-wire pairs are as wide as the lattice constant and are physically connected with the continuous wires, see Figure 4.1. Recently, a negative index metamaterial operating at 385 THz was experimentally demonstrated by using the fishnet design [42].

The experimental characterization and parametric study of planar metamaterials is rather easy for the operation frequencies at the GHz range. One advantage of working at this frequency regime is that the metamaterial features are sufficiently large to study several effects, such as the misalignment of metal pairs and metamaterial layers. Such studies are rather difficult to perform at the THz range. Recently, planar metamaterials at 14 GHz attained by using cut-wire pairs [85, 86], and at 13 GHz by using the fishnet design [87], were demonstrated experimentally. In the present work, we extend the experimental and numerical study of the fishnet structure to the case in which the structure is symmetric with respect to the x-y plane, which is shown in Figure 4.1. In this case, the x- and y-polarized incident wave the structure gives the same response.

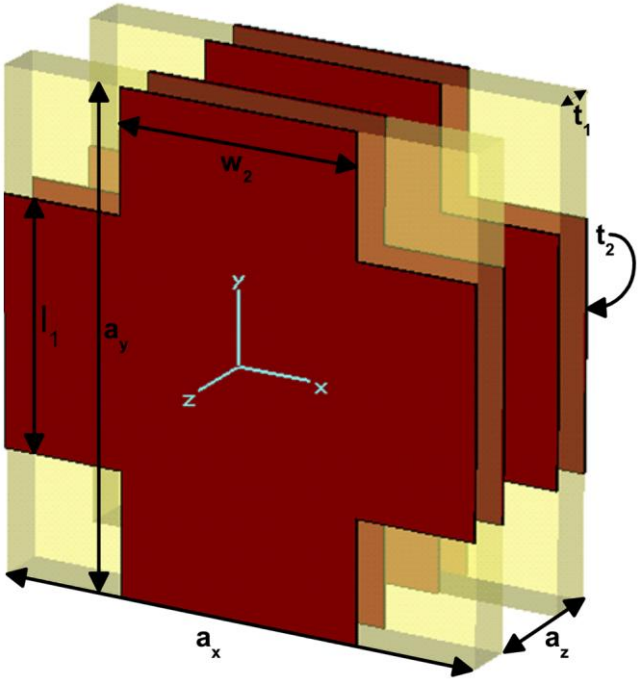

Figure 4.1. The geometry of one unit cell of the fishnet metamaterial. The electromagnetic wave propagates in the –z direction, in which E and B are along the y and z directions. There are two layers in the propagation direction; the parameters are given in the text.

4.2. Current Distribution, Transmission and Retrieval Analyses for 20 GHz

Theoretical modeling of the metamaterials is performed by using effective inductor-capacitor circuits (LC circuit). When the elements of the metamaterial in the propagation direction are small compared to the free space wavelength at the operation frequency, we can use the quasi-static process approach [30]. An LC circuit model for the fishnet structure was given in Ref. [87]. The model predicts the dependence of magnetic resonance frequency on the structure's parameters by way of the formula:

$$f_m = \sqrt{\frac{1}{l_1^{\,2}} + \frac{w_2}{l_1 l_2 a_x}} \tag{4.1}$$

where $l_2 = \frac{a_y - l_1}{2}$, l_1 is the cut-wire length, w_2 is the wire width, a_x and a_y are the periodicity in the x and y directions, see Figure 4.1.

There are two methods for the characterization of metamaterial slabs: the retrieval procedure and the effective medium analysis. The retrieval of the effective index of refraction (n), impedance (z), permittivity (ε), and permeability (μ) of a metamaterial slab is extracted from the magnitude and phase of the reflection and transmission data [77, 78]. On the other hand, the effective medium analysis is performed by only using the magnitude of the transmission data. However, four different structures are necessary: μ-negative (MNG) material, shorted MNG material, composite medium of MNG materials, and continuous wires (CMM), as well as the shorted CMM [74]. In the present chapter, we followed the latter characterization method, in which our MNG material is the cut-wire pairs, Figure 4.2(a), and the CMM is the fishnet structure, Figure 4.3(a).

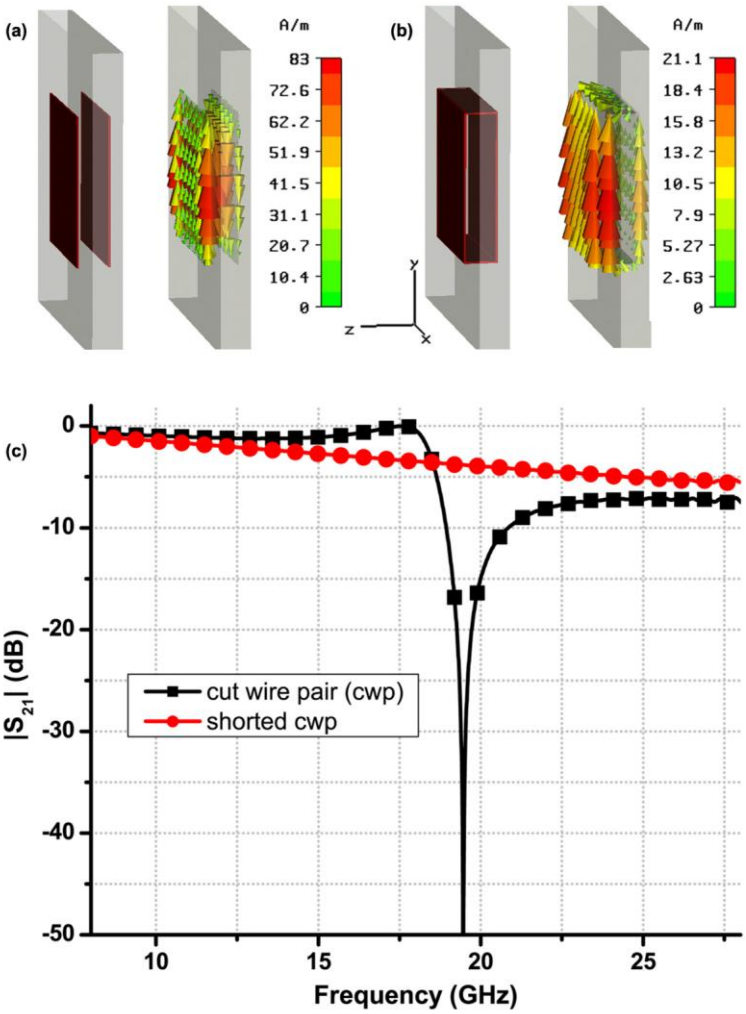

Figure 4.2. The geometry and surface current (a) the cut-wire pair (cwp). (b) shorted cut-wire pair (c) Transmission spectrum magnitude of the cwp and shorted cwp structures.

We perform a qualitative effective medium theory characterization numerically via the commercial software CST Microwave Studio. In the simulations, we insert the unit cell of the structure in a waveguide and obtain the scattering parameters by using waveguide ports. By way of this method, the structure unit cell is assumed to extend to infinity in the lateral directions and the incident, reflected and transmitted waves are in the form of a plane wave. The E field is in the y-direction, the B field is in the x-direction, and the propagation vector is in the negative z-direction: $\hat{E} = \hat{y}$, $\hat{H} = \hat{x}$, $\hat{k} = -\hat{z}$. The metallic

features are assumed to be a perfect electric conductor (PEC) and the relative permittivity of the substrate is ε_r = 1.94. Other structure parameters are as follows, see Figure 1: $a_x = a_y$ = 10 mm, a_z = 3 mm, $l_1 = w_2$ = 5 mm, t_1 = 1 mm, t_2 = 0.05 mm. We have one layer of the metamaterial in the propagation direction, in which the metal and substrate losses are ignored. The results of the first part of the effective medium analysis are summarized in Figure 4.2.

For the case of metamaterials a stop band at the transmission spectra indicates a resonance phenomenon, which could be electrically or magnetically originated. The fishnet metamaterial is composed of metallic and dielectric parts both of which are nonmagnetic. The only source of magnetic resonance is the circulating currents driven by the capacitance between the cut wires. A simple method to determine whether a stop band is due to the magnetic or electric resonance is to shorten the cut wire capacitance as shown in Figure 4.2(b). By this way the driven force of the circulating currents will be eliminated and the magnetically originated stop band at the transmission spectra will disappear, Figure 4.2(c) [74]. Moreover, as we kill the magnetic resonance by shorting the cut-wire pairs the circulating surface current in Figure 4.2(a) disappears and the current pattern becomes similar to an electric dipole, Figure 4.2(b). The second part of the effective medium theory analysis is summarized in Figure 4.3. The geometry of the CMM and shorted CMM are shown in Figure 4.3(a) and Figure 4.3(c), respectively. In this part, there are two layers in the propagation direction. The transmission data implies the existence of a negative index of refraction at around 21 GHz. However, the magnetic resonance frequency of the cut-wire pairs was around 19.5 GHz. This difference is a characteristic of the fishnet metamaterial and can be explained by considering the surface current at the first face of the metamaterial, Figure 4.3(b). When we combine the cut-wire pairs with the continuous wires, the effective cut-wire length decreases and the magnetic resonance frequency increases. Finally, we would like to note that the transmission properties remain the same when the incident wave polarization is

rotated 90°. Since the structure is symmetric with respect to the $x = \pm y$ plane this behavior was expected.

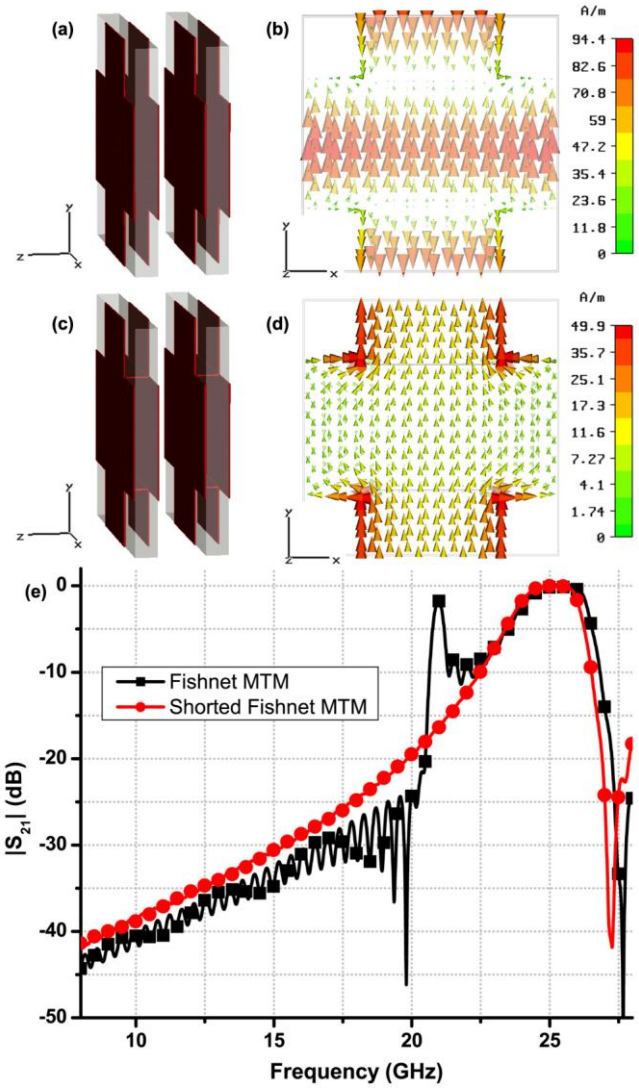

Figure 4.3. Schematic view (a) two layer CMM (c) two layer shorted CMM. Surface current on the face of the first layer (b) CMM (d) shorted CMM. (e) Magnitude of the transmission data for the CMM and shorted CMM structures.

The experiments were performed via an HP8510C Network Analyzer and two standard gain horn antennae. After the full two port calibration we first measured the scattering parameters for the free space i.e. without the metamaterial layers being inserted. Subsequently, we repeat the experiment wherein the metamaterial

slab is in between the antennae. The distance between the transmitter and receiver antennae is kept fixed at 79 mm during the experiments. The metamaterial substrate is cardboard of 1 mm thickness and the metallic features are formed by using an aluminum based tape. In Figure 4.4 the transmission magnitude and phase data are shown. The transmission data is scaled to the free space data. The experimental results are in good agreement with the simulation. At this point we should clarify the difference between the design simulations shown in Figure 4.3(e) and the more realistic simulation shown in Figure 4.4(a). In the design simulations, we assumed lossless metal and dielectric parts in order to clearly demonstrate the effective medium theory concepts (see Figure 4.2(c) and Figure 4.3(e)). In Figure 4.4(a), when comparing the simulation and experimental results we have taken the loss effects into account. The conductivity of the aluminum type and dielectric were 20000 S/m and 0.001 S/m respectively. The possible reasons of the discrepancies between the simulation and experiment are: the misalignment of the continuous and cut-wire pairs in a layer, small deviations of the fabricated material parameters from the intended values and misalignment of the multiple layers. We expect the transmission band between the frequencies 20.2 and 21.2 is negative (see Figure 4.3(e) and Figure 4.4(a)). The fractional bandwidth of the negative region is narrow and calculated as 2% by using the formula: FBW = $\Delta f/f_0$, where is Δf is the half power bandwidth and f_0 is the center frequency. The effective medium theory is a qualitative approach and in order to determine the negative band exactly a robust retrieval analysis is necessary [77, 78]. In Figure 4.4(b) we demonstrate that the phase shift of the wave within the left handed band is negative. In this band, as the number of layers increase, the phase decreases.

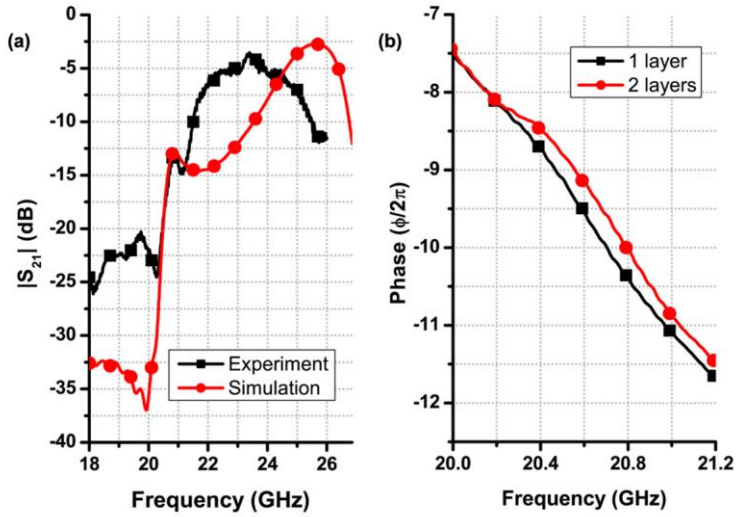

Figure 4.4. (a) The transmission spectrum of the fishnet metamaterial simulation and experiment. In the simulation, the loss of the metal and dielectric parts is taken into account. (b) Phase spectra of the metamaterial for a different number of layers.

4.3. 100 GHz Fishnet Metamaterial Design

The front view photograph of the fishnet metamaterial and unit cell are shown in Figure 4.5. There are 14 unit cells at the lateral directions, the incident E-field is in the y-direction, the B-field is in the x-direction and the propagation vector is in the –z-direction. The period in the x- and y-direction are $a_x = a_y = 2$ mm, cut-wire pair length is l = 1 mm and wire width is w = 1 mm. The relative permittivity of the substrate is $\varepsilon_r = 2.2 + i\ 0.0009$ and the substrate thickness is 254 μm. The coated copper thickness and conductivity are 9 μm and 5.8×10^7 S/m, respectively.

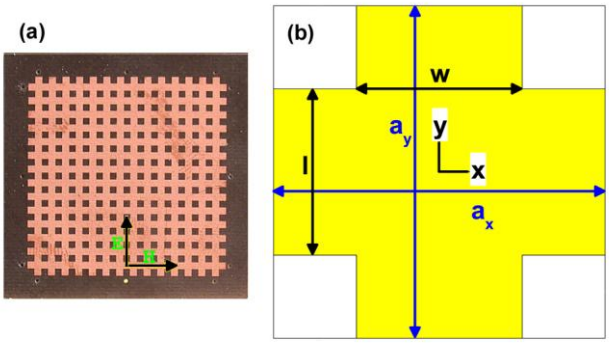

Figure 4.5. (a) A front view photograph of the fabricated fishnet metamaterial layer. The electromagnetic wave propagates in the –z direction, in which the E-field and B-field are along the y and z directions. (b) The geometry of one unit cell of the fishnet metamaterial.

4.4. Current Distribution, Transmission and Retrieval Analyses for 100 GHz

The results of the qualitative effective medium theory are shown in Figures 4.6 and 4.7. The electrically small cut-wire pair resonator geometry and induced surface current at the resonant frequency are shown in Figure 4.6(a). The circulating currents that are driven by the capacitance between the cut wires resemble a magnetic dipole response. When we short the capacitance, as shown Figure. 4.6(b), the circulating currents disappear and the response becomes similar to an electric dipole. The corresponding effect on the transmission spectra is the disappearance of the stop band, as shown in Figure 4.7(a). We can thereby infer merely by considering of the transmission spectra as to whether the stop band was magnetically originated. In Figures 4.6(c) and 4.6(d) we exhibit the fishnet metamaterial unit cell and its shorted version. The fishnet metamaterial is composed of cut-wire pairs that are connected to long continuous wires along the vertical (**y**) direction. The long continuous wires act as a low frequency plasmon system with a plasma frequency that is larger than the metamaterial operation frequency. The plasma response of the fishnet structure is expected to be very similar to the shorted version. Therefore, from

the transmission data show in Figure 4.7(b) we infer that the medium is ε-negative for f < 120 GHz and the transmission peak at ~100 GHz is the result of the double negative nature of the fishnet metamaterial.

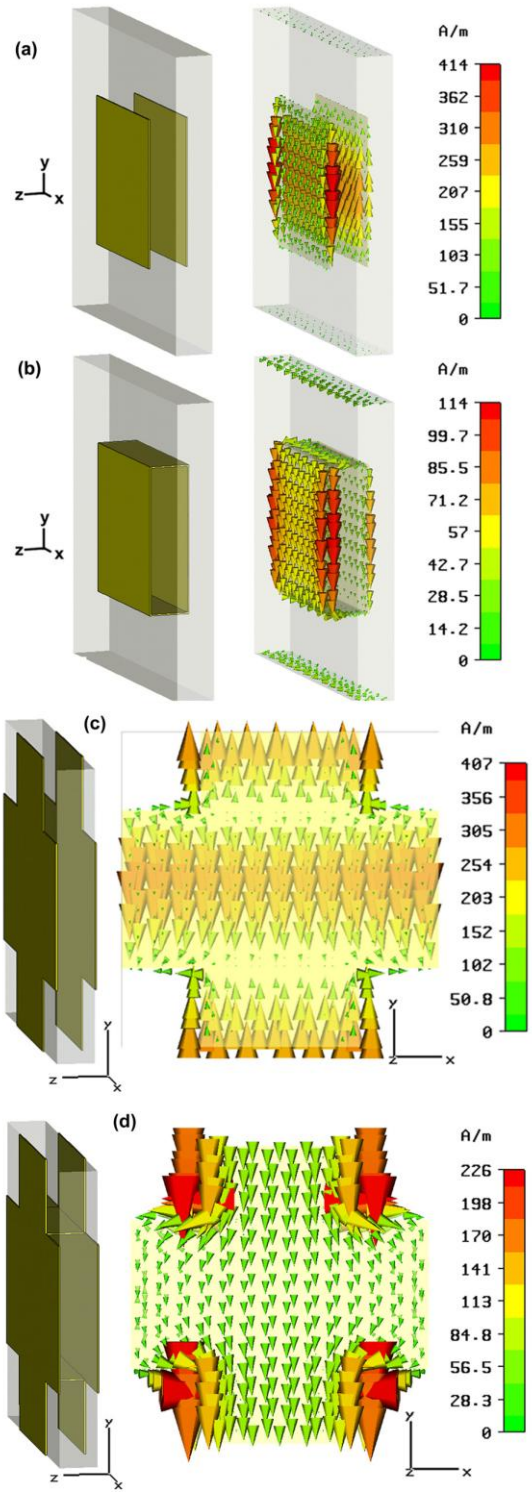

Figure 4.6. The schematic view and surface current (a) the cut-wire pair (cwp). (b) shorted cut-wire pair (sh-cwp) (c) fishnet (fn) (d) shorted-fishnet (sh-fn).

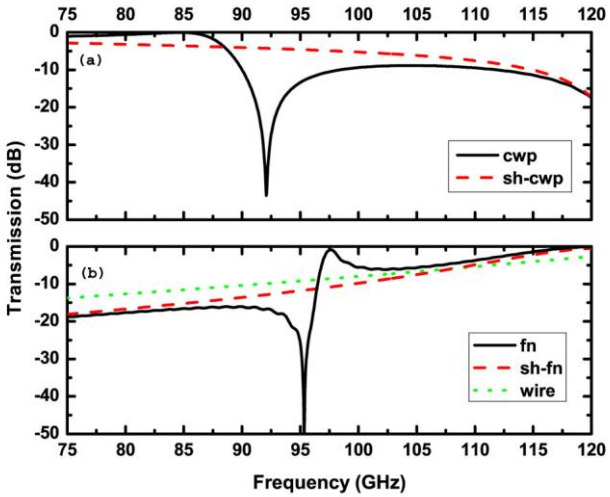

Figure 4.7. Transmission spectrum magnitude for one layer of structures at the propagation direction (a) the cut-wire pair (cwp) and its shorted version. (b) fishnet (fn), shorted fishnet (sh-fn) and the wire mesh medium.

We also present the standard retrieval analysis results. By using the complex scattering parameters we extract the index and impedance of the one layer fishnet metamaterial. The real part of the refractive index, permeability and permittivity are negative at around the transmission peak, Figure 4.8. The resonant nature leads to the narrow bandwidth of metamaterials. The fractional bandwidth of the negative region is calculated via FBW = $\Delta f / f_0$, where Δf is the half power bandwidth and f_0 is the center frequency. Here we obtain Δf = 1.57 GHz, f_0 = 97.7 GHz and FBW is 1.6%, which is a typical value for a fishnet medium [44]. We would like to emphasize that for any arbitrary polarization of the plane perpendicular incident wave the response of the metamaterial is the same because the unit cell of the fishnet metamaterial is symmetric with respect to the x-z and y-z planes.

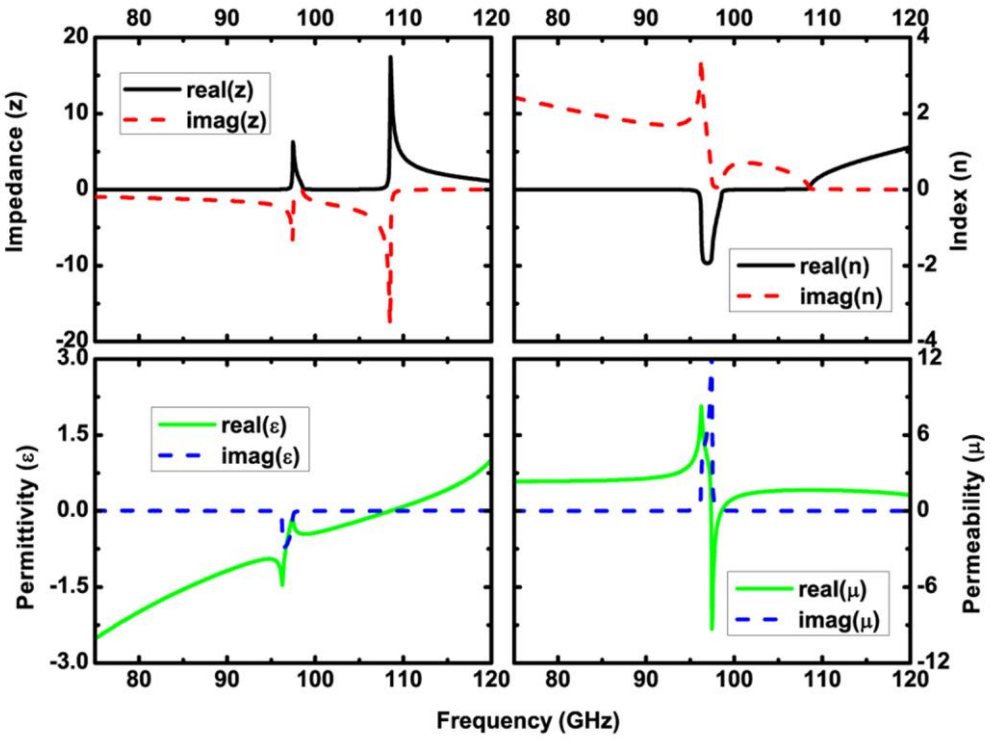

Figure 4.8. Extracted parameters as a function of frequency for the fishnet metamaterial medium.

For the experimental demonstration we use a millimeter-wave network analyzer that has a 50 dB dynamic range at the 75-115 GHz band. The experiments are performed in free space and room temperature by using two standard gain horn antennae. We kept the distance between (16 mm) and orientation of the antennae fixed and used the free space transmission data as calibration data. We stacked several layers at the propagation direction with a layer to layer separation of 250 μm. Spacers are placed at the very edges of the metamaterial layers so that the medium between the layers is air. In Figure 4.9 the experiment and corresponding simulation data are shown. We see a narrow transmission band at around 100 GHz. The experiment and simulation results are in good agreement in terms of the operation frequencies; however, the transmission magnitude in the experiment is rather low. At this point we would like to investigate the possible reasons for the discrepancies between the experiment and simulations in two groups: the fabrication based and alignment

based discrepancies. At the fabrication step, there may be small deviations of the material parameters from the intended values in terms of the size of the metallic features and misalignment of the features at the front and back faces of the substrate. However, our fabrication is a very well controlled process wherein the accuracy of the feature size is less than a micron. Therefore, we do not expect any significant fabrication based discrepancies. On the other hand, as the operation frequency increases the alignment of the several stacked layers and keeping the angle between the antenna emission normal and metamaterial plane normal as zero becomes rather difficult.

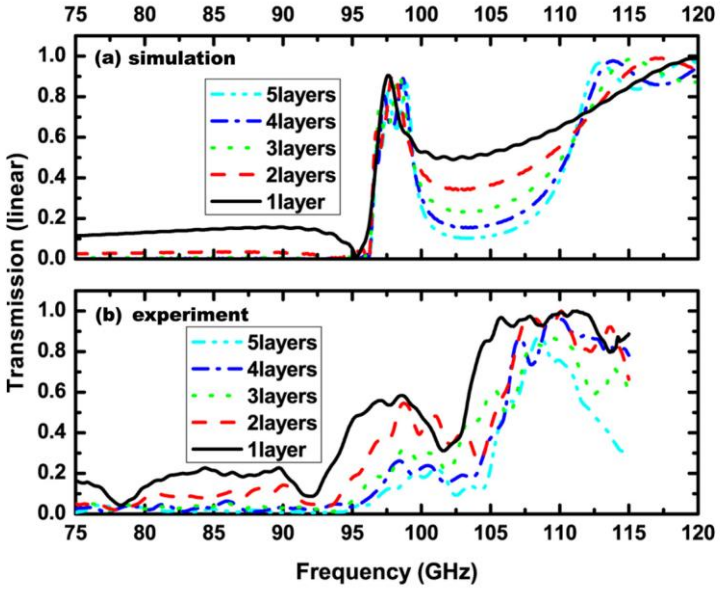

Figure 4.9. Transmission spectra in linear scale for several number of fishnet layers in the propagation direction. (a) simulations (b) experiments

Chapter 5

Oblique Response of Flat Metamaterial Slabs

5.1. Introduction

Metal dielectric based metamaterials are demonstrated to operate for normal incidence at several regimes of the electromagnetic spectrum. Some recent designs increased the operation frequency but at the expense of effective medium concepts. They used elements of electrical size that are comparable to the operation wavelength [42]. In order to be able apply the effective medium characterization methods to the designed metamaterials several points should be kept in mind. Firstly, the electrical size of the resonators are to be at least an order of smaller than the operation wavelength. Secondly, the number of metamaterial layers at the propagation direction should be large enough that the parameters permeability and permittivity are meaningful. Thirdly, the metamaterial should have an invariant response for oblique incidence especially for the exciting applications such as subwavelength imaging and the focusing of light.

In the present chapter, we first focused on the response of a split-ring resonator based composite metamaterials. The results are presented at the S-band for the case when the incident beam has a nonzero incidence angle. First, we introduced our design and structure parameters, and then showed the results of the qualitative effective medium theory characterization method. The frequency dependent response of a three-layered composite metamaterial, which

was illuminated with an oblique angle with respect to two bases, will be shown experimentally. Then, the results will be compared with a five-layered case.

5.2. Transmission Based Qualitative Effective Medium Theory of A SRR Based Metamaterial

The electrically small resonator part of the designed unit cell is shown in Figure 5.1. At the microwave frequencies, we prefer to utilize the printed circuit board technology for the fabrication of the metamaterial samples. By etching the metal coated substrates as desired, split ring resonator (SRR) shapes were obtained with following parameters: the strip width, w = 0.9 mm, the separation between the adjacent strips, s = 0.2 mm, the split width, g = 0.2 mm, outer ring radius, r_1 = 3.6 mm, inner ring radius, r_2 = 2.5 mm. The period of the resonators at the y and z directions was l = 8.8 mm. The substrate was FR-4 with relative permittivity, ε = 3.75, and the dissipation factor, tanδ = 0.002. The thickness of the substrate was 1.6 mm and the deposited copper thickness was 30 μm. On the back side of the substrate, centered continuous wires were fabricated with a width of w = 0.9 mm.

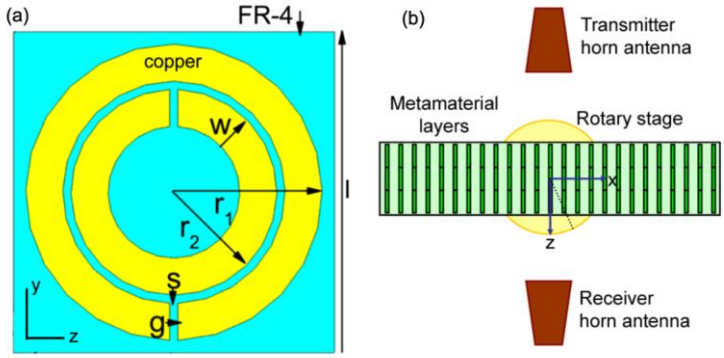

Figure 5.1. (a) The negative permeability medium unit cell: split ring resonator with parameters, w = 0.9 mm, s = 0.2 mm, g = 0.2 mm, r_1 = 3.6 mm, r_2 = 2.5 mm, l = 8.8 mm. The substrate was FR-4 with ε = 3.75 (1 + i 0.002), with the thickness 1.6 mm and deposited copper thickness 30 μm. (b) Schematic of the experiment setup when the metamaterial slab was rotated with respect to the **y** direction.

The qualitative medium theory analysis was performed numerically by using the CST-Microwave studio. The unit cell of the medium was illuminated by a normally incident plane wave and the transmitted signal was obtained via point field probes. The SRR medium transmission spectra had a stop-band at around the resonance frequency. When we measured the transmission response of its shorted version (sh-SRR) the stop-band disappeared, demonstrating the fact that the resonance was magnetically originated. For the sh-SRR, the split width is zero ($g = 0$) and thereby the capacitance of the SRR is shorted. We conclude this part of the QEMT by stating that at around the magnetic resonance frequency, the medium has negative effective permeability ($\mu < 0$). In the second part, we incorporate continuous wires and simulate the transmission response of the composite metamaterial (CMM). In this case, we see a transmission band at around the resonance frequency and inspect its double-negative origin. If it was so, the transmission band needed to disappear for the sh-CMM case, in which we had sh-SRRs instead of SRRs and the permeability was not negative. As can be seen in Figure 5.2, below the plasma frequency of the sh-CMM medium there was no transmission band, which implies the double negativity of the designed CMM metamaterial. In general, the QEMT method is preferred if the fabrication the four different media can be processed easily.

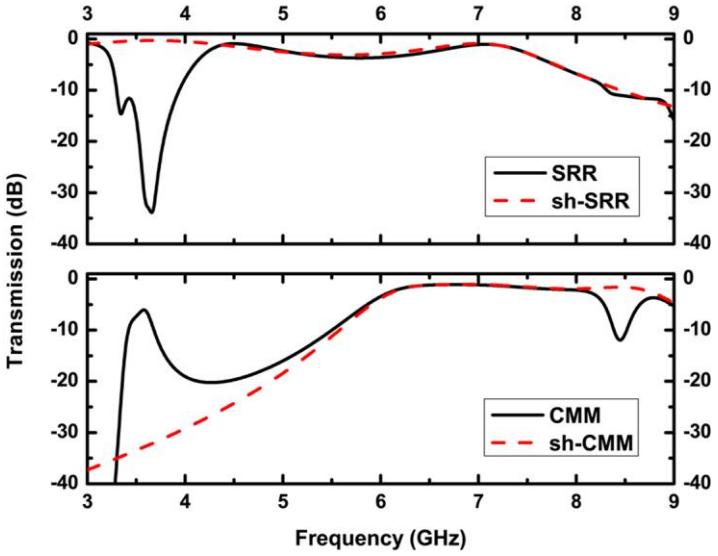

Figure 5.2. Results of the qualitative effective medium theory (QEMT). Transmission response of split ring resonator (SRR) medium, its shorted version (sh-SRR), composite metamaterial medium (CMM) and its shorted version (sh-CMM) are shown.

As we have in fact confirmed that our metamaterial has a negative-index of refraction ($n < 0$) at the double negative transmission band, we can start demonstrating the results of the oblique illumination study. In Figure 5.1(b) a schematic of the experiment setup for the rotation with respect to the y direction is shown. Standard microwave horn antennas were used as the source and sink of the radiation. We measured the transmission response for a spectrum of incidence angles by using an N5230A Vector Network Analyzer and a computer controlled rotary stage. We have shown the results of two different measurements: i) A CMM slab of three layers at the propagation direction, which was rotated with respect to the y-axis with an angle θ ranging from 0° to 45°. ii) The three-layered CMM was rotated with respect to the x-axis with an angle α ranging from 0° to 45°.

5.3. Incident Angle Dependent Transmission Response of SRR Based Metamaterials

Figure 5.3(a) shows that as the angle of incidence increased from 0° to 45°, the negative transmission band only remained with a minor change: peak transmission value had changed on the order of 1 or 2 dB. Moreover, as the angle of incidence increased a narrower and slightly shifted double negative band was observed. Its response remained nearly the same at a considerable fraction of the frequency band. In Figure 5.3(b) we plotted the experimental transmission phase advance for selected incidence angles: 0°, 15°, 30°, 45° and related simulation for 0°. At the negative band, as the incidence angle increased the behavior of the transmission phase remained almost the same, in good agreement with the simulation. In Figure 5.4(a), we show the results for the three-layered case when the incidence angle was varied with respect to the x-axis. The change of the response at the frequency band and angular domain are minor. In this case, the SRRs were excited both magnetically and electrically; therefore, we saw a strengthened transmission response as the angle α increased. At this point, we would like to clarify that the transmission peak for this oblique incidence is indeed due to double negative nature. When the incidence angle with respect to x-axis was 45°, we simulated the response of finite length continuous wire array and the CCMM. There were 20 x-axis unit cells, infinitely periodic y-axis unit cells and 3 unit cells at the propagation direction. In Figure 5.4(b) we show that the plasma frequency of the finite length CCMM medium is around 6.5 GHz and the plasma frequency of the continuous wire medium was higher. Thereby, our metamaterial has negative permittivity for the oblique incidence with respect to x-axis below 6.5 GHz. As we have a transmission band and negative permittivity at around the resonance frequency in Figure 5.4, the medium's permeability has also to be negative as expected.

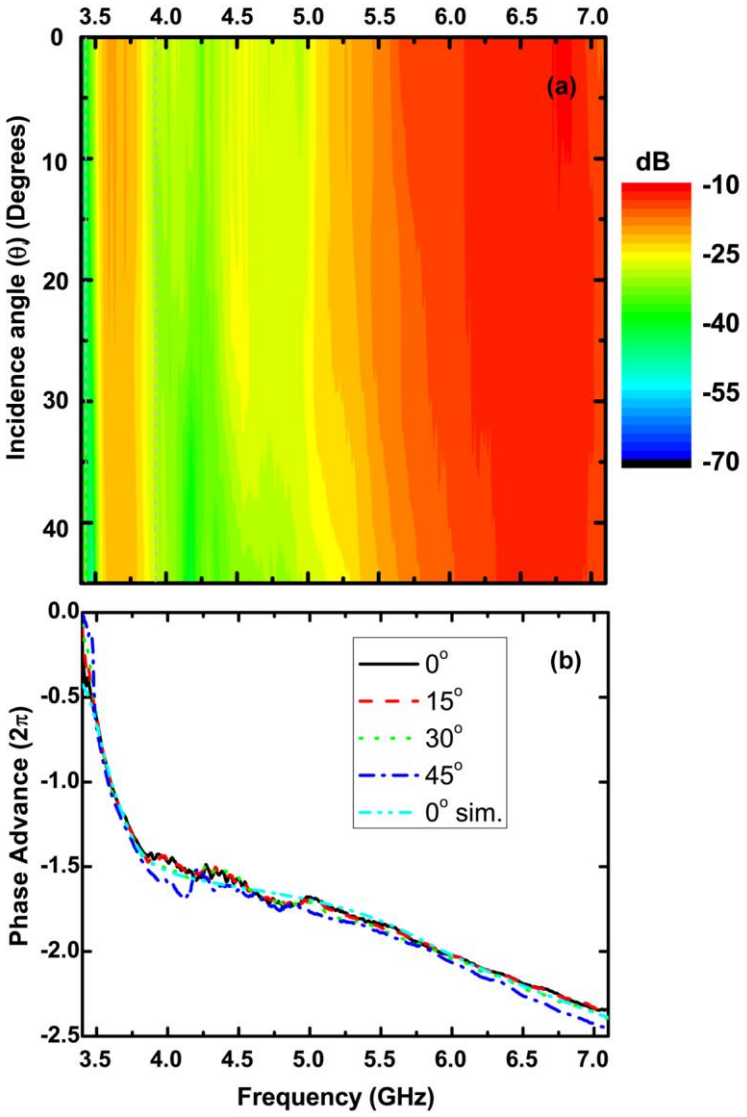

Figure 5.3. (Color online) (a) Experimental transmission spectra as a function of frequency and angle of incidence θ for the three-layered composite metamaterial are shown. The angle θ corresponds to rotation with respect to the **y**-axis. (b) Experimental transmission phase data for selected incidence angles: 0°, 15°, 30°, 45° and corresponding simulation for 0° incidence angle.

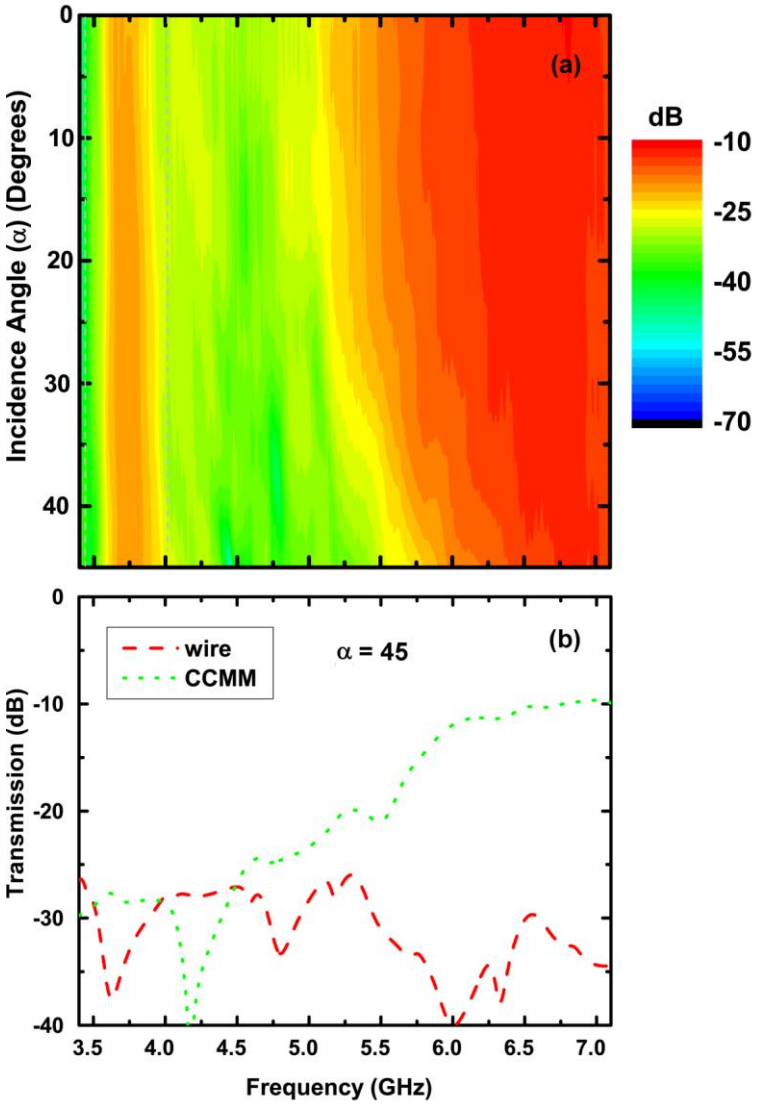

Figure 5.4. (Color online) (a) Transmission spectra as a function of the frequency and angle of incidence α for the three-layered composite metamaterial are shown. The angle α corresponds to rotation with respect to the **x**-axis. (b) Simulated transmission response of a semi-infinite continuous wire array and CCMM for the incidence angle of 45°.

5.4. Oblique Response of Fishnet Metamaterials

We numerically studied the response of the fishnet metamaterial medium to an incident plane wave with a nonzero angle of incidence. In the simulations, we first fixed the number of unit cells to 14 at the horizontal direction (x) and the

infinitely periodic state remains at the vertical direction (y), as shown in the inset of the Figure 5.5. As we rotate the metamaterial layer with respect to the y-direction with a rotation angle θ, we see a shift at the resonance frequency. Therefore, the narrow-band metamaterial does not operate at the same frequency anymore, as shown in Figure 5.5(a). Next, we fixed the number of unit cells at the vertical direction while keeping the infinite periodic condition at the horizontal direction. When the angle of incidence (α) increases, we observe that the negative transmission peak dies out at the operation frequency, which is shown in Figure 5.5(b). From these results we can also see the effect of a finite number of unit cells at one of the lateral directions. The possible reason of the low transmission peaks in the experiment was the nonzero angle of incidence. At this point we would like to emphasize that planar metamaterials are not suitable for superlens [88] applications since their response is very sensitive to the angle of incidence.

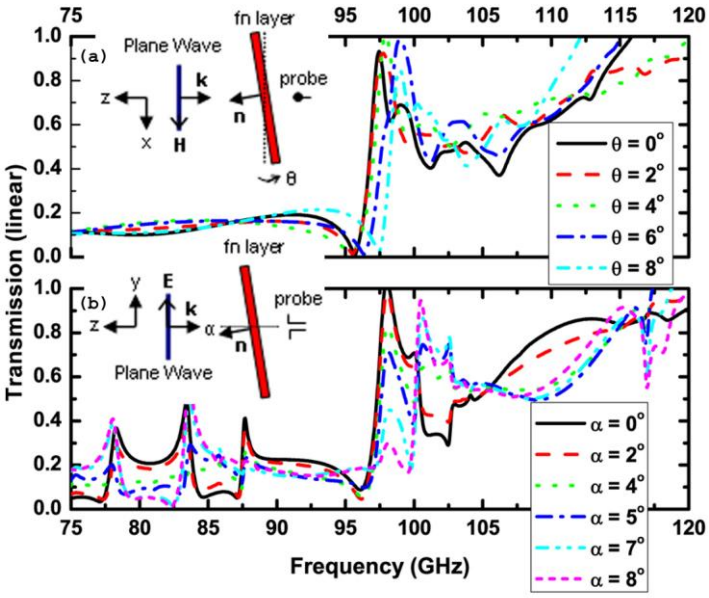

Figure 5.5. Transmission spectra for a number of incidence angles in a linear scale. The metamaterial layer is tilted, and the insets show the simulation configurations (a) H-field makes a 2α angle (b) E-field makes a θ angle with the metamaterial plane normal. The probes measure the E-field.

Chapter 6

Metamaterial Inspired Electrically Small Antennas

6.1. Introduction

The electrical size of an antenna is found by considering a hypothetical sphere that encloses it with a minimum radius (a). We divide the diameter of the sphere to the free space wavelength at the operation frequency (λ) and obtain the electrical size in terms of λ [36, 89, 90]. The electrical size of a regular thin patch antenna is approximately equal to $\lambda/2$ [91]. Passive antennas utilizing metals at frequencies much lower than the metal plasma frequency were demonstrated to have some fundamental limitations [36, 90]. For example, an antenna can be super-directive, if we optimize its directivity at the expense of other desired properties, such as its electrical size and efficiency [90]. Chu derived a relation between the antenna electrical size and its minimum quality factor in the 1940s [36]. Recently, the research conducted on the fundamental limitations of antennas was further clarified in terms of the electrical size and quality factor [92-94].

Metamaterials provided opportunities to enhance the current performance of microwave and optical devices [95, 96]. Their unusual properties and ability to control light in turn inspired researchers to design metamaterial based antennas [9, 10, 97-100]. These antennas' performances were experimentally verified: Buell loaded the ground plane of a patch antenna with a layer of single negative metamaterial and achieved miniaturization factors from *4* to *7* with efficiencies between *20%* and *35 %*. [97]. Hrabar showed miniaturized waveguides loaded

with double split ring resonators that support backward waves below the regular waveguide cutoff frequency [98]. Ermutlu achieved reduction of the patch antenna size from *0.5λ* to *0.38λ*, without degrading its bandwidth by the use of a high impedance surface. Ikonen studied the effect of artificial magneto-dielectric substrates on the impedance bandwidth of microstrip antennas [99, 101]. Quereshi and Alici invented metamaterial based antennas of electrical size *λ/10* with measured efficiencies of *54%* and *43%* [9, 10, 100]. In the present chapter, we further add to the experimentally verified metamaterial based antenna literature by adding the characterization of a negative permeability medium loaded circular patch antenna.

6.1.1. Electrically Small Antenna Characterization Basics

In a two port network, the scattering parameters were measured with a device imbedded between a 50 Ω load and source. For a complete characterization of an antenna that, for example, is connected to port 1 of the network, two scattering parameters are needed: i) input reflection coefficient with the output port terminated by a matched load (S_{11}), ii) forward transmission (insertion) gain with the output port terminated in a matched load (S_{21}). Firstly, we found the radius of the minimum sphere that encloses the antenna. The experimental characterization is performed by the aid of a vector network analyzer, standard horn antennas, automated rotary stages, coaxial cables with 50 Ω characteristic impedance and absorbers. Before the characterization measurements, we performed a full two port calibration.

6.1.1.1. Parameters extracted from the input reflection (S_{11})

The operation frequency antenna under test can be determined from minima of the amplitude of the reflection data. From the S_{11} data as well as the antenna radius (*a*) and operation frequency, we can calculate the antenna electrical size, radiation quality factor (Q), fractional bandwidth (FBW), and -10 dB bandwidth

(BW). The fractional bandwidth is $FBW= \Delta f/f_0$, where Δf is the half power bandwidth and f_0 is the center frequency. The radiation quality factor is a quite important parameter for the performance of electrically small antennas. It is the ratio of the maximum energy stored to the total energy lost per angular period [36, 93]. The minimum Q (Q_{min}) was estimated by the formula [93]: $Q=(2k^3a^3)^{-1}+(ka)^{-1}$. Here, k was the wavenumber at the operation frequency. The radiation quality factor is calculated from the measured reflection data. The Foster reactance theorem is used in this calculation: $Q=1/BW$ [94]. It is noteworthy to check the antenna performance with respect to the Chu limit in terms of the antenna quality factor.

6.1.1.2. Parameters derived from the forward transmission (S_{21})

In the case of the antenna characterization, the S_{21} should be measured either directly at the far field regime or at the near field in order to be transformed to the far field with a procedure. We preferred the latter method in our studies, and characterized the antenna by direct far field measurements at the two characteristic planes. The far field distance (R) was determined as the maximum of 10λ at the operation frequency and $2D^2/\lambda$ where D is the maximum linear dimension of the antenna. We selected a measurement distance that was larger than both of these distances and we used a standard gain horn antenna as a receiver. We show the frequency dependent co-polar angular scan measurement results. From these data, we can see that at the minima of the S_{11} the transmitted power is rather high. We also show cuts from the far field data at specific frequencies that correspond to antenna operation frequencies. The peak gain of the antennas are calculated by using the two antenna method of the absolute gain measurement technique [91]. After the full two port calibration, we first measure the forward transmission for two horn antennas and found gain of the receiver antenna $(G_{0r})_{dB}$ in dB. Then, we replace one of the horns with the antenna under test and find the gain of the transmitting antenna $(G_{0t})_{dB}$. The separation between the antennas is denoted by R in mm. We found the gain of the loaded patch at the

operation frequency (GHz) by using the following formula: $(G_{0r})_{dB} + (G_{0r})_{dB} = 20\ log_{10}(4\pi R/\lambda) + 10\ log_{10}(P_r/P_t)$ where P_r and P_t are the received and transmitted power, respectively. The peak gain is denoted as *Gain* in *dB*.

From the far field pattern cuts, the half power beam widths at the two characteristic planes are obtained and denoted as e.g. θ_{xz} and θ_{yz} in degrees. The maximum directivity of the antenna can be calculated approximately from the following formula: $D_0 = 41253/(\theta_{xz}*\theta_{yz})$. The maximum directivity at the operation frequency is denoted as D_0. The efficiency of an antenna can be calculated from: $G_0(dB) = 10\ log_{10}[e_t D_0(dimensionless)]$.

As the *minQ*, the peak Gain also has a fundamental limit. The analysis was developed by Fante in 1992. In that work, the maximum of *G/Q* was plotted numerically with respect to *ka*. We determine our *ka* for the modes of interest and, then, $(G/Q)_{max}$ is found. We calculate the maximum fundamentally available gain by using: $G_{max} = Q_{min}*(G/Q)_{max}$. Gain, directivity and efficiency of antennas are of fundamental interest and should be calculated for any antenna.

6.2. Single SRR Loaded Monopole Antenna

The SRR is electrically excited with a monopole antenna. The configuration is shown in Figure 6.1, in which the geometrical parameters of the structure are as follows: outer ring radius r_1 = 3.6 mm, inner ring radius r_2 = 5 mm, width of the strips w = 0.9 mm, separation between the two adjacent rings s = 0.2 mm, the length of the splits g = 0.2 mm. Distance to the ground plane h = 0.8 mm, the distance of the end of the radiating inner wire part to the top of the printed circuit board (PCB) t_1 = 0.2 mm, the distance between the PCB and radiating inner wire part of the monopole t_2 = 0.1 mm, thickness of the ground plane d_1 = 0.5 mm, length of the coaxial cable above the ground plane (this part was

necessary for physically strengthening the monopole) d_2 = 0.5 mm, pcb side length h_1 = 7.8 mm, and inner wire height h_2 = 8.32 mm. The coaxial cable has four major parts: the inner wire with a radius of 0.245 mm, Teflon part with a thickness of 1.08 mm and a dielectric constant 2, conducting shield part with a thickness of 0.48 mm and insulator coating with 0.48 mm thickness.

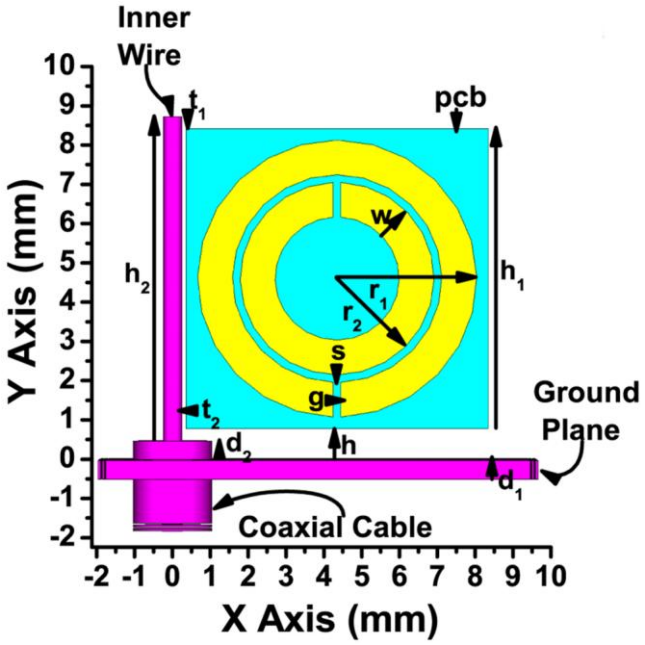

Figure 6.1. The geometry of the SRR antenna is shown, but only a part of the ground plane and the coaxial cable.

The substrate PCB was standard FR-4 material with relative permittivity $\varepsilon_r = 3.5$. The thickness of the PCB was 1.6 mm and the deposited copper thickness on the PCB was 30 µm. SRR was obtained by properly etching the metal deposit of the PCB. The ground plane is nearly square shaped at the x-z plane with the square side length being equal to the free space wavelength (λ_0) at the operation frequency (f_0). The operation frequency is selected to be the frequency at which the SRR shows resonant behavior. This frequency is determined as 3.62 GHz by considering the minimum of the input reflection coefficient, S_{11}. The antenna is simulated by using the commercial software: Computer Simulation Technology, Microwave Studio (CST MWS). The

experiments are performed via an HP8510C Network Analyzer. The simulation and experiment data of the S_{11} are presented in Figure 6.2. The minimum of the S11 data of the reflection experiment was -32 dB.

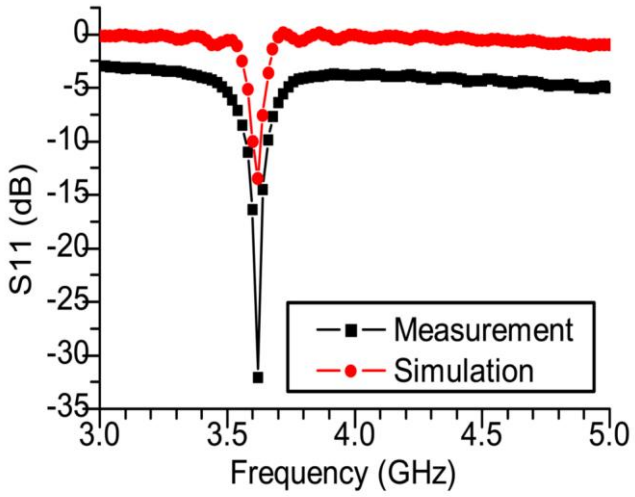

Figure 6.2. Amplitude of S_{11} for the SRR antenna, experiment and simulation.

The overall size of the antenna part is 0.095 λ_0 x 0.100 λ_0. Since the antenna part is above a conducting plane while defining the radius of the minimum sphere that encloses the antenna, we should also, therefore, consider the antenna's image [92]. Therefore, the minimum radius a for our antenna is 0.144 λ_0 i.e. 11.95 mm. The radiation quality factor of an ESA is of fundamental interest. We estimate the minimum radiation quality factor of the antenna as minQ = 1.78. The Q of the antenna was calculated by using the Foster's Reactance Theorem [94]. The fractional bandwidth (FBW) and -10 dB BW are obtained from the experimental S11 data as 0.043 and 2.42%, respectively. Therefore, the Q ~ 1/BW is 23.03 and is adequately large [102] and well above the theoretical limit.

The far field radiation pattern measurements were performed by using a standard gain horn antenna as a receiver. The distance between the antennas was ~ 1 meter, which corresponds to the far field region for our antenna. The

measured and simulated co-polarized E- and H-Plane far field radiation patterns are presented in Figure 6.3. We see that the simulated and measured far field patterns are similar, however, the simulation predicts symmetric side lobe levels for the H-Plane pattern. We couldn't be able to see this symmetry due to experimental limitations. The approximate value of the maximum directivity is calculated by using the half-power beamwidths in degrees. The measured half power beamwidth was 76° along the E-Plane and was 92° along the H-Plane. The absolute gain measurements are followed by the two antenna method calculations, in which we obtained the antenna gain as G = 2.38. The corresponding radiation efficiency of the antenna was 43.6%. The figure of merits of the antenna obtained from the measurements and simulation are summarized in Tables 6.1 and 6.2 listed at the end of the next section. Finally, we should compare the gain of our antenna with the fundamental limit given by Fante [103]. The maximum possible gain for our antenna estimated from the Fante's analysis is 4.51. We see that our gain is less than the theoretical limit.

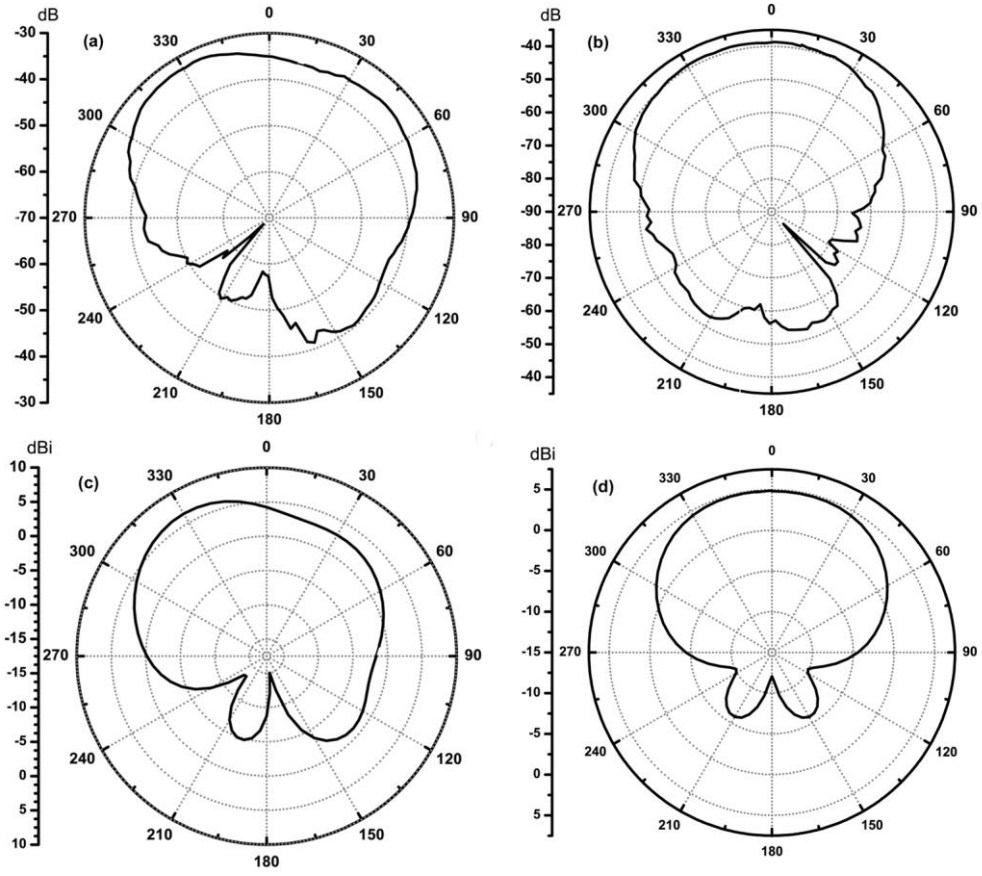

Figure 6.3. Far field radiation patterns of the SRR antenna, (a) E- Plane measured (x-y plane), (b) H- Plane measured (y-z plane), (c) E- Plane simulated, (d) H- Plane simulated.

6.3. Fundamental Limits of SRR Loaded Monopole Antennas

If we can excite the SRR electrically at rather small frequencies, the antenna size can be further miniaturized since the SRR resonance frequency can be tuned by increasing the capacitance between the rings. Considering this fact we designed serrated SRR, which has a resonance at 2.84 GHz. Just by changing the shape of the rings as shown in Figure 6.4 we obtained a smaller SRR antenna. However, though the size is smaller, the maximum theoretical gain is thereby reduced to 2.33. Correspondingly, the antenna efficiency was then 18.8%. The calculated

figure of merits are presented in Tables 6.1 and 6.2. The simulation results for the insertion loss and the far field radiation patterns are shown in Figure 6.4 and Figure 6.5, respectively.

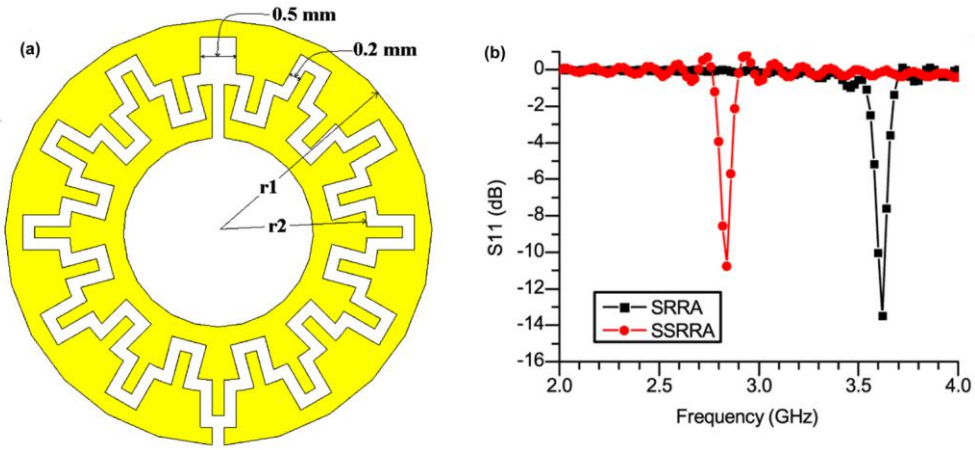

Figure 6.4. (a) Serrated SRR geometry, (b) Insertion loss for the SSRR antenna and SRR antennas.

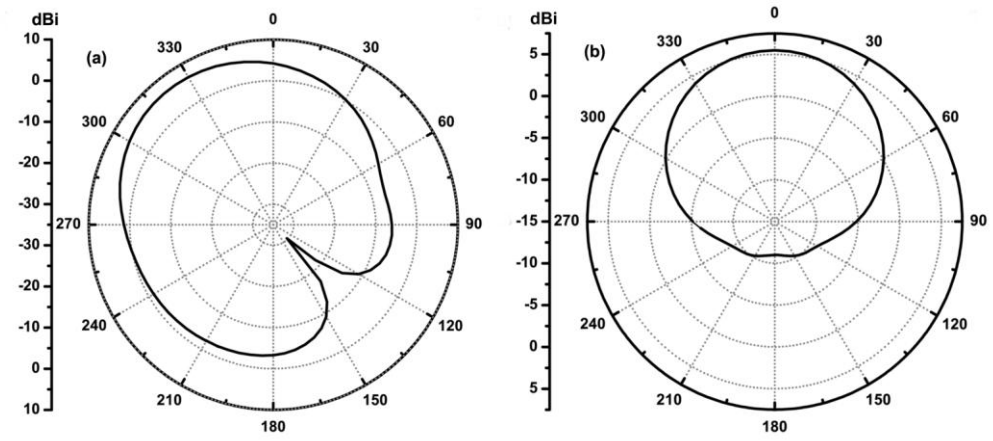

Figure 6.5. (a) E- Plane and (b) H- Plane simulated patterns of the SSRR antenna.

	Freq. (GHz)	Size	FBW (%)	Rad Q	Min Q	-10 dB BW
SRRA Exp.	3.62	0.095 λ_0 x 0.100 λ_0	4.3	23.03	1.77	2.42 %
SRRA Sim.	3.62	0.095 λ_0 x 0.100 λ_0	2.8	36.20	1.77	0.88 %
SSRRA Sim.	2.84	0.074 λ_0 x 0.079 λ_0	2.9	34.63	2.79	0.35 %

Table 6.1. Antenna figures of merit extracted from reflection amplitude.

	a	G_{max}	Gain	D_0	Efficiency
SRRA Exp.	0.144 λ_0	4.51	2.38	5.90	43.6 %
SRRA Sim.	0.144 λ_0	4.51	3.11	4.95	62.8 %
SSRRA Sim.	0.113 λ_0	2.33	1.06	5.63	18.8 %

Table 6.2. Antenna figures of merit extracted from transmission amplitude.

6.4. 1D SRR Loaded Monopole Antenna

Antennas composed of single negative materials that resonantly couple to external radiation was invented by Isaacs [104]. Even if the radiation wavelength is much larger than the antenna size, the antenna is sensitive to radiation due to the resonant coupling. By feeding such a resonator one can obtain an electrically small antenna when operating at microwave frequencies. This was the basic idea of our study in the previous sections of this chapter. In the present section we would like to demonstrate the one-dimensional array of SRR loaded monopole antennas.

We start with the single SRR case. We used the SRR depicted in Figure 6.6. Its geometrical parameters are R = 3.6 mm, r = 2.5 mm, g = w = 0.2 mm, t = 0.9 mm. The substrate is the standard FR-4 material with a thickness of 1.6 mm, relative permittivity 3.85 at 4 GHz, and a loss tangent 0.008 at 3 GHz. The SRR is fabricated by etching the deposited 30 μm thick copper. We excited the SRR by using a monopole antenna Figure 6.6(b). A monopole antenna is composed of

a coaxial cable, ground plane, and radiating wire part. We used an SSI 0413 coaxial cable with an inner wire radius a = 0.49 mm, Teflon thickness b = 1.08 mm, shield thickness c = 0.48 mm, and insulator coating thickness d = 0.48 mm, as shown in Figure 6.6(c). The Teflon dielectric constant was 2.2, in which the cable can transmit the TEM mode waves up to 65 GHz safely. The ground plane material is aluminum and is connected to the shield by a conducting paste. It is 0.5 mm thick and has a square shape with an edge length that is equal to the free space wavelength. The operation frequency was 3.52 GHz, which was determined by considering the SRR's geometrical parameters. The corresponding free space wavelength (λ) was 85.17 mm. The length of the wire above the ground plane was 8.32 mm and for the monopole antenna this length corresponds to a quarter of the operation wavelength. Thus this monopole antenna was working efficiently when feed wavelength was 33.28 mm and feed frequency was 7.8 GHz. Therefore, the SRR resonance frequency is smaller than the monopole operation frequency. The SRR is positioned rather close to the radiating wire part of the monopole antenna. At the operation frequency, 3.52 GHz, the wire part and SRR behave as a composite radiating structure. The characteristic impedance of the coaxial cable and wire SRR composite becomes very close, in which the surface currents on the SRR increase an order of magnitude and the structure starts to radiate efficiently.

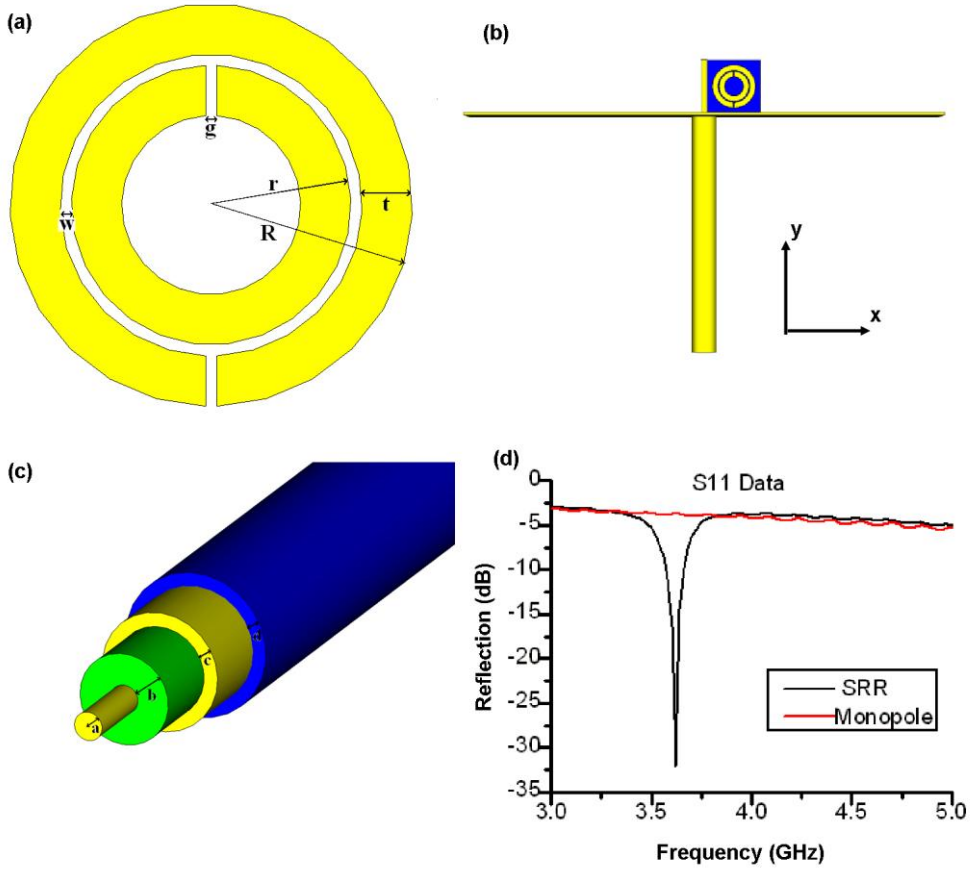

Figure 6.6. (a) Schematics of an SRR, (b) Schematics of the SRR inserted monopole antenna, (c) Schematics of the coaxial cable, (d) Measured S_{11} amplitude for the monopole and monopole SRR composite.

For the theoretical calculations, we simulated the structure via the commercial program: Computer Simulation Technology Microwave Studio (CST MWS). There was a considerable change at the $|S_{11}|$ and at the surface current at the operation frequency with respect to a non-resonant frequency. $|S_{11}|$ reduced to –30 dB from –3 dB and the surface current increased from 90 A/m to 2460 A/m. For the experimental demonstration, we used an HP8510C Network Analyzer. After a full two port calibration we measured the monopole antenna $|S_{11}|$ in order to determine its efficient operation frequency, which is 7.8 GHz. Subsequently, we measured the $|S_{11}|$ parameter between 3 GHz and 5 GHz, as

shown in Figure 6.6(d). We observed that the composite to be a –32 dB $|S_{11}|$ value.

We also obtained the far field radiation patterns of the structure by using the simulation results. The structure radiates similar to a single element patch antenna. The 3D far field view and corresponding E-plane and H-plane patterns are shown in Figure 6.7. Main lobe direction was 115°, and the directivity is 6.53 dBi. In order to show that the effect is purely due to the magnetic resonance of the SRR, we also reveal the closed split ring resonator (CRR) results. CRR has the same parameters as SRR but the splits are closed. We consider the same planes as the SRR monopole composite. The CRR insertion does not have an effect on the monopole, on the other hand, SRR insertion entirely changes the antenna characteristics.

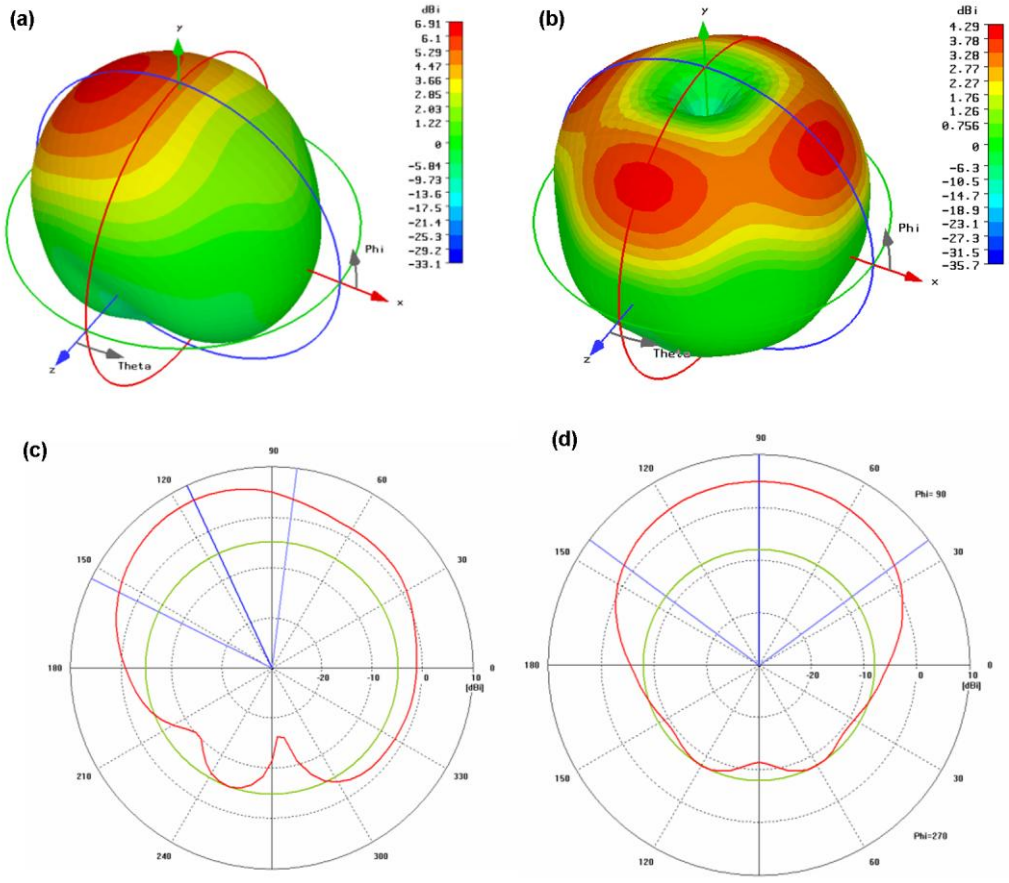

Figure 6.7. Far field pattern of the SRR monopole composite: (a) 3D view, (c) E-plane cut (x–y plane), (b) Far field pattern of the monopole (3D view), (d) H-plane cut (y–z plane).

In order to estimate the radiation efficiency of the antennas we performed the absolute-gain measurements [91]. The gain of the SRR monopole composite antenna is found by comparing it with a standard horn antenna. Two-antenna method is applied and the gain of the 1 SRR loaded monopole is found as Gain = 2.35 at 3.62 GHz. At this frequency we had minimum return loss ($|S_{11}|$). The far field radiation pattern cuts are measured by the aid of the horn receiver antenna. The half-power beamwidths of the E- and H- plane patterns implied the directivity of the antenna as 5.48 dBi [91]. And finally we estimated the efficiency as 42.88%. For the multi SRR cases measured gains were almost the same as 1 SRR case. The simulations of the multi SRR cases show that directivity of these antennas is almost the same as the 1 SRR case also.

Therefore we can safely conclude that efficiencies of the multi-SRR and 1 SRR antennas have similar values. These results indicate that the composite antenna has good coupling efficiency and enough radiation efficiency.

We also considered multi-SRR effects on the radiation pattern. By coupling 2, 3, and 4 SRRs side by side, we calculated the radiation patterns. The dependence of coupling on the arrangement of the SRRs was studied in the literature [105]. Here, SRRs are placed side by side with an 8.8 mm period Figure 6.8. The measured and simulated $|S_{11}|$ parameters indicated that the arrangement of multi-SRRs in this way does not change the operation frequency considerably. There is a small shift with respect to the 1 SRR case. Metamaterial transmission lines can implement steerable leaky wave antennas [106-108]. We observed that by increasing the number of SRRs in the x- direction, the E-plane beam maximum shifts considerably. The corresponding E-plane far field patterns are shown in Figure 6.9. Therefore, by changing the resonator numbers in the antenna, we can attain the steerability property.

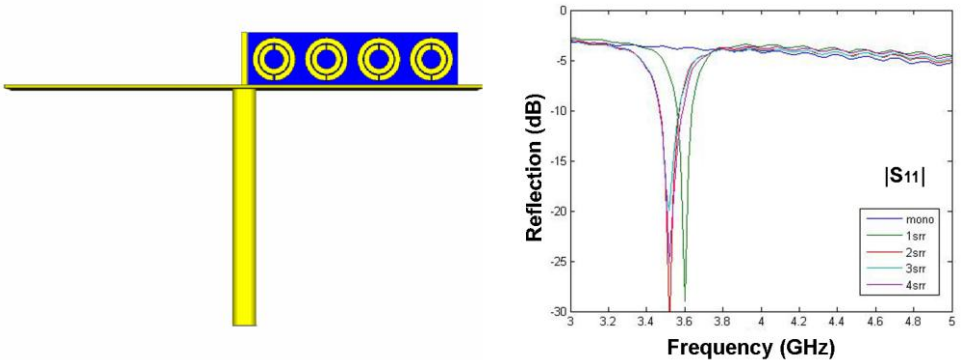

Figure 6.8. Schematic of 4 SRR loaded monopole (left). Measured $|S_{11}|$ data for several number of SRRs and monopole (right).

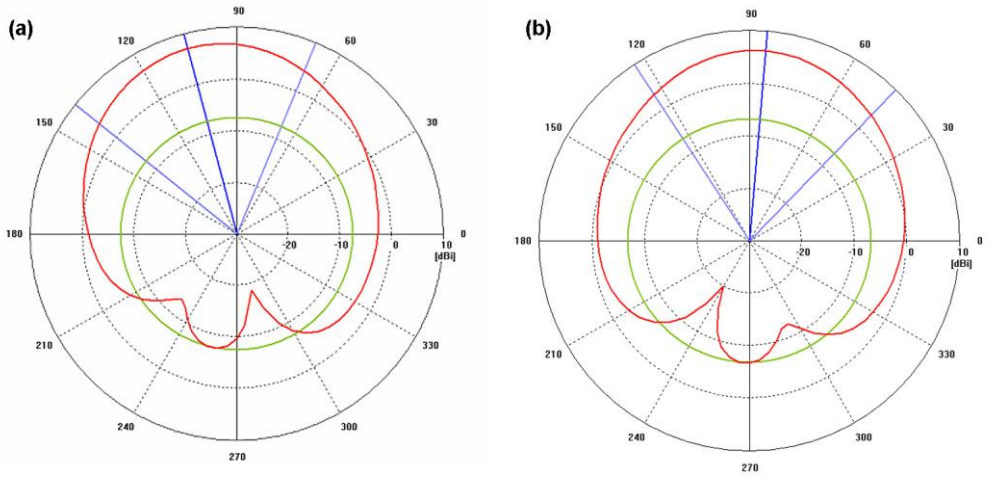

Figure 6.9. Multi SRR effects. (a) 2 SRRs (main lobe direction = 110°). (b) 4 SRRs (main lobe direction = 100°).

6.5. Dual Mode MSRR Loaded Monopole Antenna

An antenna under test (AUT) can be experimentally characterized by using a network analyzer. The configuration of our AUT is shown in Figure 6.10. We loaded the monopole antenna simultaneously with two electrically small metamaterial elements. We placed the SRR composed of 1 split ring parallel to the yz-plane. We had the MSRR with the same side length in the xz-plane, the number of rings (N) of the MSRR was 5. The other parameters were as follows: resonator side length, l = 4 mm, separation between the rings, s = 0.2 mm, width of the strips, w = 0.2 mm, split width, g = 0.2 mm, thickness of the deposited metal, h = 0.018 mm, substrate (FR-4) thickness, t = 1 mm. The listed relative permittivity of FR-4 was ε_r = 4.9 with a dissipation factor tanδ = 0.02. The coaxial SMA connector was soldered to the ground plane from the bottom and the metamaterial particles were mechanically connected to the ground plane by using comb shaped FR-4 holders. We connected the antenna to an antenna holder from the corners of the ground plane for the characterization measurements.

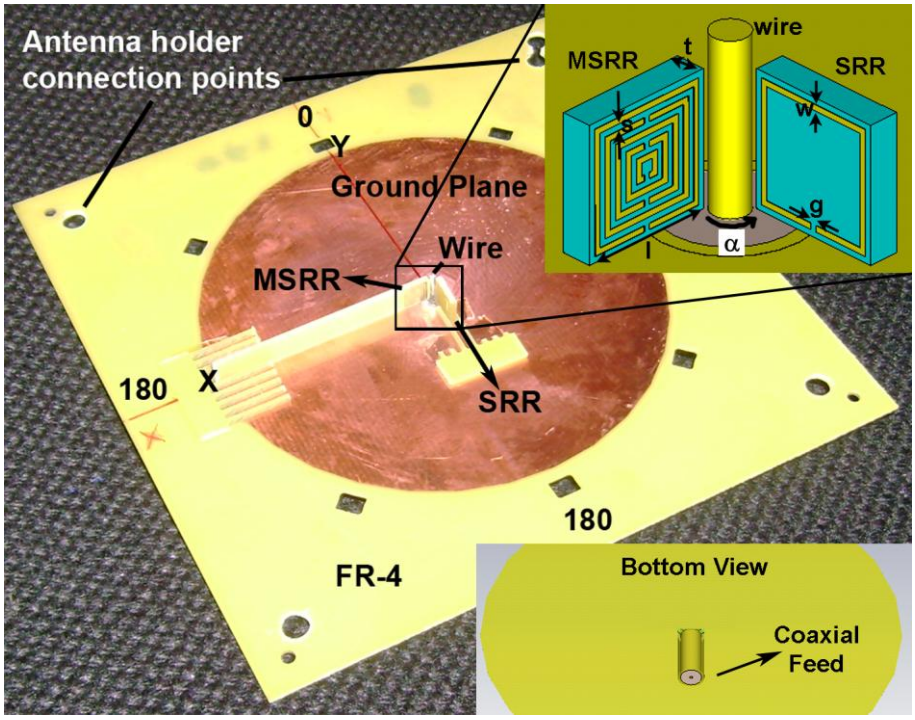

Figure 6.10. Antenna photograph and geometry of the loading resonators.

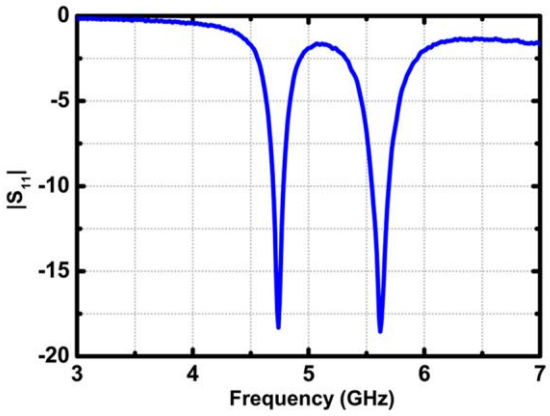

Figure 6.11. Return loss ($|S_{11}|$) of the antenna in logarithmic scale.

The minima of the S_{11} magnitude show us at which frequencies the antenna is matched to free space. These frequencies are the operation center frequencies of the antenna and determined as 4.74 GHz (MSRR mode) and 5.62 GHz (SRR mode). As the resonators were perpendicular to each other, their coupling was

minimal and these operation frequencies were close to the resonance frequencies of SRR and MSRR media as determined by transmission measurements. The half power bandwidths were 300 MHz and 520 MHz, and thereby the fractional bandwidths were 0.063 and 0.093 at 4.74 GHz and 5.62 GHz, respectively. The electrical size of the antenna for each mode was calculated as $\lambda/11.2$ and $\lambda/9.5$ for the MSRR and SRR modes. By using the Q_{min} formula, we estimated the minimum antenna quality factors as $Q_{min\text{-}MSRR} = 4.5$ and $Q_{min\text{-}SRR} = 3.2$. Now let us compare our antenna factor with the theoretical limit (Q_{min}). The Q-factors were 15.9 and 10.8 for the MSRR and SRR modes, and they were within the same order of magnitude with the theoretical limits. We tabulated these data in Table 6.3. In order to determine the antenna efficiency, figures of merit need to be extracted from the S_{21} parameter also.

	Freq. (GHz)	a (mm)	u	ka	FBW	Rad Q	Min Q
MSRR	4.74	5.66	$\lambda/11.2$	0.57	0.063	15.9	4.5
SRR	5.62	5.66	$\lambda/9.5$	0.67	0.093	10.8	3.2

Table 6.3. Figures of merit extracted from the return loss ($|S_{11}|$) data.

We measured S_{21} directly at the far with a standard gain horn antenna of rectangular aperture. In Figure 6.12, we showed the frequency dependent angular co-polar and cross-polar far field patterns. The patterns were not scaled to peak gain. Note that the co-polar pattern of MSRR mode is a cross-polar pattern of the SRR mode and vice versa. In Figure 6.12, parts (a) and (c), we have SRR co-polar patterns at the x-z and y-z planes, respectively. Similarly, in Figure 6.12 parts (b) and (d), we had MSRR co-polar patterns at the y-z and x-z planes, respectively. We can clearly conclude from these data that while one mode was operating for a polarization, the other one was inactive and vice versa. The difference between the co- and cross-polar patterns for the MSRR mode was 14.6 dB and, for the SRR mode, it was 15.9 dB. We can identify the gain of the antennas by using absolute gain measurements [91]. We estimated the gain

of the MSRR mode as -0.8 dB, and the SRR mode as -0.5 dB. Fante studied the maximum gain of an antenna with respect to ka. We had ka_{MSRR}= 0.57, and $Q_{min-MSRR}$ = 4.5 and thereby the maximum theoretical gain was $G_{max-MSRR}$ ~18. For the SRR mode ka_{SRR} = 0.67 and $Q_{min-SRR}$= 3.2 and the $G_{max-SRR}$~16. Before calculating the efficiency, we finally needed to investigate the directivity of the antenna at the two dual modes.

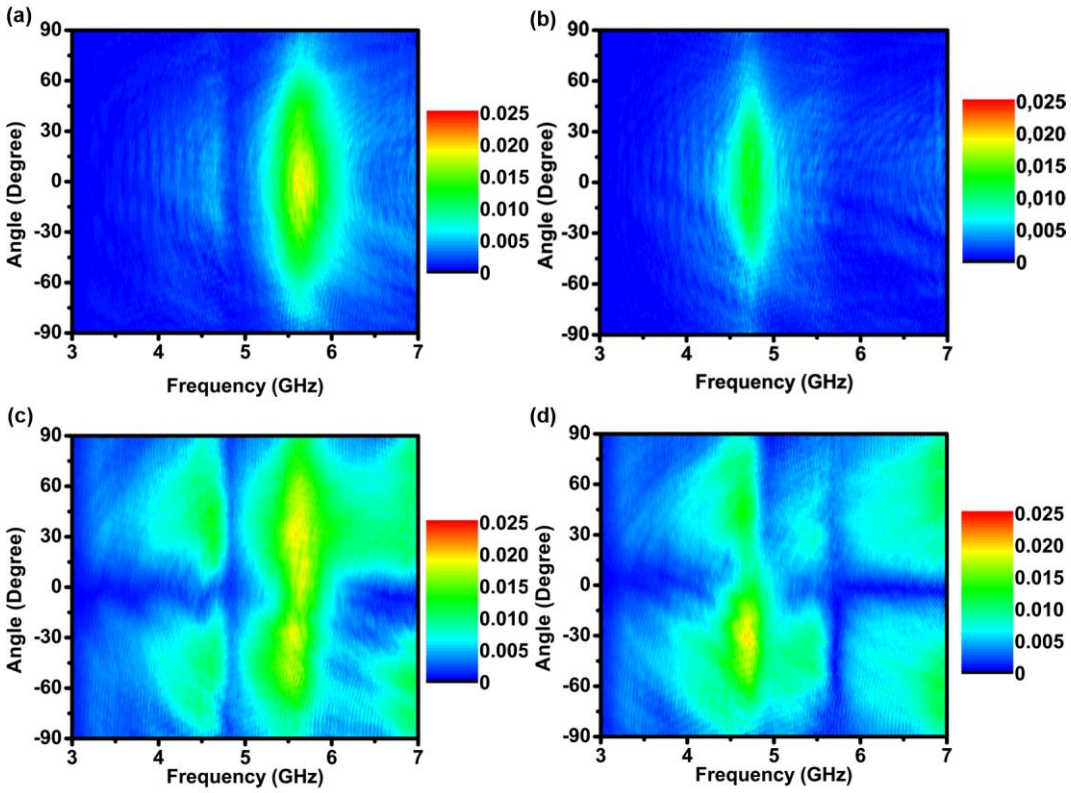

Figure 6.12. Frequency and angle dependent far field transmission data. SRR co-polar patterns (a) x-z plane (c) y-z plane. MSRR co-polar patterns (a) y-z plane (c) x-z plane.

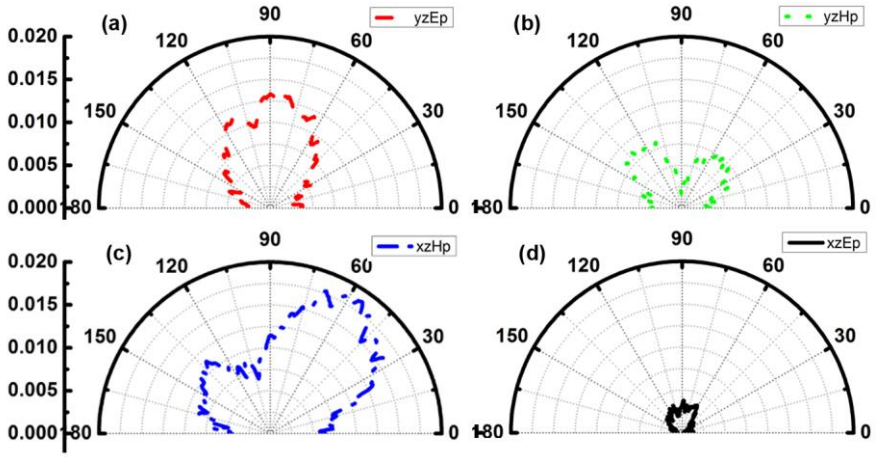

Figure 6.13. Far field transmission pattern cuts for the MSRR mode at 4.74 GHz. (a) E-field of the horn antenna was parallel to the y-z plane. (b) H-field of the horn antenna was parallel to the y-z plane. (a) and (c) were co-polar patterns, (b) and (d) were cross-polar patterns.

In Figures 6.13 and 6.14, the far field pattern cuts are shown at the operation frequencies of the two modes. In Figure 6.13 (a) and (c) the co-polar; (b) and (d) cross-polar patterns are shown for the MSRR mode. In Figure 6.14 (b) and (d) the co-polar; (a) and (c) cross-polar patterns are shown for the SRR mode. The calculated the half power beam widths (θ) are listed in Table 6.4, in which the directivities of the modes were $D_{0\text{-MSRR}} = 5.6$ and $D_{0\text{-SRR}} = 2.2$.

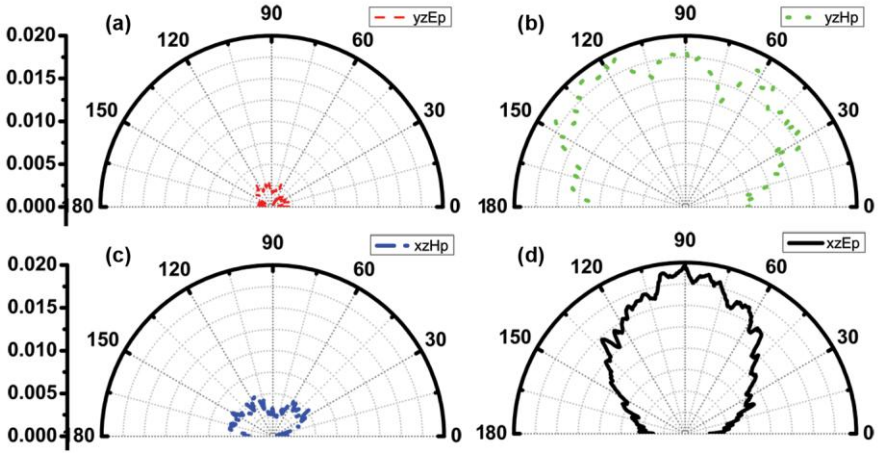

Figure 6.14. Far field transmission pattern cuts for the SRR mode at 5.62 GHz. (a) E-field of the horn antenna was parallel to the y-z plane. (b) H-field of the horn antenna was parallel to the y-z plane. (a) and (c) were cross-polar patterns, (b) and (d) were co-polar patterns.

	Freq. (GHz)	G_{max}	Gain (dB)	θ_{xz}	θ_{yz}	D_0	Efficiency
MSRR	4.74	~18	-0.8	78^o	94^o	5.6	15%
SRR	5.62	~16	-0.5	111^o	166^o	2.2	40%

Table 6.4. Figures of merit extracted from the forward transmission (S_{21}) data.

The total efficiency of the antenna was estimated as $e_{t\text{-}MSRR}$ = 15% and $e_{t\text{-}SRR}$ = 40% by the formula: $G_0(dB) = 10 \log_{10}[e_t D_0(\text{dimensionless})]$.

6.6. 2D MSRR Loaded Circular Patch Antenna

In the present section, we further add to the experimentally verified metamaterial based antenna literature by adding the characterization of a negative permeability medium loaded circular patch antenna. The efficient operation of a μ-negative medium loaded circular patch antenna at the subwavelength regime was predicted by using the cavity model [109]. The necessary conditions in terms of the filling ratio of the volume underneath the patch and the permeability of the filler metamaterial medium were determined by cavity analysis. By keeping in mind its unit cell properties, we identified the possible radii of the cylinder shaped μ-negative media. Our metamaterial elements that we used in this study were recently developed multi-split ring resonators (MSRRs) and spiral resonators (SRs). Depending on the resonator parameters, we can have a wide range of operation frequencies.

The antenna was composed of a ground plane, circular patch, and perpendicularly oriented MSRR layers in between. As shown in Figure 6.15, there were closely packed *8* MSRR layers with 1, 2, 3, and 4 unit cells in the *x*-direction. We formed a circle-like shaped MSRR medium with the radius, *r = 6.8mm*. The ratio of the patch and MSRR medium radii was *R/r =10/6.8 = 1.47*. The metamaterial cylinder was covered with air, in turn mimicking the proposed

interface of μ-negative - μ-positive media. The relative permeability of air μ_{air} = *1* and the relative permeability of the metamaterial medium shows a Lorentzian behavior of obtaining positive and negative values at different frequency bands [110]. For the demonstration of this antenna, we selected a specific MSRR with the following parameters: side length, *l = 3.2 mm*, number of rings, *N = 8*, separation between the rings, *s = 0.1mm*, width of the strips, *w = 0.1 mm*, split width, *g = 0.1 mm*, thickness of the deposited metal, *h = 0.018mm*, substrate thickness, *t = 1mm*. The listed relative permittivity of FR-4 was ε_r = *4.9* with the dissipation factor *tanδ = 0.02*. The coaxial SMA connector was soldered to the ground plane from the bottom and the feed wire was soldered to the patch from the top. The metamaterial layers were mechanically connected to the ground plane via FR-4 sticks and grids. The feed point was approximately *2.5 mm* away from the patch edge. We connected the antenna to an antenna holder from the corners of the ground plane for the characterization measurements.

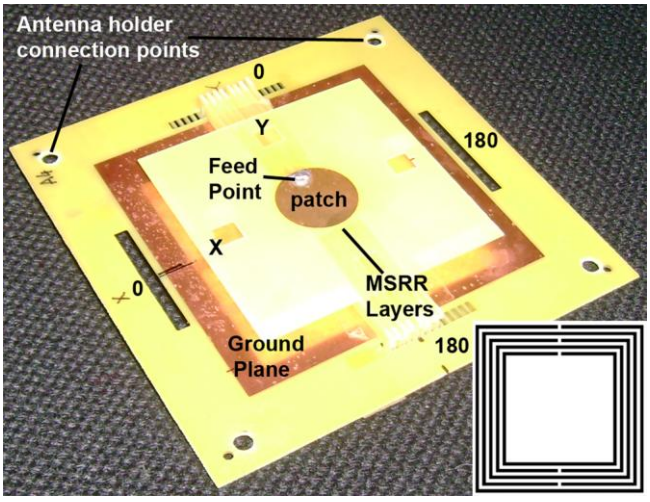

Figure 6.15. Manufactured antenna photograph and multi-split ring resonator geometry.

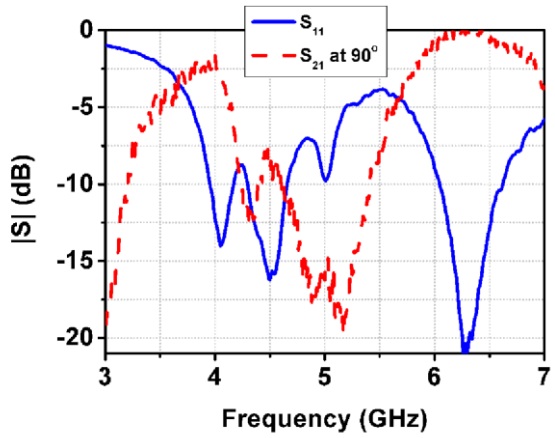

Figure 6.16. Magnitude of the input reflection coefficient ($|S_{11}|$) and co-polar far field transmission at 90°.

Firstly, we found the radius of the minimum sphere that encloses the antenna. The minimum radius for this antenna was $a= (10^2+3.4^2)^{0.5}= 10.56\ mm$. Around the resonance frequency (*4.5GHz*) of the MSRRs, we investigated antenna operation at 4 four different modes: *3.85 GHz*, *4.49 GHz*, *5.07 GHz*, and *6.26 GHz*, which are very close to the minima of the magnitude of the reflection data. From the S_{11} data, as shown in Figure 6.16, as well as the antenna radius (a) and operation frequency, we can calculate the antenna electrical size, radiation quality factor (Q), fractional bandwidth (FBW), and -10 dB bandwidth (BW). Here, due to the coupling of several modes, it was not trivial to calculate the FBW. Therefore, for the determination of FBW, we also considered the normalized far field forward transmission at 90°, as shown in Figure 6.16 as a dashed curve. The radiation quality factor is a quite important parameter for the performance of electrically small antennas. For the first mode (*3.85 GHz*) of the antenna, the minimum quality factor was $Q_{min}=1.98$. We showed the calculated figures of merit for the other modes in the Tables 6.5 and 6.6 of the next section. Moreover, the radiation quality factor that was calculated from the measured data of Figure 6.16 was $Q_{rad} = 5.42$. The FBW and electrical size at the first mode were *0.18* and $\lambda/3.69$, respectively. It is noteworthy that the antenna was close to the Chu limit in terms of the antenna quality factor.

In Figure 6.17, we showed the frequency dependent co-polar angular scan measurements that were not normalized to peak gain. From these data, we can see that at the minima of the S_{11} the transmitted power is rather high. In Figure 6.18, part (a), we showed the x-y plane cut, and in Figure 6.18, part (b), the y-z plane cut was shown. We plotted cuts from the 2D field patterns at the mentioned operation frequencies. These patterns were scaled to the maximum gain. The peak gain of the antennas were calculated by using the two antenna method of the absolute gain measurement technique [91]. The separation between the antennas was $R = 800\ mm$. We found the gain of the loaded patch at $3.85\ GHz$ as $Gain = 4.42\ dB$.

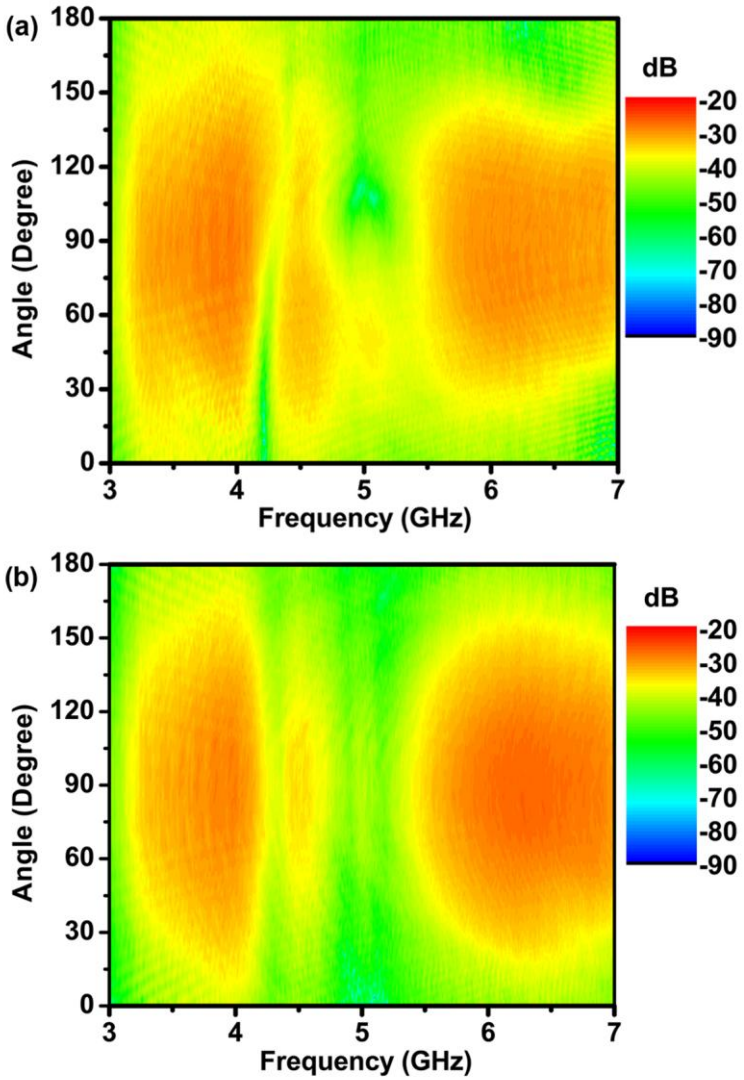

Figure 6.17. Frequency dependent angular far field patterns (a) y-z plane (b) x-z plane.

From the far field pattern cuts, the half power beam widths at the two characteristic planes were obtained as $\theta_{xz} = 73.5°$ and $\theta_{yz} = 82$. The maximum directivity at 3.85 GHz was $D_0 = 6.84$. The efficiency of an antenna at 3.85 GHz was 40%.

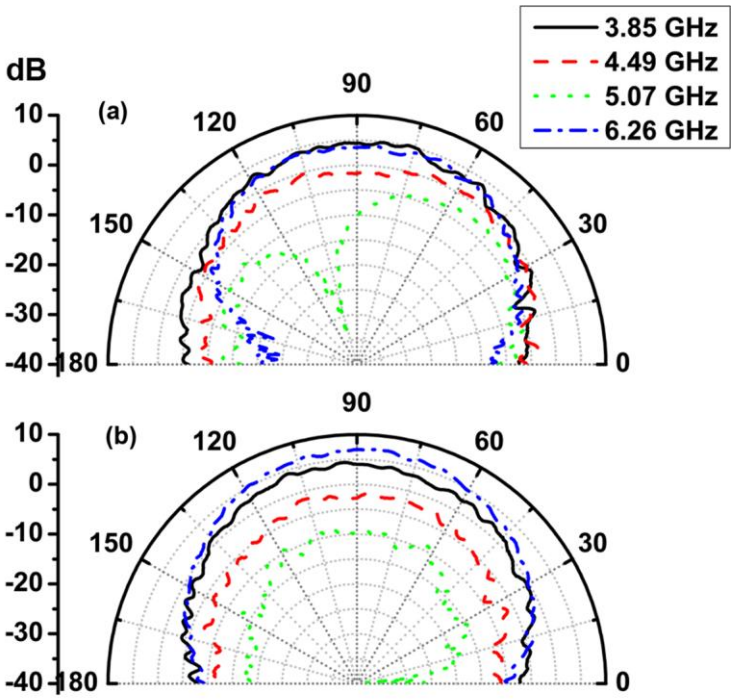

Figure 6.18. Far field pattern cuts at several operation modes (a) y-z plane (b) x-z plane.

As the *minQ*, the peak Gain also has a fundamental limit. Our *ka* was around 1 for the modes of interest and, therefore, $(G/Q)_{max}$ was around *10* [103]. The maximum peak gain for our antenna was approximately $G_{max} = 17$. Our efficiency was *40%* and the minimum quality factor was close to the Chu limit. The performance of this antenna will be acceptable for applications. Loading patch antennas with a metamaterial medium improves the current standards of electrically small antennas.

We plotted the characterization parameters at the other frequency modes in Tables 6.5 and 6.6 for reference. At *6.26 GHz*, the gain and thereby the efficiency of the antenna were rather high with respect to the first mode, but the antenna's electrical size was *1.6* times larger. While studying the electrically small metamaterial elements, we focused on achieving smaller electrical sizes of resonators. Can we further reduce the electrical size of the patch antenna by using the spiral resonators?

6.7. 2D SR Loaded Circular Patch Antenna

In this example, we used the same mechanism and constructed a circular patch antenna loaded with spiral resonators. The spiral resonator parameters were as follows: the side length, *l = 5 mm*, number of turns, *N = 5*, separation between the strips, *s = 0.1mm*, width of the strips, *w = 0.1* mm, thickness of the deposited copper metal, *h = 0.009mm*, substrate thickness, *t = 0.254mm*. The listed relative permittivity of Rogers RT/duriod substrate is $\varepsilon_r = 2$, with a loss tangent of $tan\delta = 0.0009$. The coaxial SMA connector was soldered to a *0.5mm* thick ground plane from the bottom and the feed wire was soldered to the patch from the top. The metamaterial layers were placed, via types, between the patch and ground plane. The feed point was approximately *5 mm* away from the patch edge. A photograph of this antenna is shown in Figure 6.19. This time, we were only able to demonstrate the S_{11} related parameters due to the experimental limitations at low frequencies.

	Freq. (GHz)	a (mm)	u	ka	FBW	Rad Q	Min Q
A1-Mode1	3.85	10.56	λ /3.69	0.85	0.18	5.42	1.98
A1-Mode2	4.49	10.56	λ /3.16	0.99	0.07	14.03	1.52
A1-Mode3	5.07	10.56	λ /2.80	1.12	0.05	20.28	1.25
A1-Mode4	6.26	10.56	λ /2.28	1.38	0.19	5.13	0.91
A2-Mode1	0.88	20.62	λ /8.26	0.38	0.04	28.38	11.72

Table 6.5. Figures of merit extracted from the input reflection (S_{11}) data.

	Freq. (GHz)	G_{max}	Gain (dB)	D_0	Efficiency
A1-Mode1	3.85	17.84	4.42	6.85	40%
A1-Mode2	4.49	15.16	0.76	5.15	23%
A1-Mode3	5.07	13.70	-1.92	12.79	5%
A1-Mode4	6.26	11.83	7.11	7.54	68%
A2-Mode1	0.88	-	-	-	-

Table 6.6. Figures of merit extracted from the forward transmission (S_{21}) data

The minimum radius of the antenna was $a = 20.62\ mm$ and the S_{11} data is shown in Figure 6.20. The ratio of the patch and SR medium radii was $R/r = 20/14 = 1.43$. Similar to the MSRR loaded antenna, we also observed the modes at the frequencies close to the resonance frequency of the SRs. However, this time the antenna of the first mode was at $0.88\ GHz$ and the electrical size was $\lambda/8.3$. The figure of merits was as follows: the $FBW = 0.035$, $minQ = 11.7$, $Q_{rad} = 28.4$. The minimum quality factor was again close to the best performance as determined by the Chu limit. This time we cannot include the S_{21} analysis that is to be discussed in the next session.

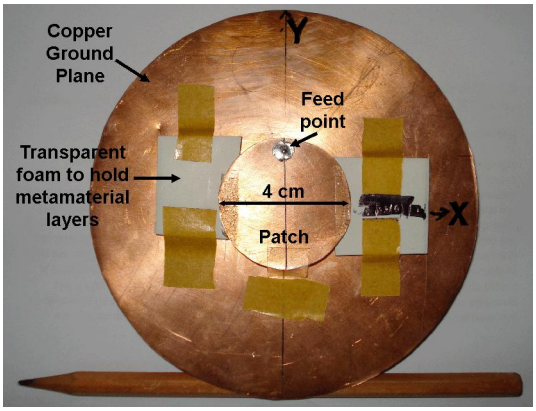

Figure 6.19. Top view of the spiral resonator loaded copper based patch antenna photograph.

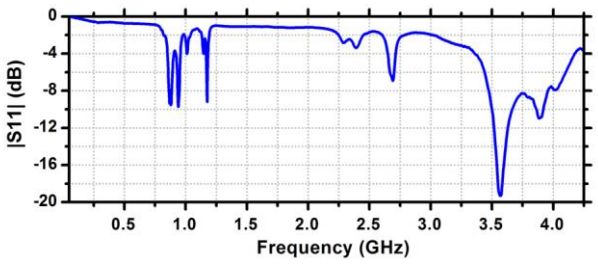

Figure 6.20. Magnitude of the input reflection coefficient ($|S_{11}|$) for the spiral resonator loaded patch antenna.

Chapter 7

Metamaterial Based Absorbers

7.1. Introduction

An electromagnetic absorber neither reflects nor transmits the incident radiation. Therefore, the power of the impinging wave is mostly absorbed in the absorber materials. The performance of an absorber depends on its thickness and morphology, and also the materials used to fabricate it. The simples absorber layout is referred to as the Salisbury screen [111]. It consists of a 377 Ohm resistive sheet placed a quarter wavelength ($\lambda_0/4$) apart from a metal plate at the center operation frequency (f_0). Salisbury proved that at integer multiples of $\lambda_0/4$, there is a reflection dip, implying resonant absorption. Though the frequency bandwidth of the absorber is inherently limited by its resonant electromagnetic behavior, resonant absorbers find several applications in microwave technology, especially in the reduction of resonant peaks of the radar signature of metallic objects and sharp shapes.

Recent advances in artificial electromagnetic materials have made it possible to control the electromagnetic field by means of properly engineered permittivity and permeability functions [1, 3, 7, 9, 10, 20, 21, 23, 24, 28, 32, 44, 59, 64, 67, 72-74, 96, 110, 112-117]. Metamaterial concepts, such as magnetic resonance and negative refraction, have led researchers to come up with new types of antennas [7, 9, 10, 98, 99, 101, 109, 118], lenses [44, 64, 113, 119], and absorbers [120-123].

The first metamaterial based absorbers have been proposed by Bilotti *et al.* and Mosallaei & Sarabandi and they are both characterized by an ultra-thin absorber thickness and a narrow operation band [121, 122, 124]. Later, Padilla's group demonstrated the perfect metamaterial absorber by utilizing the high imaginary part of the metamaterial index of refraction [123]. In other words, they utilized the lossy nature of metamaterials and achieved a thin absorber with a $\lambda/2.2$ unit cell dimension. The maximum measured absorption peak was 88% at 11.5 GHz with a 460 MHz bandwidth (Δf). The fractional bandwidth ($\Delta f / f_0$) was FBW = 4%, and the metamaterial unit cell was composed of two patterned metallic surfaces separated by a dielectric board: an electric ring resonator on the front and a line strip at the back. One advantage of metamaterial based absorbers is that the operation frequency can be controlled by scaling the constituting unit cells. These techniques that were developed mainly at the microwave frequencies can be applied at higher frequencies until the unit cell dimension and metal skin depth become comparable [41].

In the present chapter, we experimentally verify two metamaterial based configurations made of a planar arrangement of sub-wavelength inclusions combined with either a metal plate or a resistive sheet. The structure of the chapter is as follows. In Section 7.2, we present the geometry of the proposed designs. In Section 7.3, we describe the experiment setup. In Section 7.4, we present the results of the experimental characterization of the two types of absorbers in terms of resonance mechanism, electrical thickness and inclusion type.

7.2. Design and Geometry of Metamaterial Based Absorbers

The metamaterial based miniaturized absorbers, which we present in this chapter, consist of a back plate made of either metal or a magnetic metamaterial

and a front layer made of either a magnetic metamaterial or a resistive sheet, respectively. The sketches of the proposed absorbers are reported in Figure 7.1. The metal plate and the resistive sheet thicknesses are $d = 0.5$ *mm* and $d = 1.8$ *mm*, respectively. The magnetic metamaterial layer consists of a two-dimensional array of magnetic inclusions, namely split-ring resonators (SRR) or multiple split-ring resonators (MSRR), having a side length of $l = 3.2$ *mm*. The parameters of the SRR/MSRR are as follows: strip width $w = 0.1$ *mm*, separation between the strips $s = 0.1$ *mm*, split (gap) width $g = 0.1$ *mm*, number of rings $N = 2$ and $N = 8$ for the SRR and MSRR, respectively. The substrate on which resonators are etched is FR-4 with thickness $t = 1$ *mm* and a listed relative dielectric constant of $\varepsilon_r = 4.9\ (1+ i\ 0.02)$. The thickness of the copper strips in the FR-4 board is $h = 18\ \mu m$. In Figure 7.1, we show the right view of the absorber configurations and the SRR/MSRR geometry in the inset. The periods in the *x*- and *y*- directions are $p_x = 1.8$ *mm* and $p_y = 3.2$ *mm*, respectively. The separation between the back plate and magnetic the metamaterial medium is indicated as d_s. In the experiments, we used *82* layers in the *x*- direction and *38* unit cells in the *y*- direction, leading to a total transverse dimension of *148 mm x 140 mm*.

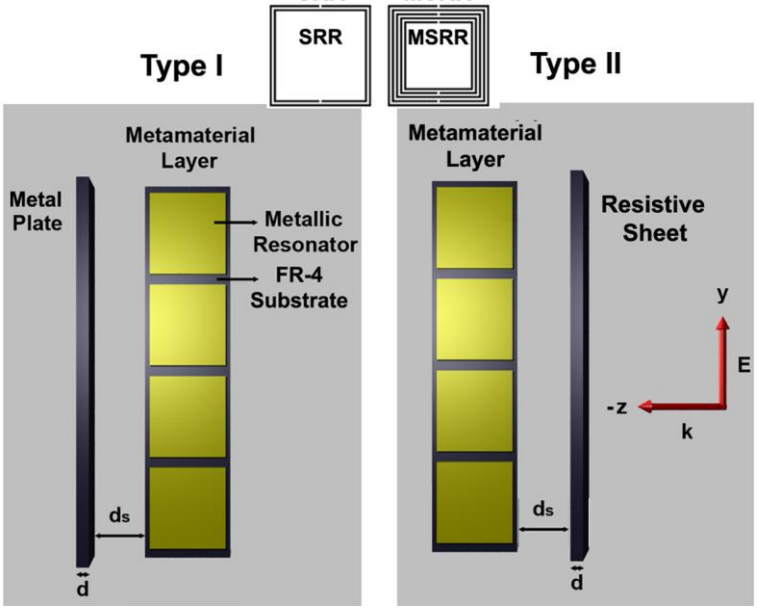

Figure 7.1. Geometry and schematic of the two absorber designs. Type I absorber consists of an array of magnetic resonators placed in front of a thin aluminum plate. Type II absorber consists of a carbon resistive sheet backed by the same metamaterial layer as for Type I. The wavevector (**k**) of the incident field is in the - *z*- direction and the electric field (**E**) is in the *y*- direction. As metallic resonators we used SRR and MSRR.

7.3. Transmission Reflection Setup at Microwave Frequencies

We developed a homemade free space measurement system that is composed of standard horn antennas, microwave lenses, and a network analyzer operating at around the 3.5 – 7 GHz band. All of the elements of the setup were connected by using specifically manufactured aluminum holders, which have been aligned by means of mercury steel bars passing through the corners of the sample holders.

The setup configuration is reported in Figure 7.2. The direction of gravity is from right to left, which made the placement of the samples under test easier. We use two hemispherical Teflon (the dielectric constant is 2) lenses in front of each of the two 10 dB gain standard horn antennas. The lenses have been

manufactured through the wide spread turning machines and their diameter is 20 cm. We verified the focus distance of the two lenses by direct scanning measurements and compared these data with the simulations. The focus was $f \sim 8\ cm$ away from the lens and the lateral full width at half maximum of the beam was *6 cm* at around *5 GHz*. The simulated magnitude of the electric field at *5 GHz*, when the reference plane for the sample is left empty is shown in Figure 7.2. The simulations have been performed through CST Microwave Studio.

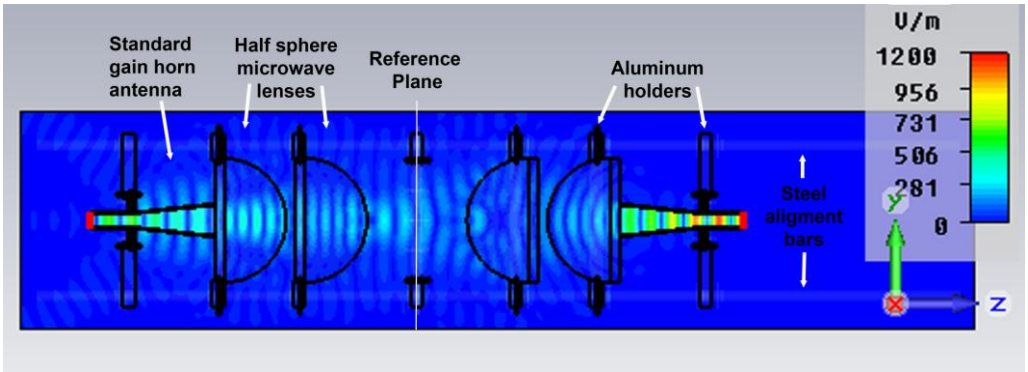

Figure 7.2. Experimental setup and simulated electric field magnitude distribution at *5 GHz*. The setup was placed as the steel bars touch the ground and the propagation direction was parallel to the gravitational acceleration. In the simulation the field was propagating in the –*z*- direction.

The two horn antennas were connected to a two-port HP8510C vector network analyzer. In a two-port network, the scattering parameters have been measured with a device imbedded between a 50 Ω load and the source. For a complete characterization of a planar sample, we measured the four complex scattering parameters of the two ports: i) input reflection coefficients with the output port terminated by a matched load (S_{11} and S_{22}) ii) forward transmission (insertion) gain with the output port terminated in a matched load (S_{21}, S_{12}). Before starting the characterization measurements, we performed a TRL calibration.

For the calibration, we used the same method described by Varadan *et al.* in 1989 [125]. The internal through-reflect-line (TRL) calibration model of the HP

8510C was performed. Firstly, we moved the second antenna and its lenses to a distance of $2f+\lambda/4$ from the first one, where λ is the wavelength at the mid-band (*5 GHz*) and *f* is the focal distance. We measured the *line standard*. Secondly, we moved the second antenna and its two lenses to a position such that the distance between the two lenses was two times the focal length (*2f*). Then we measured the *through standard*. Finally, we placed an aluminum plate at the reference plane that was a focal length away from both lenses, and measured the *reflect standard*. Now that our free-space calibration was ready, we moved on to the test measurements.

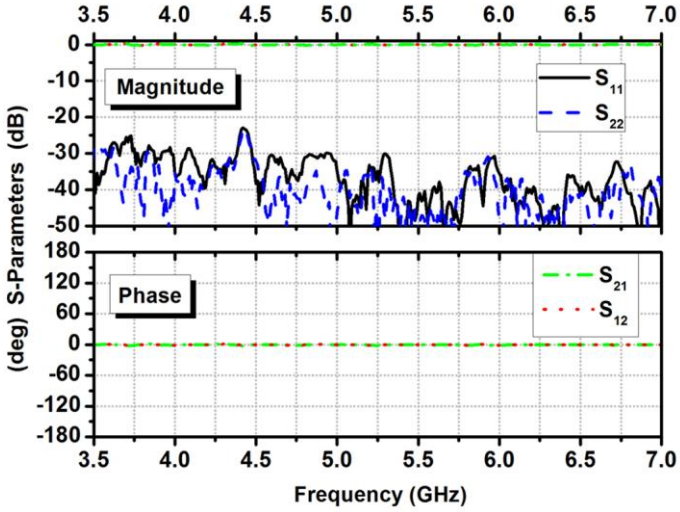

Figure 7.3. Measured scattering (S) parameters of the free-space after thru-reflect-line (TRL) calibration.

In Figure 7.3 we show the free-space measurement results in terms of both the transmission magnitude/phase and the reflection magnitude for the two ports obtained without any sample at the reference plane. S_{11} and S_{22} magnitudes are on the order of *–30 dB*, and the amplitude and phase of S_{21} and S_{12} are within ± *0.3 dB* and ± 3^o, respectively. We finalized the development of an experimentally confirmed homemade complex transmission-reflection setup by implementing a computer control code that measures and records the eight parameters sequentially.

7.4. Characterization of the Absorbers

7.4.1. Type I absorber based on SRR

In this case, we have the 2D SRR array placed in front of an aluminum back plate. In Figure 7.4 we show the magnitude of the measured S-parameters. The separation between the back plate and the SRR layer was $d_s = 7.2\ mm$. At around the magnetic resonance frequency of the SRR, we find the expected reflection dip: *–12.8 dB* at *4.74 GHz*. As expected, the structure behaves as a resonant absorber. When the electromagnetic field impinges on the structure from port 1, the absorbance of the structure is calculated by the formula: $A = 1 - |S_{11}|^2 - |S_{21}|^2$. Our absorption peak at *4.74 GHz* was *94.7%* and the 3-dB bandwidth is $\Delta f = 370\ MHz$. The fractional bandwidth of the device is, thus $\Delta f/f_0 = 8\%$. The total thickness of the absorber is $\tau = d + ds + p = 11.1\ mm$, which corresponds to $\lambda/5.7$ at the central frequency of operation.

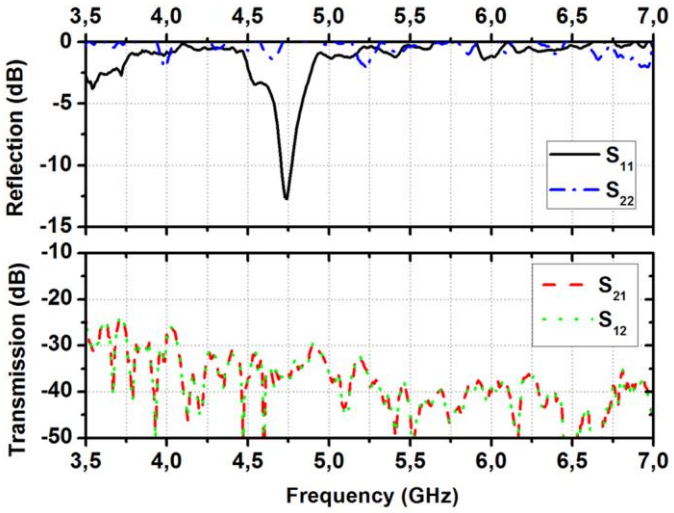

Figure 7.4. Scattering parameter amplitude for the Type I absorber.

In order to prove the magnetic origin of the resonant absorption, we applied a typical test for the analysis of the magnetic resonance in metamaterial structures [3, 44, 73, 74, 113]. According to this technique, we closed the split of the SRR, considering the structure reported in the inset of Figure 7.5 and referred to as a closed split ring resonator (CRR). The electrical resonance response of the SRR does not change when we short the splits.

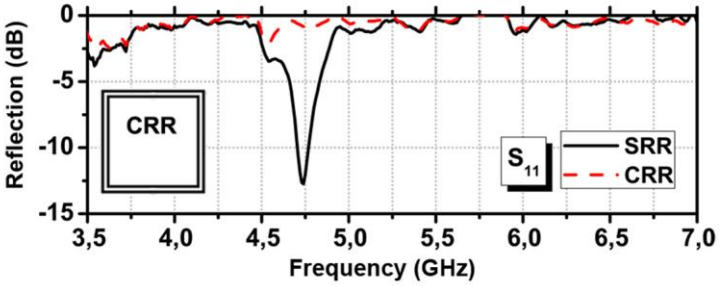

Figure 7.5. Comparison of the reflection responses (amplitude of S_{11}) of the two absorbers made of SRR and CRR.

However, the only source of magnetic resonance of the SRR is the circulating currents that are driven by the split capacitance. As we short the split capacitance, the driven force of the circulating currents is eliminated and as a result, we expect to lose the absorbing peak at around the magnetic resonance frequency. We constructed a layer of a two-dimensional CRR medium and measured its response in the absorber configuration. The results are reported in Figure 7.5. The absence of the reflection minimum proves that the origin of the SRR based absorber was indeed the magnetic resonance of the SRR themselves.

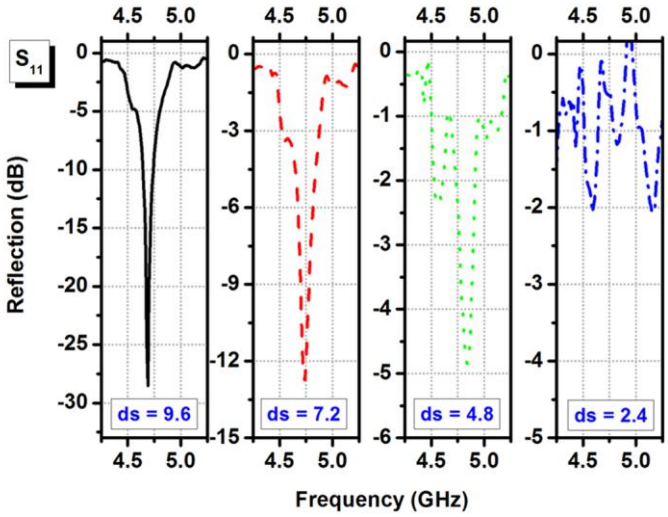

Figure 7.6. Dependence of the reflection minima on the separation between the metal plate and the metamaterial layer.

While investigating the absorber performance, we show that the reflection minimum depends on the distance between the metamaterial layer and back plate. In Figure 7.6, we compare the absorber performance for different d_s values, ranging from *2.4 mm* to *9.6 mm*. We observe that the electrical length of the separation between the metamaterial layer and the metal plate should be on the order of $\lambda/8$ for high resonance strength. The absorbance increases for d_s = *9.6 mm* and decreases when it is *4.8 mm* or *2.4 mm*. At d_s = *9.6 mm*, the absorption peak is *99.8%* at *4.69 GHz* with $\tau = \lambda/4.7$ and *FBW = 8%*. As d_s further decreases, the response dies out. It might be possible that we are able to further reduce the absorber electrical thickness by using more miniaturized resonators, according to the methods that were developed in our recent papers [32, 33, 59].

7.4.2. Type I absorber based on MSRR

In this part of the study, we show that by reducing the electrical size of the resonator, it is, indeed, possible to reduce the electrical thickness of the absorber. For the concept demonstration, we replaced the SRR medium with an

MSRR one. The structural parameters of the MSRR are the same as the SRR, but now the number of the rings is $N = 8$ instead of $N = 2$. This enabled us to obtain a smaller electrical size for the same space occupancy. Figure 7.7 shows that the reflection minimum shifts to lower frequencies in accordance with the resonator electrical size. In this configuration, the separation between the metamaterial layer and the metal plate is $d_s = 7.2\ mm$. The absorption peak is *82 %* with *FBW=6%* and an electrical size of $\lambda/6.2$ at *4.33 GHz*. A further reduction of the absorber electrical dimensions can be easily obtained by using more miniaturized inclusions, such as the spiral resonators [32, 33, 38, 59].

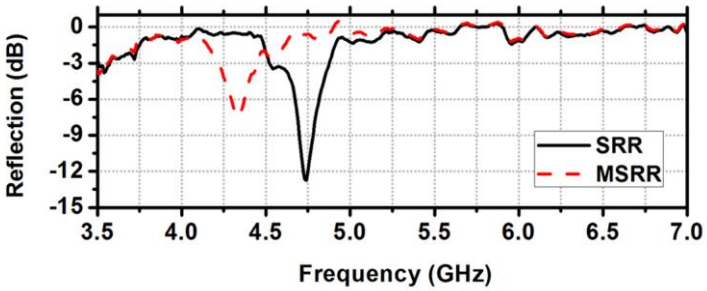

Figure 7.7. Effect of the resonator electrical size on the absorber thickness.

In all the measurements presented so far, we have characterized the absorber for normal incidence only. Recently, we demonstrated that the response of SRR based metamaterials remains nearly the same up to 45^o incidence angle [80]. Moreover, the metamaterial particles studied here can be packed into a 2D isotropic unit cell such that a polarization independent response can be obtained [2, 32].

7.4.3. Type II absorber based on SRR and MSRR

In this part of the study, we replaced the metal plate with a carbon based resistive sheet having a sheet resistance of *5 kOhm*. In this configuration, the metamaterial layer is the back plate and the resistive sheet is the front layer. It is worth noticing that, in contrast to the Type I absorber design, in this case we do

not use any metal screen. This kind of absorber is very useful when we would like to suppress a resonant peak of the radar signature of a non-metallic object, made, for instance, of new ultra-light materials based on carbon fibers. The absence of the metal backing, in this case, is crucial because if we used a metal backed absorber, we would reduce the resonant peaks of the radar response at other frequencies. As presented in Ref. [126], in fact, the metal backing makes the non-metallic object a metallic one. The transmission and reflection data for this case are shown in Figure 7.8. The configurations employing both the SRR and MSRR based media were measured. There is a *97.4%* absorption peak at *4.67 GHz* for the MSRR case and a *98.4%* absorption peak at *5.15 GHz* for the SRR case. The separation between the metamaterial layer and the resistive sheet determines the frequency of the reflection dip: $d_s \approx 7\ mm$ and $d_s \approx 10\ mm$ have been used for the SRR and MSRR cases, respectively. Thereby, the electrical thicknesses and -10 dB bandwidths (BW_{-10dB}) are $\lambda/4.7$, $\lambda/4.2$ and 9.9%, 9.6%, for the SRR and MSRR cases, respectively.

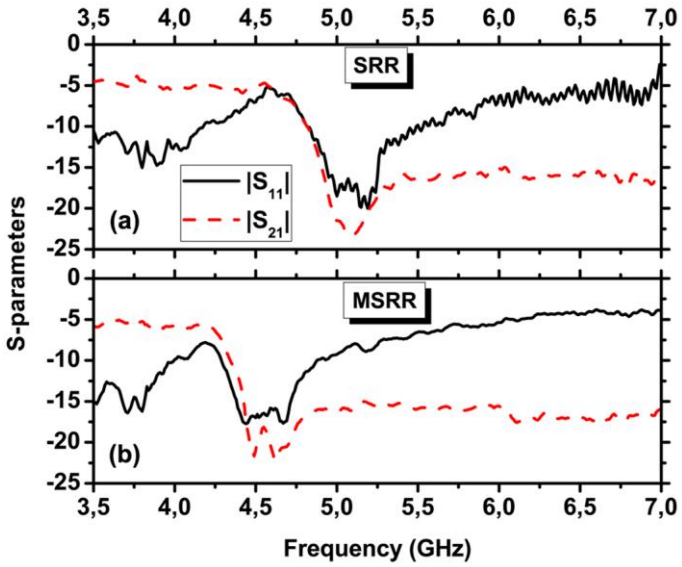

Figure 7.8. Scattering parameter amplitudes (dB) for the Type II absorber based on SRR and MSRR.

Chapter 8

Metamaterial Incorporated Photonic Devices

8.1. Introduction

Artificial structures that act like materials can show extraordinary properties that could result in a group of new devices and extensive control of electromagnetic waves [112]. These metamaterials' unit cell size determines their narrow operation frequency band, which could be in microwave, millimeter-wave, THz, mid-IR, IR or visible [2, 3, 24, 28, 32, 43, 67, 73, 113, 127]. The constituting elements' physical sizes were typically an order of magnitude smaller than the operation wavelength. When the operation frequency is at the optical regime, metamaterial properties such as negative refraction, the reversal of Cherenkov radiation, Doppler shift, cloaking and an enhanced magnetic response could lead to high performance and novel photonic devices in information and communication technologies. These include negative index material based superlenses, optical isolators, electro-optic modulators, and optical switches. In the present chapter, we investigate a basic analysis of photonic metamaterials, especially focusing on their magnetic response [44].

Bethe studied transmission through a subwavelength aperture and diffraction of light passing through an aperture of size much smaller than the incident wavelength in the 1940s. The transmission efficiency that is normalized to the aperture area depends on the aperture size in terms of the wavelength of the incident electromagnetic wave [128]. Ebbesen et al. invented the surface plasmon aided enhanced transmission structure. They properly designed the

geometry of the metal around the subwavelength hole and thereby excited the surface plasmon resonances boosting the enhanced transmission efficiency [129]. The results are useful in the fields of scanning nano-lithography, optical data storage, near-field optical microscopy, and bio-chemical sensing, as they yield a light spot beyond the diffraction limit with an enhanced transmission [129, 130]. In the present chapter, we exhibit an exciting design that incorporates deep subwavelength optical split ring resonators to enhance transmitted power radiated to the far field passing through a subwavelength hole.

8.1.1. Design Simulations

We started our analysis with numerical simulations of the magnetic metamaterial unit cells. The commercial software CST-Microwave Studio [37] helped us to see the response of the photonic metamaterial designs. We used the program's frequency domain solver with unit cell boundary conditions. Metamaterials composed of shaped metallic resonators placed on a substrate. Their actual parameters such as metal loss, coated metal thickness, resonator side length, strip width, and arm length of these structures should be identified by the help of experimental data. We used the data given in the literature for the metal characteristics and performed the design simulations. As the next step, we tried to fabricate the arrays of the resonators, and we paid specific attention to achieve the structure parameters as designed.

8.2. Nanofabrication of Optical Metamaterials

Firstly, we prepared the sapphire substrate on which the metallic resonators would be printed. It was diced to 7mm x 7mm dimensions, cleaned in acetone, isopropanol, deionized water consecutively, and dried by using a nitrogen gas gun. The sample was dehydrated on a hot-plate at 180 °C for 1 minute and coated

with polymethyl methacrylate (PMMA-950K-A2) high resolution positive resist via a spinner machine to achieve a 150nm thickness. We baked it at 180 C° for 90 seconds, spincoated with aquasave, and rebaked at 90 C° for 30 seconds to prevent charging during e-beam exposure. The e-beam exposure step starts with the design of the exposure structures and dose tests. In the Raith e-beam lithography computer aided controller program, we drew the U-shaped resonators as a composition of single pixel lines. For the dose tests, a two-dimensional array of split ring resonator (SRR) arrays with slightly varying parameters was organized. A dose test exposure was performed at 15 kV acceleration voltage, and the sample was inserted into a developer solution of 1:3 ratio MIBK: H_2O and kept there for 45 seconds. The next step was metallization, and the sample was coated with silver (Ag) via an e-beam evaporator machine. The final steps were the lift-off and scanning electron microscopy (SEM) inspection. We determined the optimum dose for the designed dimensions. By using these optimum dose test results, we fabricated the SRR array coated sample, as shown in Figure 8.1(b).

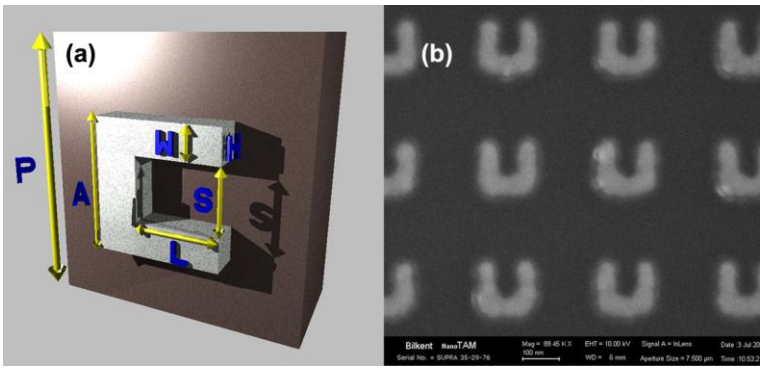

Figure 8.1. (a) Schematic and parameters of the unit cell. (b) Scanning electron microscopy image of the fabricated array.

8.3. Transmission-Reflection Setup for Optical Regime and Characterization Measurements

Before concentrating on the obtained results, we would like to discuss a few points. For the e-beam lithography fabrication technique, the resonator parameters can be different from the designed ones on the order of 5 nm. In addition to this, the measured structure parameters can be a few nm different from the real ones due to the SEM image precision limit. We observed that for each of the printed SRR we had a different set of parameters in our array. The parameters varied at most 5 nm from one SRR to another at different regions of the array. Therefore, in our simulations we had to find out a set of average SRR parameters that gave the same response as the experimentally characterized one. The unit cell of the average SRR whose transmission response is close to the measured SRR array is shown in Figure 8.1(a). In Figure 8.2, we can compare the simulation and experiment results for the configuration that is to be studied in detail in the following section. The periods in the x and y directions were p_x = p_y = 330nm, side length of the SRR at the x and y directions were a_x = a_y = 155nm, arm length was L = 104nm, width of the arms was w = 39nm, separation between the arms was s = 77nm and the coated metal thickness was h = 39.5nm. We took the substrate thickness in the simulations as t = 150nm while it was 1mm in the experiments. In the simulation domain, we observed that using a substrate thickness larger than 150nm does not change the resonance frequency of the SRR array. Thereby, in all of our simulations, we used 150nm thick substrate instead of a 1mm one. At the optical regime, the dispersion characteristics of metals play an important role. They were taken into account by fitting the complex metal permittivity values given in Palik [131] by using the Drude model. CST Drude model permittivity was given by the formula: $\varepsilon(\omega) = \varepsilon_\infty + \omega_p^{\,2} / \omega(\omega - i\upsilon_c)$ where ω_p was the plasma frequency and v_c was the collision frequency. Our fit to the Palik data implied ω_p = 13250x10^{12} rad/s and v_c = 130 THz. We used this data set to model the dispersion properties of silver in our simulations. However, we discovered from the experimental data that the

collision frequency of our metal was 4.3 times larger. Despite this, we used the values of ω_p and v_c obtained from the fit of Palik data in the following theoretical analysis.

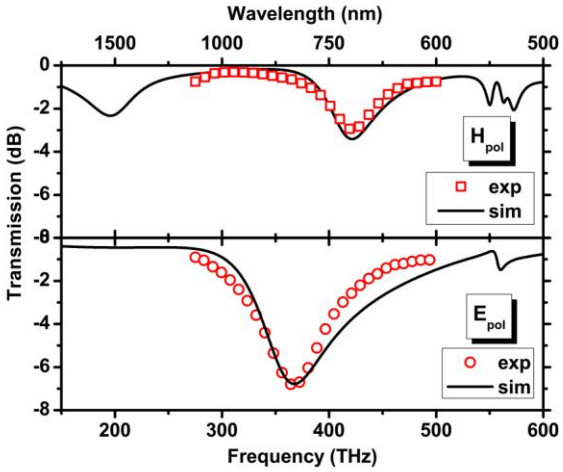

Figure 8.2. Simulated and measured transmission response of the sample SRR array.

8.4. Properties of Photonic Magnetic Metamaterials

8.4.1. Polarization dependent transmission response

The significance of SRR relies on its magnetic resonance. Depending on the orientation of the SRR and polarization of the incident light we could excite the magnetic resonance of the SRR by E-field, B-field, or both E and B-field of the incident light. It is also possible that the SRR may not be excited at all. In Figures. 9.3 and 9.4, we show the possible orientations and corresponding transmission response of the SRRs. For the planar case, as shown in Figure 8.3 as the (blue) dotted curve, we observed two transmission stop bands. The first one appeared due to the magnetic resonance, and the second one appeared due to the electrical resonance of the SRR. At the magnetic resonance, we had circulating currents at the SRRs, so that they acted like magnetic dipoles. This stop band was at around 1550nm wavelength. The SRRs physical size was an

order of magnitude smaller than this operation wavelength. At the electrical resonance mode, we observed an electric dipole like response and the stop band was around 700 nm wavelength. For the other orientation shown in Figure 8.3(b), we could only obtain the electrical resonance since the magnetic resonance of the structure was not excited. We saw a stop band at around 830nm that was slightly different from case (a). We have not yet obtained a coupling effect between the two modes (magnetic and electric) as in case (a). By this analysis, we can characterize our SRRs and determine the operation frequency that corresponds to the magnetic resonance frequency. In Figure 8.4, we show the other possible orientations of the SRRs with respect to the incident field. The magnetic resonance frequency for this case was around 1200nm and the electrical resonance was at 770nm. In case (a), the magnetic resonance was excited by the B-field of the incident wave and in case (b) none of the resonances were excited.

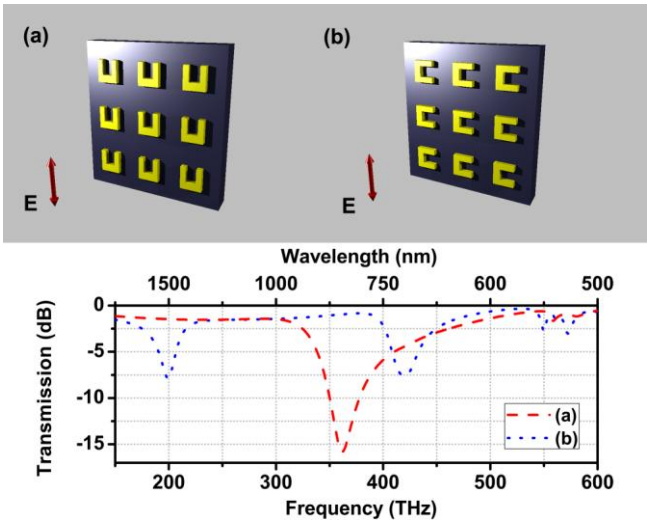

Figure 8.3. Different orientations and transmission response of the SRR medium (a) Only the electric resonance was excited, (b) Both electric and magnetic resonances were excited.

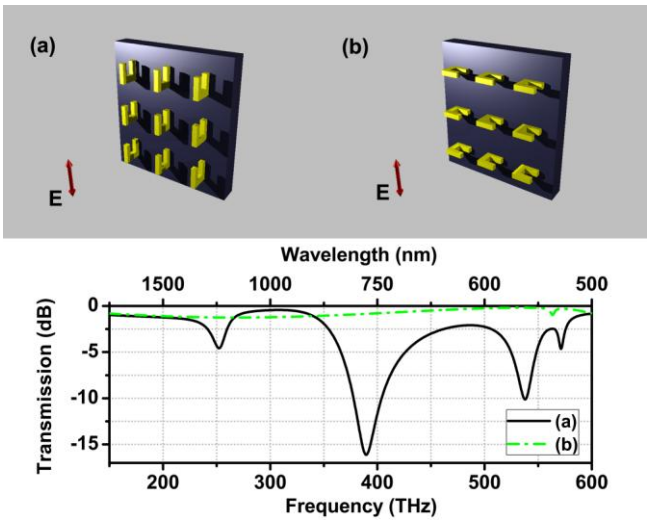

Figure 8.4. Other possible orientations and transmission response of the SRR medium: (a) Both electric and magnetic resonances were excited by the B-field of the incident wave, (b) None of the resonances were excited.

8.4.2. Tunability via a buffer layer

Based on the simulation results we developed a method for the fine tuning of the magnetic and electric resonances of SRR arrays. When the substrate itself was very thin, or coated with a very thin buffer layer, the magnetic resonance frequency shifts, depending on the layer thickness. In Figure 8.5, we presented the results for the glass layer of thicknesses varying from 10 to 30 nm. As this buffer layer thickens, the resonance frequency shifts from 185.1 THz to 173.8 THz. As we continue to increase the buffer layer (t_b) or substrate thickness (t), the shift shows a saturating behavior and does not change at around 150nm thickness. By using materials whose volume is dependent on the applied temperature, pressure, or static field, we can slightly tune the metamaterial resonance frequency.

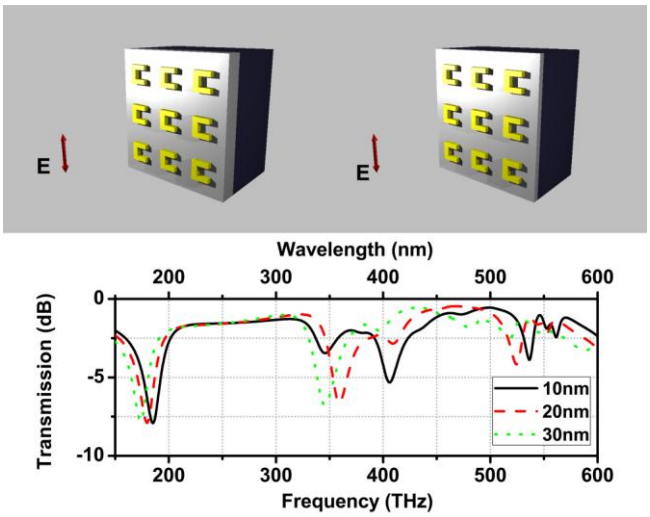

Figure 8.5. Effect of changing buffer layer thickness on the magnetic resonance frequency.

We tried to explain some of the effects observed here by using the theory of perturbations [132]. For small buffer layer thickness (t_b), or small substrate thickness (t) without buffer a layer, the shift of the resonance frequency can be qualitatively explained by considering the effect of substrate as a perturbation of the resonance field of the substrate-free SRR. Indeed, it is well known from the theory of perturbations of the closed cavities with a perfect electric conductor (PEC) wall that introducing a dielectric perturbation into such a cavity leads to a downshift of the eigenfrequencies. In this case, the perturbation affects the electric field. Indeed, in the general case only the frequency shift can be estimated as $\Delta f / f = -(\varepsilon - \varepsilon_0)F/\varpi - (\mu - \mu_0)G/\varpi$, where ε_0 and μ_0 are free-space permittivity and permeability, ε and μ are permittivity and permeability of the perturbation, f is an eigenfrequency of the unperturbed cavity and ϖ is the corresponding eigenmode energy; *F* and *G* are the variations of the energy of the electric and magnetic fields arising due to the introduced perturbation. Thus the second term is vanishing if $\mu = \mu_0$. Analogously, placing a dielectric substrate below a SRR in turn results in the enhancement of the resonance electric field, which in turn increases the effective capacitance and, hence, decreases the magnetic resonance frequency (f_m). Furthermore, using this

analogy one could expect that placing a diamagnetic ($\mu<\mu_0$) or low-permittivity ($\varepsilon<\varepsilon_0$) substrate instead of a dielectric one should result in the upshifting of f_m. Further increase of the substrate thickness leads to the saturation of f_m . In other words, it does not lead to any significant variation in f_m starting from a certain value of t_b of t. This is quite predictable since only the near-interface part of the substrate perturbatively affects the resonance field of the substrate-free SRR. Our perturbation theory based interpretation is in agreement with the results presented in a Wegener Group paper, see Figure 3 in ref. [133]. Therein, the increase of the index of refraction of the dielectric substrate material, *n*, results in the downshifting of f_m. For larger *n* values, we obtain a stronger perturbation of the resonance electric field.

8.4.3.Density of split ring resonators

In Figure 8.6, we demonstrated the effect of the SRR period on the resonant behavior. We present the cases when the period was 1.4, 2, 4, and 6 times the side length of the SRR. As the period was increased, we observed two significant features. First, due to the weakened coupling of the SRRs, the fractional bandwidth of the stop band decreased. Moreover, the resonance strength reduced while the resonance frequency decreased. The second outcome was that the response of the SRR array nearly became the same as the single SRR as the period increased up to 6a. Therefore, in our future studies in order to observe the single resonator effects, we could also use periodic SRRs with a sufficiently large period.

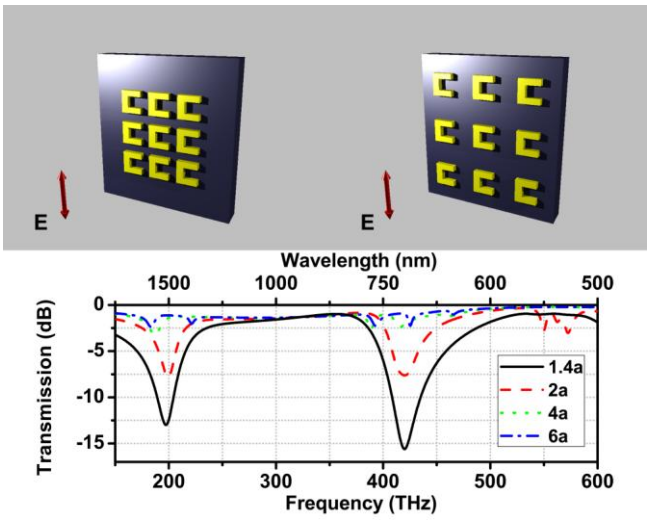

Figure 8.6. Effect of SRR period.

8.4.4. Shift of magnetic resonance frequency

One of the most important parameters of photonic SRRs that determines the magnetic resonance frequency was the arm length L. In Figure 8.7, we decreased the arm length from 104nm to 0nm and observed a quite strong shift of magnetic resonance frequency. The electrical resonance remained nearly the same while the magnetic resonance shifts from 199.5 THz to 324.6 THz when the arm length reduced from 104nm to 35nm. The limiting case, L = 0, corresponds in fact to the square particles. In this case, the magnetic resonance approached its limit and we only had the electrical resonance present. In this part, we observed that the reduction of the arm length increases the operation frequency, but the electrical size of the SRRs also reduced and they were not in the deep subwavelength regime any more. Therefore, the array moved from the metamaterial regime to the photonic crystal regime.

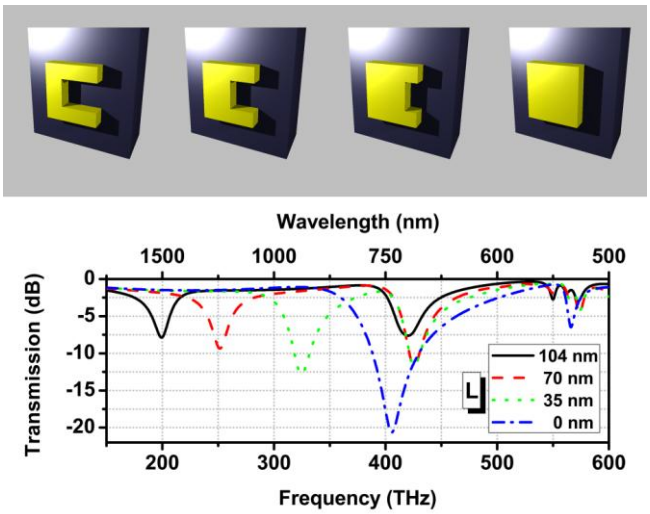

Figure 8.7. Effect of changing the arm length L.

The analogy with the perturbed PEC-wall cavities can again be adopted, since ω_p is still several times larger than $2\pi f_m$. Accordingly, the variation of the SRR shape from L = 104nm to L = 0nm can be qualitatively interpreted as a perturbation due to the introduction of a PEC body into the cavity. In this case, the frequency shift is $\Delta f / f = -\varepsilon_0 F / \varpi + \mu_0 G / \varpi$ [132]. Hence, such a perturbation should lead to the upshift of the resonance frequency, if the effect of the magnetic field dominates over that of the electric field. According to recent studies by the Soukoulis Group [41, 96], the magnetic resonance frequency can be extracted from a quasi-static LC-circuit theory in the following form: $f_m = \frac{1}{2\pi} \frac{1}{\sqrt{(L_e + L_m)C}}$, where L_e is the electron self-inductance related to the kinetic energy, L_m is the magnetic field inductance, and C is capacitance of the split ring. In turn, both L_e and L_m are proportional to the length of the axis of the wire making the ring, l'. The structures shown in Figure 8.7 l'decreased from left to right leading to larger f_m. Hence, the results of the qualitative analysis based on both perturbation and LC-circuit interpretations are in agreement.

8.4.5.Metal properties and resonance properties

As the operation frequency of the metamaterials increase, the effect of plasma frequency of the metal can't be neglected. A metal with either a larger or smaller plasma frequency (ω_p) than that of silver (Ag) enables one to obtain larger or smaller values of f_m compared to silver. In the above formula for f_m [41], ω_p appears due to the term $L_e \propto \omega_p^{-2}$. In the hypothetic limiting case, $L_m = 0$, $f_m \propto \omega_p$ and the contribution of L_e vanishes if ω_p tends to infinity. Silver (Ag) is one of the low loss metals that has also been demonstrated to be less lossy than gold (Au) and antimony (Pb) [134]. The high frequency response of SRR can be achieved by modifying the SRR shape. We can obtain a magnetic resonance at higher frequencies with the same SRR side length, but by varying the arm length as shown in the previous part. However, we should keep in mind that high frequency operation is then achieved at the expense of electrical size. Another suggestion was to use metals at low temperatures to be able to push the resonant behavior at higher frequencies while keeping the electrical size the same [72]. In Figure 8.8, we show how our resonator would behave if we had the opportunity to fabricate it from a perfect electrical conductor. The stop band of the magnetic resonance moved from 199.5 THz to 338.1 THz, and the resonance strength changed from -8 to -28 dB while replacing the PEC SRRs with the silver ones. However, even with the PEC SRR, the metamaterial operation cannot cover the entire visible spectrum due to the fundamental limitations of the used SRR designs.

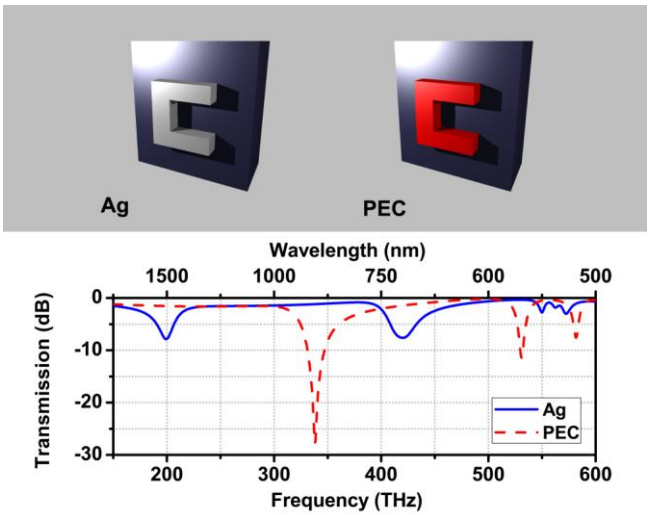

Figure 8.8. Effect of the metal loss and plasma frequency of the SRR material.

8.5. Enhanced Transmission at the Far Field

The light passing through subwavelength apertures exponentially decays and the transmission values are typically very low. Our recent proposal to enhance the transmission is shown in Figure 8.9. In case (a), we have a subwavelength hole that is 200 nm wide and 300 nm deep. The transmission was very low, as shown in the solid curve in Figure 8.9, until the wavelength of the incident light reached a value comparable to the aperture width. Here, we introduced a novel technique to enhance the transmission passing through a single hole in a rather thick plate. As shown in Figure 8.9(b), we introduced three SRRs throughout the hole for the orientation, in which the B-field of the incident wave excited the magnetic resonance of the SRRs. In this case, we observed a 400-fold enhancement of transmission at 300THz ($\lambda \approx 1000$nm). In the suggested configuration, the first SRR behaves like an electrically small receiver antenna [9, 10], the second SRR enables the light propagation throughout the waveguide [135], and the third SRR reemits the light as a transmitter antenna. This enhancement is achieved in the subwavelength regime and appears at the far field. To compare, we also simulated the Ebbesen structure, for which the single

hole was surrounded by periodic surface corrugations [129]. We saw that the magnitude of the power transmission level was within the same range in terms of order of magnitude. The enhancement for that case was approximately 13 fold, while the operation wavelength was around 700nm. Moreover, there were 5 grooves with electrical size almost equal to operation wavelength (λ), thereby the effective radiating aperture area of the Ebbesen structure was 9λ x 9λ. There are two major advantages of our structure: i) The beam can be transferred to far field with an order of magnitude larger enhancement (~400-fold), ii) Our radiating aperture area was subwavelength λ/5 x λ/5 and approximately 2000 times smaller than the Ebbesen case. Therefore, in terms of transmission enhancement per radiating aperture area our structure is quite impressive. On the other hand, the disadvantages of this design are the following i) It is very difficult to operate at the visible or UV regimes due to the saturating response [41], ii) The fabrication via current e-beam lithography, FIB milling, and multistep coating is quite difficult and expensive. We are currently working on much simpler designs that utilize the same mechanism for experimental demonstration at the expense of lower enhancement.

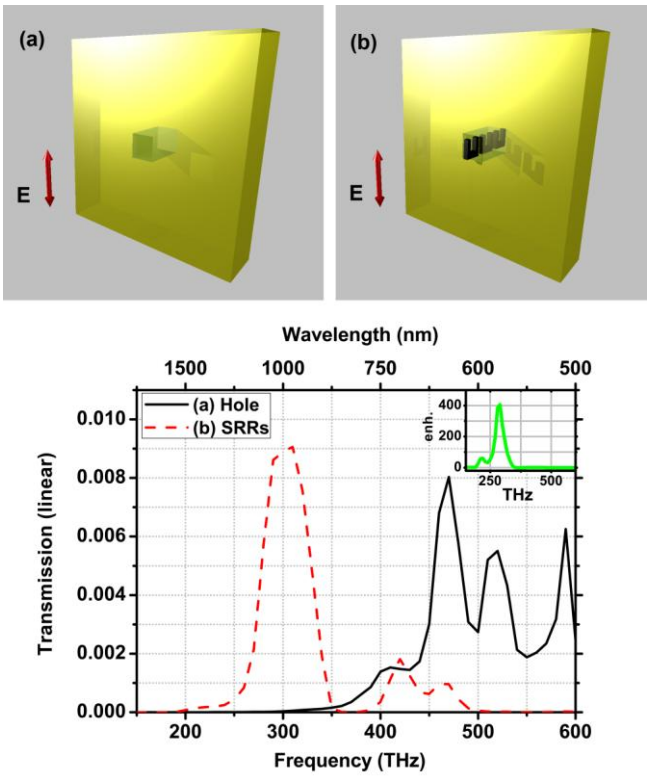

Figure 8.9. Configuration and results for the transmission enhancement design. (a) Metal plate with 300nm thickness with a square hole with 200 nm side length at the centre. (b) The three SRRs were placed at the input and output apertures and inside the hole along the propagation direction. Transmission is normalized by the incident wave magnitude. The corresponding enhancement value was given in the inset.

In Figure 8.10, we demonstrate the far field response and near field beam profiles at the operation frequency. In our numerical study, we excited the structure under test via a waveguide and extracted the normal transmission response from far field monitors. In Figure 8.10, we show the power patterns at the x-z and y-z planes. The reflected power level is 20 dB higher than the transmitted one at the far field at a 300 THz operation frequency. The angular beam widths were 120° and 88° at the x-z and y-z planes, respectively. The beam was quite broad with 3.9 dBi directivity.

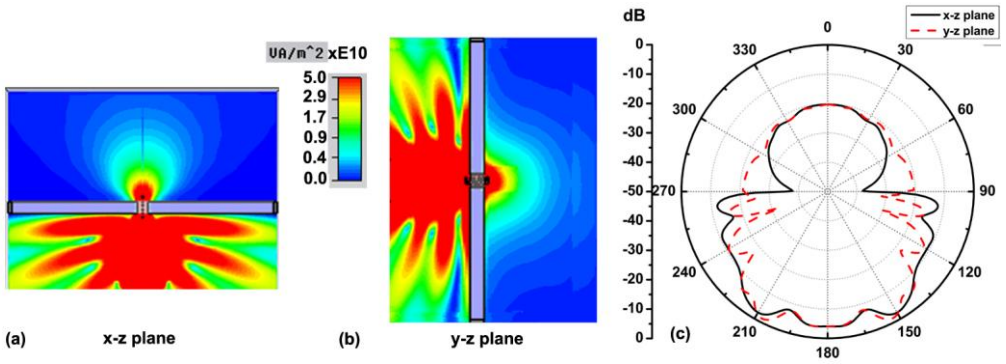

Figure 8.10. Field distribution at 300 THz. Near field power distributions around the structure in the basis planes (a) x-z plane, (b) y-z plane. (c) Far field patterns cuts at the two planes.

8.6. Photonic Metamaterial Based Absorbers solar, stealth, thermal isolation, infrared photo-detector and biosensor applications

In the present section, we studied a novel absorber that utilized metamaterial concepts and resonant absorption theory. The absorber is metal backed and involves a thin photonic magnetic metamaterial layer. The subwavelength unit cells of the metamaterial layer were designed to operate at the infrared regime to provide an experimental proof of concept. Then we improved the design and incorporated a very thin resistive sheet layer between the dielectric and metamaterial layers. This composite structure acts like a wideband antireflection coating. The structure of the section is as follows. In subsection 8.6.1, we present the geometry of the proposed design. In subsection 8.6.2, we describe the fabrication, experimental characterization and simulation methods. In subsection 8.6.3, we present the results of the experimental characterization and simulations of the absorber in terms of spectral response. In subsection 8.6.4, we extend the design to polarization independent case and present the field distribution and power flow. Finally in subsection 8.6.5, we demonstrate the oblique performance of the absorber.

8.6.1.Design and Geometry

The metamaterial based thin absorbers, which we present in this paper, consist of a metal back plate, a front magnetic metamaterial layer and a dielectric layer in between. The geometry and parameters of the proposed absorber are reported in Figure 8.10. The substrate, metal layer, dielectric layer, and metamaterial layer thicknesses are $t_s = 1\ mm$, $t_m = 300\ nm$, $t_d = 115\ nm$, $t_{Ti} = 20\ nm$ and $h = 50\ nm$, respectively. The magnetic metamaterial layer consists of a two-dimensional array of magnetic inclusions, namely split-ring resonators (SRR) is shown in the inset of Figure 8.11. The parameters of the SRR were as follows: the side length of the SRR at the *x* and *y* directions were $140.7\ nm < a = a_x = a_y < 174\ nm$, the periods in the *x* and *y* directions were $p_x = p_y = 330nm$, width of the arms was $37\ nm < w < 59.3\ nm$, separation between the arms was $s = a - 2w$, and arm length was $L = 104nm$. The substrate was sapphire, back metal was silver (Ag), the SRR's were composed of titanium (Ti) and gold (Au) and the dielectric was Si_3N_4 with dielectric constant, $\varepsilon = 4.51$. The dimension of the area on which the SRR's printed was $300\ \mu m \times 300\ \mu m$.

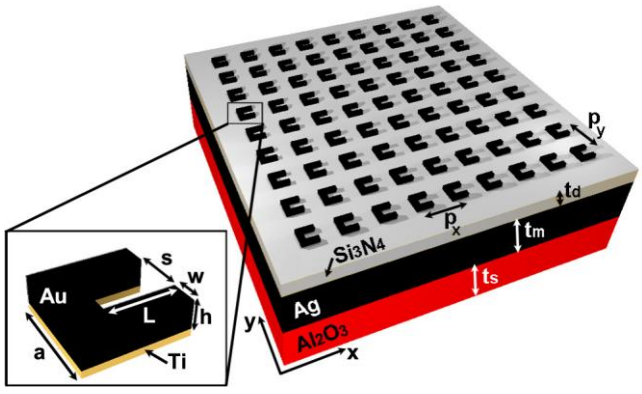

Figure 8.11. Geometry and schematic of the thin absorber design. The absorber consists of an array of magnetic resonators placed on the top of a thin dielectric. The wavevector (**k**) of the incident field is in the - *z*- direction and the electric field (**E**) is in the *y*- direction.

8.6.2. Methodology

In the following sub-sections, we explain our nano-fabrication techniques, experimental characterization setups, and numerical simulations.

8.6.2.1. Nano-Fabrication

Firstly, we prepared the sapphire substrate on which the metallic resonators would be printed. It was diced to 10 mm x 6 mm dimensions, cleaned in acetone, isopropanol, deionized water consecutively, and dried by using a nitrogen gas gun. Then, a patterned silver layer of 300 nm thickness was coated with electron beam evaporation method. We have patterned the Silver layer with photolithography: i) in order to overcome some deposition problems of silicon nitride over large areas of silver, ii) to obtain a better coating quality, iii) to obtain mirror regions for calibrating the reflection response. On top of Silver back metal layer, we have coated silicon nitride dielectric layer with 130 nm thickness by using a PECVD (Plasma Enhanced Chemical Vapor Deposition) machine. We have used silane and ammonia and argon gases for this process, their flow rates being 300 sccm, 10 sccm, and 50 sccm respectively. Applied RF power was 50 W and process pressure was 80 pA. For patterning the samples to obtain the metallic resonators, sample was coated with polymethyl methacrylate (PMMA-950K-A2) high resolution positive resist via a spinner machine to achieve a 120 nm thickness. We baked it at 180 C° for 90 seconds, spincoated with aquaSAVE (sulfonated polyaniline vanish for e-beam lithography), and rebaked at 90 C° for 30 seconds to prevent charging during e-beam exposure.
E-beam lithography was done by using Raith's eLiNE nanolithography system. This process starts with the design of the structures that are to be exposed and dose tests. In the Raith lithography software, we drew the U-shaped resonators as a composition of single pixel lines. For the dose tests, two-dimensional arrays of SRRs with slightly varying parameters were organized. A dose test exposure was performed at 7.5 kV acceleration voltage, and the sample was inserted into

a developer solution of 1:3 ratio MIBK:Isopropanol and kept there for 40 seconds. The next step was metallization, and the sample was coated with gold (Au) via an e-beam evaporator machine. To promote the adhesion to the silicon nitride surface, a 20 nm layer of Ti was deposited in this evaporation process before coating the Au layer. The final steps were the lift-off and scanning electron microscopy (SEM) inspection. We determined the optimum dose for the designed dimensions. By using these optimum dose test results, we fabricated the SRR array coated sample, as shown in Fig. 1 background.

8.6.2.2. Experiment

The free space measurements of the samples were performed by using a homemade transmission reflection setup. A schematic of the setup is given in Figure 8.12. The light was incident from an Ocean Optics LS-1 tungsten halogen light source and passes through a Glan Taylor cube polarizer, a beam splitter and focused on the two-dimensional SRR area via a Melles-Griot *20x* objective. The beam diameter was around *100 μm*. We collected the light with a *50x* objective and by the aid of a mirror we sent the beam to a ccd camera. We found the position of the absorber area by the aid of alignment marks on the sapphire sample and then centered the light beam on that area. After alignment we allowed the light to go to the lens and multimode fiber (fiber2). The signal was measured by using an Ocean Optics USB4000 spectrometer at the visible regime (*600 nm – 1000 nm*) and by using a StellarNet Red Wave NIR spectrometer at the infrared regime (*900 nm – 1700 nm*). We calibrated the sample's transmission response with respect to bare substrate. For the reflection measurements, we used the bare metal coated sample area for calibration. The beam reflected from the absorber area again passes through the *20x* objective and transmitted to a multimode fiber (fiber1) by the way of the beam splitter. The reflection amplitude was also measured by using the two spectrometers.

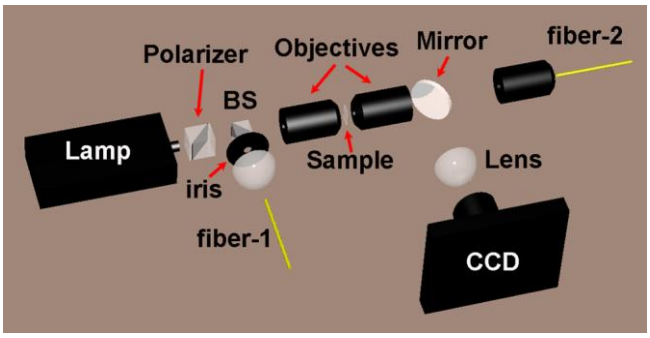

Figure 8.12. Homemade experimental setup for transmission and reflection based characterization. Fibers were connected to spectrometers. The mirror was removed after placing the beam onto the area of interest.

8.6.2.3. Numerical Simulations

We analyzed the magnetic metamaterial incorporated absorber unit cell by using the CST-Microwave Studio. The unit cell was assumed to be infinitely periodic at the lateral directions. Frequency domain solver of the program provides the necessary unit cell boundary conditions. We also investigated the magnetic metamaterial layer was composed of shaped metallic resonators placed on a bare substrate. We used experimental data to estimate the magnetic metamaterial layer's actual parameters such as metal loss, coated metal thickness, resonator side length, strip width, and arm length of these structures. We also utilized the literature data of silver, gold, titanium in order to model metal parameters. Moreover, detailed SEM inspections gave us the parametric variations of the realized samples.

8.6.3. Results and Discussions

For the e-beam lithography fabrication technique, the resonator parameters can be different from the designed ones on the order of 10 nm. We had to find a method that can take into account these fabrication imperfections in the simulations. We observed in SEM inspections that each individual SRR actually had different parameters from the others'. The parameters varied at most 5-10 nm from one SRR to another at different regions of the 2D array. We decided to

create 6x6 array of SRR unit cells in simulations whose parameters were varied in accordance with SEM data. We gave the dimension range of the SRRs. We took the substrate thickness in the simulations as $t_s = 150\ nm$ while it was *1 mm*. However, we confirmed numerically that using a substrate thickness larger than *150 nm* does not change the resonance frequency of the SRR layer. Thereby, in all of our simulations, we used $t_s = 150\ nm$ instead of *1 mm*. The dispersion characteristics of metals are of critical importance at the optical regime. The complex metal permittivity values given in the Palik's handbook [131]. We used these data to calculate the Drude model parameters of the materials. The Drude model permittivity was given by the formula: $\varepsilon(\omega) = \varepsilon_\infty + \omega_p^{\,2} / \omega(\omega - i\upsilon_c)$ where ω_p was the plasma frequency and ν_c was the collision frequency. Our fit to the data of Palik's handbook implied $\omega_p = 13250x10^{12}\ rad/s$ and $\nu_c = 130\ THz$ for silver, $\omega_p = 12000x10^{12}\ rad/s$ and $\nu_c = 105\ THz$. We used this data set to model the dispersion properties of silver in our simulations for gold, and $\omega_p = 14500x10^{12}\ rad/s$ and $\nu_c = 5500\ THz$ for titanium. However, we found out from the experimental data that the collision frequency of our metals was not exactly the same as the one obtained from Drude model fits. Despite this, we used in our numerical analyses the values of ω_p and ν_c obtained from the fit to the data of Palik's handbook.

We show the simulated and measured absorption (A) derived from the scattering parameters: the magnitude of transmission ($|S_{21}|$), reflection ($|S_{11}|$) data in Figure 8.13. We observed a reflection dip at around the magnetic resonance frequency of the SRRs and as expected, the structure behaves as a resonant absorber. When the electromagnetic field impinges on the structure from port 1, the absorbance of the structure is calculated by the formula: $A = 1 - |S_{11}|^2 - |S_{21}|^2$. We obtained a *99.3%* absorbance peak at *250 THz* (*1200 nm*). The full width at 90% absorption was around *121 THz (825 nm)*. The total thickness of the absorber was $\tau = t_d + t_{Ti} + h = 185\ nm$, which corresponds to $\lambda/6.5$ at the central frequency of operation.

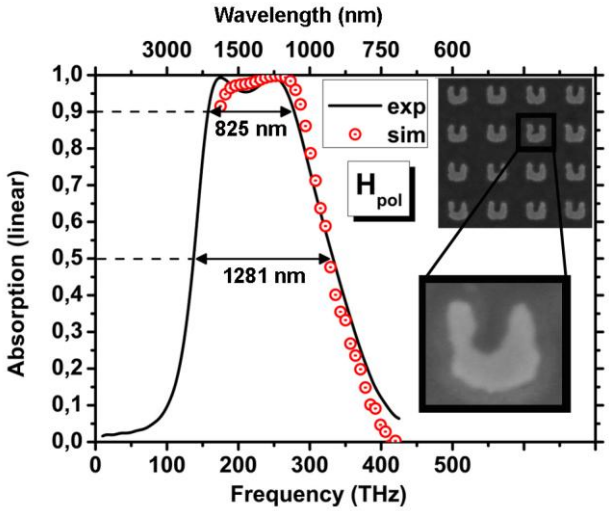

Figure 8.13. Numerical and experimental data of absorbance derived from scattering parameters. The SEM image of a section of the printed area and an example SRR are shown on the right.

The design here was to demonstrate the proof of concept, further optimization for specific application in terms of SRR parameters and film thicknesses are possible. For example as we increased the dielectric layer thickness we observed the absorption magnitude shows an oscillatory behavior, the maxima and minima depend on the surface impedance variation of the metamaterial layer. The minimum separation necessary between the metamaterial layer and the back metal for an absorption maximum was $\lambda_0/(4.9n_d)$ at the center frequency of operation (*250 THz*). Here, n_d is the index of dielectric layer and λ_0 is the magnetic resonance wavelength. The absorbance decreases and increases periodically as we vary the dielectric thickness. Higher order absorption maxima do not show a linear dependence on the dielectric layer thickness. Another example is the variation of the arm length *L*. It is an important parameter for determining the magnetic resonance frequency. We decreased the arm length from *104 nm* to *0 nm* and observed a quite strong shift of magnetic resonance frequency and thereby the absorption peak frequency. In this parametric variation the electrical resonance of the SRRs remained nearly the same while the magnetic resonance shifts from *199.5 THz* to *324.6 THz* when the arm length reduced from *104nm* to *35nm*. For the limiting case, $L = 0$, only the electrical

resonance was present. The only source of magnetic resonance of the SRR is the circulating currents that are driven by the split capacitance. As we decrease arm length to $L = 0\ nm$ the driven force of the circulating currents is eliminated and as a result, we expect to lose the absorbing peak at originated due magnetic resonance. The exciting conclusion is that by just changing L, we can change the resonance frequency considerably. One of the reasons of obtaining wide bandwidth in the experiments was the large parametric variations at the fabricated samples.

Up to now, we showed that the design works for normal incidence and single polarization. In the following sections, we improved the design to operate independent of incident polarization and we studied oblique response.

8.6.4. Polarization insensitive and wide bandwidth composite structure

We added a resistive sheet layer between the metamaterial and dielectric layer composed of very thin titanium (Ti). When studying the absorber configurations we observed that when there is only the metamaterial or resistive sheet at resonant frequency of the layer we find another reflection dip. Then we merged the two structures and the composite structures thereby had a larger bandwidth then the two cases and the absorption was based on the both mechanism. The thickness of the titanium layer was $t_{Ti} = 2\ nm$, SRR height was $h = 40\ nm$ and the dielectric layer thickness was $t_d = 110\ nm$ in the new design.

In order to achieve polarization independence, we changed the unit cell so that it is now composed of 4 SRRs: composed of elements parallel to the y-direction and the other elements that are parallel to the x-direction as shown in Figure 8.14. We saw that the simulated absorption spectra for incident wave polarization of $45°$ is the same as polarization angle $0°$ and $90°$ that clearly proves the polarization independent response. We conclude from these results that the absorber can be extended to operate as polarization independent.

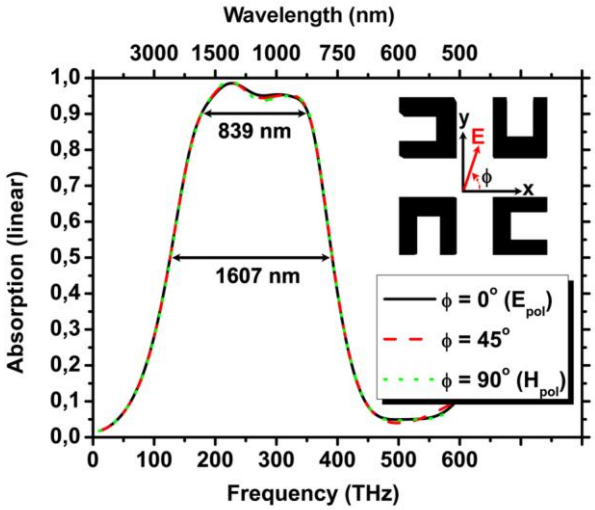

Figure 8.14. Polarization independent response and corresponding unit cell.

In Figure 8.15, we plotted power distribution, E- field amplitude and power flow at around the center frequency (*225 THz*) for the composite absorber. We saw the localization of the incident power between the silver metal layer and split ring resonator layer. The peak power enhancement at the dielectric region was quite high. We placed the SRR layer at a distance for maximum absorption: $\sim\lambda/5.7n_d$ apart in the dielectric layer. The index of the dielectric media was higher than free space and the impedance of the SRR layer was high. These conditions enable the reflected wave from the metal plate and the impinging fields combine to cancel out the total reflection from the structure.

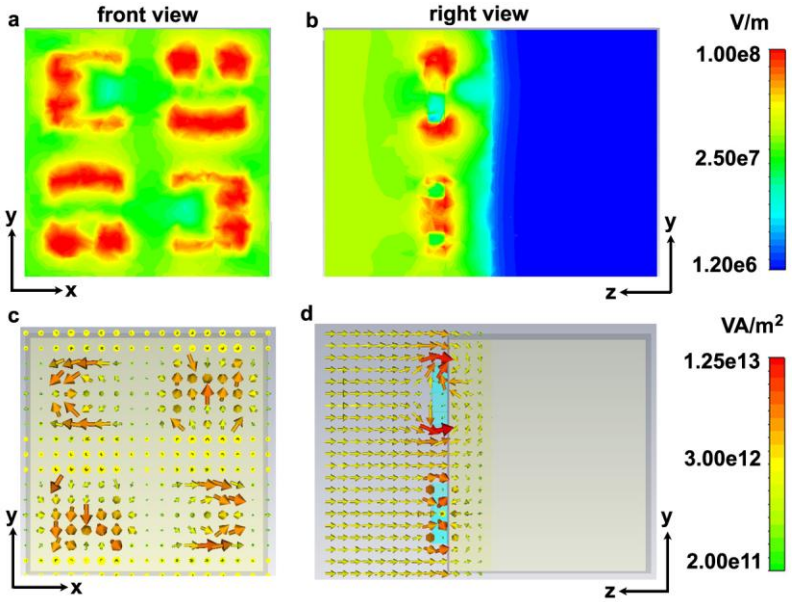

Figure 8.15. Spatial field distributions in the vicinity of split ring resonators at 225 THz frequency. (a) Electric field amplitude (b) Electric field distribution (c) Magnetic field distribution. Six unit cells were shown.

8.6.5. Oblique Response

In all the data presented so far, we have characterized the absorber for normal incidence only. For the oblique illumination study, we have investigated incidence angles of 20°, 40°, 60°, and 80° in the x-z and y-z planes. Figure 8.16 shows the spectral response for several angles of incidence, the peak absorption frequency changes and remains more than 70% up to 60° incidence angle. The excitation of SRRs is now partially electrically and partially magnetically originated. The details of orientation dependent excitation have been investigated in literature at the microwave and optical frequencies [136]. There was a slight shift of the operation frequency that slightly decreased the operation bandwidth. Even though the operation frequency of the absorber changed slightly the absorption values remained large for up to 60° at the x-y and y-z planes.

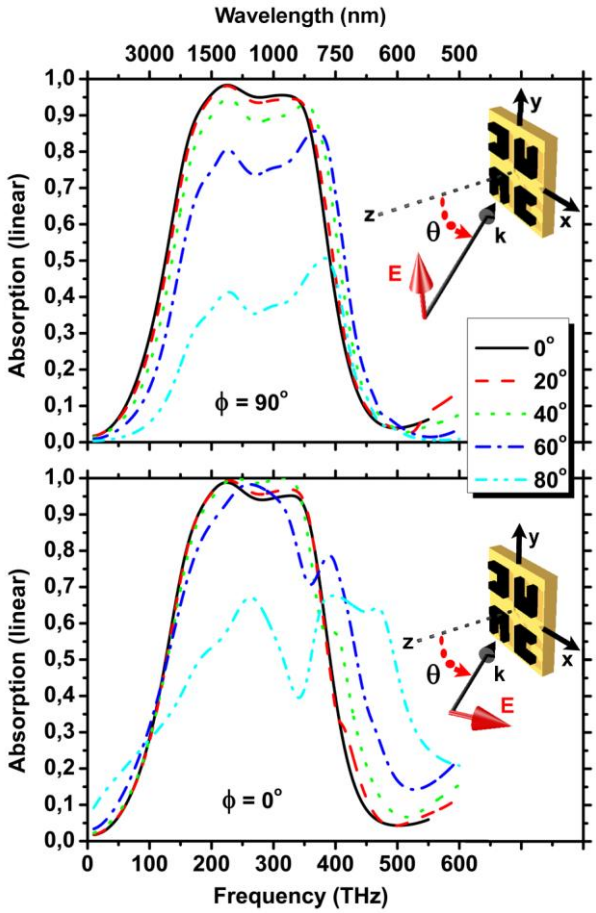

Figure 8.16. Simulated absorption response of the SRR based metamaterial absorber for several incidence angles.

Chapter 9

Conclusion

We investigated metamaterial elements and demonstrated unusual phenomena such as negative refraction, negative phase velocity, miniaturization of antennas, novel thin absorbers and enhanced transmission.

In chapter 2, we have demonstrated the results of our parametric study on the electrically small negative permeability medium particles that were fabricated via the standard printed circuit board technology. Increasing the side length of the particles and using higher permittivity substrates in turn decreases the electrical size significantly. On the other hand, there is a trade-off between the electrical size and the resonance strength of the particles. We analyzed a novel particle: the multi-spiral resonator and obtained ~ - 30 dB resonant dip with $\lambda_0/30$ electrical size at 0.81 GHz. Our particles are low profile and can be easily packed into three-dimensional arrays for antenna, superlens and absorber applications. Moreover, we obtained particles with strip width and separation as low as 50 μm and scaled them to operate at higher frequencies. We explained a method for digitally tuning the resonance frequency of the multi split structures. Finally, we have demonstrated that by inserting deep subwavelength resonators into periodically arranged subwavelength apertures complete transmission enhancement can be obtained at around the magnetic resonance frequency. The proposed application of the enhanced transmission is certainly an example of something extremely interesting for people working in optics and suggests a possible way to obtain it even at near-infrared and visible regimes. The only difference would be in the technology (for instance electron beam lithography instead of regular microwave printed circuit technology). Even though periodically arranged metallic resonators can produce a negative permeability

medium, the resonant response weakens at extreme regimes under certain conditions, which is the major problem of obtaining a negative index at the visible regime. We report that by decreasing the operation temperature, the metal conductivity can be increased, enhanced negative permeability can be obtained and the operation range of the negative permeability media, and thereby the negative index media, can be extended. We doubled the resonant strength of a typical resonator operating at microwave frequencies by decreasing its temperature to 150 K. The results are promising for the demonstration of negative-index media at the visible regime.

In chapter 3, characterization of split ring resonator-based metamaterial operating at 100 GHz was demonstrated in terms of the transmission based qualitative effective medium theory and the standard retrieval analysis. The structure layers were produced via printed circuit board technology and the transmission response for increasing the number of layers at the propagation direction was analyzed. We observed a stop-band for the SRR-only medium and pass-band for the CMM medium at around 100 GHz. The transmission peak value was ~ -2.5 dB and the metamaterials' average loss was ~ 2.5 dB / mm. The experimental results were not very sensitive to the layer disorders or the angle of incidence, and they were in good agreement with the numerical calculations. The far field radiation response of horn antenna and metamaterial slab composite had a lower angular width, which was verified both numerically and experimentally. By constructing a metamaterial prism and performing angular scan experiments we confirmed the retrieved negative index property of a split ring resonator based metamaterial. We confirmed by direct field scan measurements, a one-dimensional metamaterial lens that is designed to be double negative by using the qualitative effective medium theory, in which it indeed refracts the obliquely incident waves to the negative direction. The study was performed both experimentally and numerically at around 100 GHz.

In chapter 4, characterization of a planar metamaterial operating at 100 GHz is demonstrated in terms of the qualitative effective medium theory and the standard retrieval analysis. The structure layers are produced via printed circuit board technology and then the transmission response for the increasing number of layers is analyzed. When the linear polarization of the incident field changes, the transmission data remains the same if the angle between the structure plane and propagation vector is kept fixed. This is due to the x-y plane symmetric design of the metamaterial. We also characterized a planar metamaterial operating at 21 GHz by using a quantitative effective medium theory. The planar metamaterial was the fishnet structure, which is symmetric with respect to the $x = \pm y$ plane. The operation frequency of the fishnet metamaterial is higher than the corresponding cut-wire pair magnetic resonance frequency. The left-handed nature of the transmission peak is identified unambiguously by using the shorted CMM structure. The experimental phase data strengthens the indication of the negative index of refraction. By investigating the planar metamaterials at microwave frequencies several contributions can be added to the study of metamaterials at optical frequencies.

In chapter 5, we demonstrated the fishnet metamaterial case for which the incidence angle is nonzero. The response of the medium changes very quickly as we increase the angle of incidence. We demonstrated that planar metamaterials are sensitive to the angle of incidence and this is a major drawback for superlens applications. Moreover, we systematically studied a three-layered SRR-based metamaterial slab oblique response and showed that the negative index characteristics remain nearly the same up to incidence angle of 45°. The negative transmission band remained almost the same for two different bases of rotation. The insensitivity of SRR based metamaterials to the angle of incidence makes them a good candidate for metamaterial applications especially the superlens.

In chapter 6, we were able to obtain resonant antennas with efficiencies exceeding 40% by electrically exciting the SRRs placed on a ground plane. The sizes of the antenna were less than $\lambda_0/10$. We conclude that metamaterials can play a role in the development of ESAs. We observed that as we continued decreasing the resonant frequency of the SRRs, the maximum theoretical gain and simultaneously the gain decreased. Therefore, we can estimate the limit of our method, which is used to miniaturize antennas. Moreover, it is important to note that when excited properly, SRRs above a ground plane radiate efficiently. These results can have applications in future wireless systems and in the development of the steerable phased array antennas. Secondly, by introducing multi-SRRs we can observe the antenna beam direction shifts. This property might lead us to steerable antennas that are composed of SRRs. By electrically exciting two perpendicularly placed SRRs with different electrical sizes, we were able to obtain an electrically small, single fed, resonant antenna with efficiencies of 15% to 40%. The size of the antenna was less than $\lambda/10$ at the two operation frequencies 4.72 GHz and 5.76 GHz. The dual polarization nature of this antenna enables operation for the two modes at perpendicular polarization states. This antenna has applications as a single receiver element or a unit cell element of a metamaterial based phased array antenna. We also studied electrically small single layer metamaterial loaded patch antennas. These results constitute proof for the usefulness of metamaterial concepts in the antenna miniaturization problem. An MSRR medium loaded antenna had an electrical size of $\lambda/3.69$ and *40%* efficiency. We demonstrated that by loading the patch via an SR medium, a further miniaturization is possible. This miniaturization technique is potentially promising for antenna applications. However, rather sophisticated fabrication and characterization facilities are needed in order to demonstrate the limits of these antennas.

In chapter 7, we showed that the concept of metamaterials has proven to be useful in yet another field of microwave engineering, i.e. microwave absorbers. For a metal backed metamaterial absorber, we demonstrated the relation

between the electrical thickness and the absorbance peak. The origin of the absorbance was proven to be the magnetic resonance of the constituting artificial magnetic material inclusions. For approximately *λ/5* of total electrical thickness, we achieved an almost perfect absorption with a *8%* fractional bandwidth by using SRR of *λ/10* electrical size. As we used metamaterial elements of a smaller electrical size, such as MSRR, we were able to reduce the absorber thickness accordingly. Moreover, we demonstrated another type of absorber: a metamaterial backed resistive sheet. Almost perfect absorbance was also achieved for this case, with *λ/5* total electrical thickness and *8%* fractional bandwidth. These proofs of concepts may open the door to a) even more miniaturized microwave absorbers, employing deeply sub-wavelength magnetic inclusions and b) tunable devices employing either externally controlled capacitors connected to the magnetic resonators or light-induced conductivity changes of the material filling the splits of the SRR and MSRR. These concepts can be also extended to the THz and infrared regimes of the electromagnetic spectrum[48], by scaling the physical size of the metamaterial elements and taking into account the material properties of metals, which, due to the increased losses, may, indeed, help to reduce the complexity of the designs.

In chapter 8, we clearly demonstrated the possible effects of split ring resonator orientations on the transmission response at the optical regime. Depending on the application, a different orientation and correspondingly different modes can be utilized. When the thickness of the substrate on which the split ring resonators were printed was very small, it may affect the magnetic resonance frequency. We can mimic this behavior by coating a thick substrate with a very thin buffer layer. The magnetic resonance frequency can be fine tuned by changing the buffer layer thickness. For a densely packed split ring resonator array, a stronger coupling yielded an increased the fractional bandwidth of the magnetic stop band, as well as an increased the resonance strength. When the split ring resonators were loosely packed, the response was very weak and very similar to that in a single resonator case. The magnetic

resonance frequency was strongly dependent on the parameter: arm length (L) of the split ring resonators. A slight change in the arm length leads to a significant shift of the magnetic resonance frequency. The resonant behavior of metamaterials at the optical regime strongly depends on the characteristics of the utilized metal. There was a 139 THz difference between the magnetic resonance frequencies of silver- and perfect electrical conductor- based split ring resonator media.

We incorporated the split ring resonators in the numerical domain to provide an alternative solution to the problem of enhanced transmission. Compared to the Ebbesen results, we obtained a 31 times larger enhancement from a 2000 times smaller radiating aperture area. Furthermore, the fields were radiated to the far field with 3.9 dBi directivity, which is suitable for real world applications at the optical regime.

Finally, we demonstrated metamaterial incorporated absorber configurations operating at the optical regime. For a metal backed metamaterial absorber, we demonstrated the relation between the electrical thickness and the absorbance peak. The origin of the absorbance was proven to be the magnetic resonance of the constituting artificial magnetic material inclusions. For approximately $\lambda/6$ of total electrical thickness, we achieved an almost full absorption with a 42% fractional bandwidth by using subwavelength SRRs. As a proof of concept, we demonstrated a composite absorber with 185 nm thickness and obtained minimum 90% absorption between 1078 nm to 2183 nm free space wavelengths. As the next step we demonstrated a design that is polarization independent and wider bandwidth that composed of an electrical screen in addition to the present magnetic metamaterial screen. We finalized the analysis by demonstrating the oblique response of the superior absorber design. We observed up to 60° incidence angle the absorption remains above 70%. Utilization of magnetic resonance at the optical regime can have applications in various important areas such as photovoltaic thin film solar cells, military stealth technologies, thermal isolation, infrared photodetectors, and biosensors.

BIBLIOGRAPHY

1. R. A. Shelby, D. R. Smith, S. Schultz, *Experimental verification of a negative index of refraction.* Science, 2001. 292: p. 77-79.
2. J. B. Pendry, A. J. Holden, D. J. Robbins, W. J. Stewart, *Magnetism from conductors and enhanced nonlinear phenomena.* IEEE Trans. Microwave Theory Tech., 1999. 47: p. 2075-2084.
3. K. B. Alici, E. Ozbay, *Characterization and tilted response of a fishnet metamaterial operating at 100 GHz.* J. Phys. D: Appl. Phys., 2008. 41: p. 135011.
4. M. Gokkavas, K. Guven, I. Bulu, K. Aydin, R. S. Penciu, M. Kafesaki, C. M. Soukoulis, E. Ozbay, *Experimental demonstration of a left-handed metamaterial operating at 100 GHz.* Phys. Rev. B, 2006. 73: p. 193103.
5. B. D. F. Casse, M. O. Moser, J. W. Lee, M. Bahou, S. Inglis, L. K. Jian, *Towards three-dimensional and multilayer rod-split-ring metamaterial structures by means of deep x-ray lithography.* Appl. Phys. Lett., 2007. 90: p. 254106.
6. S. Zhang, W. Fan, K. J. Malloy, S. R. J. Brueck N. C. Panoiu, R. M. Osgood, *Near-infrared double negative metamaterials.* Opt. Express, 2005. 13: p. 4922-4930.
7. K. Buell, H. Mosallaei, K. Sarabandi, *A substrate for small patch antennas providing tunable miniaturization factors.* IEEE Trans. Microwave Theory Tech., 2006. 54: p. 135-146.
8. A. Alu, F. Bilotti, N. Engheta, L. Vegni, *Subwavelength compact resonant patch antennas loaded with metamaterials.* IEEE Trans. Antennas Propag., 2007. 55: p. 13-25.
9. K. B. Alici, E. Ozbay, *Electrically small split ring resonator antennas.* J. Appl. Phys., 2007. 101: p. 083104.
10. K. B. Alici, E. Ozbay, *Radiation properties of a split ring resonator and monopole composite.* Phys. Status Solidi B, 2007. 244: p. 1192-1196.

11. A. Erentok, R. Ziolkowski, *A hybrid optimization method to analyze metamaterial-based electrically small antennas.* IEEE Trans. Antennas Propag., 2007. 55: p. 731-741.
12. A. Alu, F. Bilotti, N. Engheta, L. Vegni, *Metamaterial covers over a small aperture.* IEEE Trans. Antennas Propag., 2006. 54: p. 1632-1643.
13. D. Sievenpiper, L. Zhang, R. F. J. Broas, N. G. Alexopolous, E. Yablonovitch, *High-impedance electromagnetic surfaces with a forbidden frequency band.* IEEE Trans. Microwave Theory Tech., 1999. 47: p. 2059-2074.
14. A. Ourir, A. Lustrac, J. M. Lourtioz, *All-metamaterial-based subwavelength cavities (λ/60) for ultrathin directive antennas.* Appl. Phys. Lett., 2006. 88: p. 084103.
15. J. Garcia-Garcia, F. Martin, F. Falcone, J. Bonache, J. d. Baena, I. Gil, E. Amat, T. Lopetegi, M. A. G. Laso, J. A. M. Iturmendi, M. Sorolla, R. Marques, *Microwave filters with improved stopband based on sub-wavelentgh resonators.* IEEE Trans. Microwave Theory Tech., 2005. 53: p. 1997-2006.
16. J. Bonache, I. Gil, J. Garcia-Garcia, F. Martin, *Novel microstrip bandpass filters based on complementary split-ring resonators.* IEEE Trans. Microwave Theory Tech., 2006. 18: p. 265-271.
17. F. Falcone, F. Martin, J. Bonache, M. A. G. Laso, J. Garcia-Garcia, J. D. Baena, R. Marques, M. Sorolla, *Stop-band and band-pass characteristics in coplanar waveguides coupled to spiral resonators.* Microw. Opt. Tech. Lett., 2004. 42: p. 386-388.
18. C. G. Parazzoli, R. B. Greegor, K. Li, B. E. C. Koltenbah, M. Tanielian, *Experimental Verification and simulation of negative index of refration using Snell's law.* Phys. Rev. Lett., 2003. 90: p. 107401.
19. S. He, Y. Jin, Z. Ruan, J. Kuang, *On subwavelength and open resonators involving matematerials of negative refraction index.* New J. Phys., 2005. 7: p. 210.

20. S. Guenneau, S. A. Ramakrishna, S. Enoch, S. Chakrabarti, G. Tayeb, B. Gralak, *Cloaking and imaging effects in plasmonic checkerboards of negative ε and μ and dielectric photonic crystal checkerboards.* Photonics Nanostruct., 2007. 5: p. 63-72.
21. J. B. Pendry, D. Schurig, D. R. Smith, *Controlling electromagnetic fields.* Science, 2006. 312: p. 1780-1782.
22. A. Alu, N. Engheta, *Plasmonic materials in transparency and cloaking problems: mechanism, robustness, and physical insights.* Opt. Express, 2007. 15: p. 3318-3332.
23. F. Bilotti, S. Tricarico, L. Vegni, *Electromagnetic cloaking devices for TE and TM polarizations.* New J. Phys., 2008. 10: p. 115035.
24. L. Zhang, G. Tuttle, C. M. Soukoulis, *GHz magnetic response of split ring resonators.* Photonics Nanostruct., 2004. 2: p. 155-159.
25. O. Sydoruk, A. Radkovskaya, O. Zhuromskyy, E. Shamonina, M. Shamonin, C. J. Stevens, G. Faulkner, D. J. Edwards, L. Solymar, *Tailoring the near field guiding properties of magnetic metamaterials with two resonant elements per unit cell.* Phys. Rev. B, 2006. 73: p. 224406.
26. K. Aydin, E. Ozbay, *Capacitor-loaded split ring resonators as tunable metamaterial components.* J. Appl. Phys., 2007. 101(024911).
27. I. Gil, J. Garcia-Garcia, J. Bonache, F. Martin, M. Sorolla, R. Marques, *Varactor-loaded split ring resonators for tunable notch filters at microwave frequencies.* Electron. Lett., 2004. 40: p. 1347-1348.
28. M. C. K. Wiltshire, J. B. Pendry, I. R. Young, D. J. Larkman, D. J. Gilderdale, J. V. Hajnal, *Microstructured Magnetic Materials for RF Flux Guides in Magnetic Resonance Imaging.* Science, 2001. 291: p. 849-851.
29. M. C. K. Wiltshire, E. Shamonina, I. R. Young, and L. Solymar, *Dispersion sharacteristics of magneto-inductive waves: Comparison between theory and experiment.* Electron. Lett., 2003. 39: p. 215-217.

30. J.D. Baena, R. Marques, F. Medina, and J. Martel, *Artificial magnetic metamaterial design by using spiral resonators.* Phys. Rev. B, 2004. 69: p. 014402.
31. R. R. A. Syms, I. R. Young, and L. Solymar, *Low loss magneto-inductive waves.* J. Phys. D: Appl. Phys., 2006. 39: p. 3945-3951.
32. K. B. Alici, F. Bilotti, L. Vegni, E. Ozbay, *Miniaturized negative permeability materials.* Appl. Phys. Lett., 2007. 91: p. 071121.
33. F. Bilotti, A. Toscano, L. Vegni, K. Aydin, K. B. Alici, E. Ozbay, *Equivalent-circuit models for the design of metamaterials based on artificial magnetic inclusions.* IEEE Trans. Microwave Theory Tech., 2007. 55: p. 2865-2873.
34. F. Aznar, M. Gil, J. Bonache, J. Garcia-Garcia, F. Martin, *Metamaterial transmission lines based on broad-side coupled spiral resonators.* Electron. Lett., 2007. 43: p. 530-532.
35. I. Bahl, P. Bhartia, *Microwave Solid State Circuit Design*. 2003, New York: Wiley.
36. L. J. Chu, *Physical limitations of omni-directional antennas.* J. Appl. Phys., 1948. 19: p. 1163-1175.
37. CST, GmbH, *CST-Microwave Studio*. 2009: Darmstadt, Germany.
38. F. Bilotti, A. Toscano, L. Vegni, *Design of Spiral and Multiple Split-Ring Resonators for the Realization of Miniaturized Metamaterial Samples* IEEE Trans. Antennas Propag., 2007. 55: p. 2258-2267.
39. C.R. Simovski, A.A. Sochava, Progress Electromag. Research, 2003. 43: p. 239.
40. C. J. Panagamuwa, A. Chauraya, J. C. Vardaxoglou, *Frequency and beam reconfigurable antenna using Photoconducting switches.* IEEE Trans. Antennas Propag., 2006. 54: p. 449-454.
41. J. Zhou, Th. Koschny, M. Kafesaki, E. N. Economou, J. B. Pendry, C. M. Soukoulis, *Saturation of the magnetic response of split-ring resonators at optical frequencies.* Phys. Rev. Lett., 2005. 95: p. 223902.

42. G.Dolling, M. Wegener, C. M. Soukoulis, S. Linden, Opt. Lett., 2007. 32: p. 53-55.
43. C. Enkrich, M. Wegener, S. Linden, S. Burger, L. Zschiedrich, F. Schmidt, J. F. Zhou, Th. Koschny, C. M. Soukoulis, *Magnetic metamaterials at telecommunication and visible frequencies.* Phys. Rev. Lett., 2005. 95: p. 203901.
44. K. B. Alici, E. Ozbay, *A planar metamaterial: Polarization independent fishnet structure.* Photonics Nanostruct., 2008. 6: p. 102-107.
45. G. Dolling, G. Enkrich, M. Wegener, j. F. Zhou, C. M. Soukoulis, S. Linden, Opt. Lett., 2005. 30: p. 3198-3200.
46. S. Linden, C. Enkrich, M. Wegener, J. Zhou, Th. Koschny, C. M. Soukoulis, *Magnetic response of matematerials at 100 Terahertz.* Science, 2004. 306: p. 1351-1353.
47. N. F. Mott, Proc. R. Soc. London A, 1936. 153: p. 669.
48. N. W. Ashcroft, N. D. Mermin, ed. *Solid State Physics*. 1976, Saunders College, Fort Worth. 66.
49. I. S. Grigoriev, E. Z. Meilikhov, *Handbook of Physical Quantities*. 1997: CRC Press Inc.
50. J. B. Pendry, A. J. Holden, W. J. Stewart, I. Youngs, *Extremely low frequency plasmons in metallic mesostructures.* Phys. Rev. Lett., 1996. 76: p. 4773-4776.
51. L. Peng, L. Ran, H. Chen, H. Zhang, J. A. Kong, T. M. Grzegorczyk, *Experimental observation of left-handed behavior in an array of standard dielectric resonators.* Phys. Rev. Lett., 2007. 98: p. 157403.
52. Q. Zhao, B. Du, L. Kang, H. Zhao, Q. Xie, B. Li, X. Zhang, J. Zhou, L. Li, Y. Meng, *Tunable negative permeability in an isotropic dielectric composite.* Appl. Phys. Lett., 2008. 92: p. 051106.
53. H. Zhao, J. Zhou, Q. Zhao, B. Li, L. Kang, Y. Bai, *Magnetotunable left-handed material consisting of yttrium iron garnet slab and metallic wires.* Appl. Phys. Lett., 2007. 91: p. 131107.

54. A. Pimenov, A. Loidl, P. Przyslupski, B. Dabrowski, *Negative refraction in ferromagnet-superconductor superlattices.* Phys. Rev. Lett., 2005. 95: p. 247009.

55. O. G. Vendik, M. S. Gashinova, *Artificial Double Negative (DNG) Media Composed by Two Different Sphere Lattices Embedded in a Dielectric Matrix* Proc. 34th European Microwave Conference - Amsterdam, 2004: p. 1209-1212.

56. A. Ahmadi, H. Mosallaei, *Physical configuration and performance modeling of all-dielectric metamaterials.* Phys. Rev. B, 2008. 77: p. 045104(1)-045104(11).

57. C. L. Holloway, E. F. Kuester, J. Baker-Jarvis, P. Kabos, *A double negative (DNG) composite medium composed of magnetodielectric spherical particles embedded in a matrix.* IEEE Trans. Antennas Propag., 2003. 51: p. 2596-2603.

58. S. Ghadarghadr, H. Mosallaei, *Dispersion diagram characteristics of periodic array of dielectric and magnetic materials based spheres.* IEEE Trans. Antennas Propag., 2009. 57: p. 149-160.

59. K. B. Alici, F. Bilotti, L. Vegni, E. Ozbay, *Optimization and tunability of deep subwavelength resonators for metamaterial applications: complete enhanced transmission through a subwavelength aperture.* Opt. Express, 2009. 17: p. 5933-5943.

60. I. Bulu, H. Caglayan, E. Ozbay, *Beaming of Light and Enhanced Transmission via Surface Modes of Photonic Crystals.* Opt. Lett., 2005. 30: p. 3078-3080.

61. S. S. Akarca-Biyikli, I. Bulu, E. Ozbay, *Enhanced transmission of microwave radiation in one-dimensional metallic gratings with sub-wavelength aperture.* Appl. Phys. Lett., 2004. 85: p. 1098-1100.

62. I. Bulu, H. Caglayan, E. Ozbay, *Highly directive radiation from sources embedded inside photonic crystals.* Appl. Phys. Lett., 2003. 83: p. 3263-3265.

63. H. Caglayan, I. Bulu, E. Ozbay, *Extraordinary grating-coupled microwave transmission through a subwavelength annular aperture.* Opt. Express 2005. 13: p. 1666-1668.
64. K. Aydin, I. Bulu, E. Ozbay, *Subwavelength resolution with a negative-index metamaterial superlens.* Appl. Phys. Lett., 2007. 90: p. 254102.
65. F. Bilotti, A. Toscano, L. Vegni, *Design of Spiral and Multiple Split-Ring Resonators for the Realization of Miniaturized Metamaterial Samples.* IEEE Trans. Antennas Propag., 2007. 55: p. 2258-2267.
66. M. W. Klein, C. Enkrich, M. Wegener, *Single-slit split-ring resonators at optical frequencies: limits of size scaling.* Opt. Lett., 2006. 31: p. 1259-1261.
67. N. Katsarakis, G. Konstantinidis, A. Kostopoulos, R. S. Penciu, T. F. Gundogdu, M. Kafesaki, E. N. Econoumou, Th. Koschny, C. M. Soukoulis, *Magnetic response of split-ring resonators in the far-infrared frequency regime.* Opt. Lett., 2005. 30: p. 1348-1351.
68. A. Ishikawa, T. Tanaka, S. Kawata, *Negative magnetic permeability in the visible light region.* Phys. Rev. Lett., 2005. 95: p. 237401.
69. S O'Brien, D. McPeake, S. A. Ramakrishna, J. B. Pendry, *Near-infrared photonic band gaps and nonlinear effecs in negative magnetic metamaterials.* Phys. Rev. B, 2004. 69: p. 241101.
70. K. Aydin, K. Guven, M. Kafesaki, C. M. Soukoulis, E. Ozbay, *Investigation of magnetic resonances for different split-ring resonator parameters and designs.* New J. Phys., 2005. 7: p. 168(1)-168(15).
71. A. N. Grigorenko, A. K. Geim, H. F. Gleeson, Y. Zhang, A. A. Firsov, I. Y. Khrushchev, J. Petrovic, *Nanofabricated media with negative permeability at visible frequencies.* Nature, 2005. 438: p. 17-20.
72. K. B. Alici, E. Ozbay, *Low-temperature behavior of magnetic metamaterial elements.* New J. Phys., 2009. 11: p. 043015.
73. E. Ozbay, K. Aydin, E. Cubukcu, M. Bayindir, *Transmission and Reflection Properties of Composite Double Negative Metamaterials in Free Space.* IEEE Trans. Antennas Propag., 2003. 51: p. 2592-2595.

74. Th. Koschny, M. Kafesaki, E. N. Economou, C. M. Soukoulis, *Effective medium theory of lefthanded materials.* Phys. Rev. Lett., 2004. 93: p. 107402.
75. K. B. Alici, E. Ozbay, *Oblique response of a split-ring resonator based left-handed metamaterial slab.* Opt. Lett., 2009. 34: p. 2294-2296.
76. K Aydin, K. Guven, N. Katsarakis, C. M. Soukoulis, E. Ozbay, *Effect of disorder on magnetic resonance band gap of split-ring resonator structures.* Opt. Express 2004. 12: p. 5896-5901.
77. D. R. Smith, S. Shultz, P. Markos, C. M. Soukoulis, *Determination of effective permittivity and permeability of metamaterials from reflection and transmission coefficients.* Phys. Rev. B, 2002. 65: p. 195104.
78. X. Chen, T. M. Grzegorczyk, B. I. Wu, J. Pacheco, J. A. Kong, *Robust method to retrieve the constitutive effective parameters of metamaterials.* Phys. Rev. E, 2004. 70: p. 016608.
79. D. R. Smith, D. C. Vier, Th. Koschny, C. M. Soukoulis, *Electromagnetic parameter retrieval from inhomogeneous metamaterials.* Phys. Rev. E, 2005. 70: p. 036617.
80. K. B. Alici, E. Ozbay, *Oblique response of a split-ring-resonator-based left-handed metamaterial slab.* Opt. Lett., 2009. 34: p. 2294-2296.
81. T. J. Yen, W. J. Padilla, N. Fang, D. C. Vier, D. R. Smith, J. B. Pendry, D. N. Basov, X. Zhang, Science, 2004. 303: p. 1494.
82. S. Zhang, W. Fan, B. K. Minhas, A. Frauenglass, K. J. Malloy, S. R. J. Brueck, Phys. Rev. Lett., 2005. 94: p. 037402.
83. S. Zhang, W. Fan, N. C. Panoiu, K. J. Malloy, R. M. Osgood, S. R. J. Brueck, Phys. Rev. Lett., 2005. 95: p. 137404.
84. V. M. Shalaev, W. Cai, U. K. Chettiar, H. Yuan, A. K. Sarychev, V. P. Drachev, A. V. Kildishev, Opt. Lett., 2005. 30: p. 3356.
85. K. Guven, M. D. Caliskan, E. Ozbay, Opt. Express, 2006. 14: p. 8685.
86. J. Zhou, L. Zhang, G. Tuttle, T. Koschny, C. M. Soukoulis, Phys. Rev. B, 2006. 73: p. 041101.

87. M. Kafesaki, I. Tsiapa, N. Katsarakis, Th. Koschny, C. M. Soukoulis, E. N. Economou, Phys. Rev. B, 2007. 75: p. 235114.
88. J. B. Pendry, *Negative Refraction Makes a Perfect Lens.* Phys. Rev. Lett., 2000. 85: p. 3966.
89. H. A. Wheeler, *Fundamental limitations of small antennas.* Proc. IRE, 1947. 49: p. 1479-1484.
90. R. C. Hansen, *Fundamental limitations in antennas.* Proc. IEEE, 1981. 69: p. 170-182.
91. C. A. Balanis, *Antenna Theory: Analysis and Design*. 1997, New York: Wiley.
92. J. C. E. Sten, A. Hujanen, P. K. Koivisto,, *Quality factor of an electrically small antenna radiating close to a conducting plane.* IEEE Trans. Antennas Propag., 2001. 49: p. 829-837.
93. J. S. McLean, *A re-examination of the fundamental limits on the radiation Q of electrically small antennas.* IEEE Trans. Antennas Propag., 1996. 44: p. 672-676.
94. W. Geyi, P. Jarmuszewski, Y. Qi,, *The Foster reactance theorem for antennas and radiation Q.* IEEE Trans. Antennas Propag., 2000. 48: p. 401-408.
95. J. B. Pendry, *Metamaterials in the sunshine.* Nature Mater., 2006. 5: p. 599-600.
96. C. M. Soukoulis, M. Kafesaki, E. N. Economou, *Negative-Index Materials: New Frontiers in Optics.* Adv. Mater., 2006. 18: p. 1941-1952.
97. K. Buell, H. Mosallaei, K. Sarabandi,, *A substrate fo small patch antennas providing tunable miniaturization factors.* IEEE Trans. Microwave Theory Tech., 2006. 54: p. 135-146.
98. S. Hrabar, J. Bartolic, Z. Sipus, *Waveguide miniaturization using uniaxial negative permeability metamaterial.* IEEE Trans. Antennas Propag., 2005. 53: p. 110-119.

99. M. E. Ermutlu, C.R.S., M. K. Karkkainen, P. Ikonen, S. A. Tretyakov, A. A. Sochava, *Miniaturization of patch antennas with new artificial magnetic layers*, in *Intenational Workshop on Antenna Technology: Small Antennas and Novel Metamaterials*. 2005, IEEE: New York. p. 87-90.
100. F. Qureshi, M.A.A., G. V. Eleftheriades, *A compact and low-profile metamaterial ring antenna with vertical polarization.* IEEE Antennas Wireless Propag. Lett., 2005. 4: p. 333-336.
101. P. Ikonen, S. Maslovski, C. Simovski, S. Tretyakov, *On artificial megneto-dielectric loading for improving the impedance bandwidth properties of microstrip antennas.* IEEE Trans. Antennas Propag., 2006. 54: p. 1654-1662.
102. G. A. Thiele, P. L. Detweiler, R. P. Penno, IEEE Trans. Antennas Propag., 2003. 51: p. 1263.
103. R. L. Fante, *Maximum possible gain for an arbitrary ideal antenna with specified quality factor*. IEEE Trans. Antennas Propag., 1992. 40: p. 1586-1588.
104. E. D. Isaacs, P. M. Platzman, and J. T. Shen, *Resonant Antennas.* US Patent 6,879,298, 2005.
105. P. G. Balmaz, O. J. F. Martin, J. Appl. Phys., 2002. 92: p. 2929.
106. D. F. Sievenpiper, *Steerable leaky wave antenna capable of both forward and backward direction.* US Patent Application 20040227668, 2004.
107. A. Lai, C. Caloz, and T. Itoh, IEEE Microw. Mag., 2004. 5: p. 34.
108. A. Grbic, G.V. Eleftheriades, J. Appl. Phys., 2002. 95: p. 5930.
109. A. Alu, F. Bilotti, N. Engheta, L. Vegni, *Subwavelength, compact, resonant patch antennas loaded with metamaterials.* IEEE Trans. Antennas Propag., 2007. 55: p. 13-25.
110. K. B. Alici, E. Ozbay, *Direct observation of negative refraction at the millimeter-wave regime by using a flat composite metamaterial.* J. Opt. Soc. Am. B, 2009. 26: p. 1688-1692.

111. W. W. Salisbury, *Absorber body for electromagnetic waves*, U.S. Patent 2599944, Editor. 1952.
112. D. R. Smith, J. B. Pendry, M. C. K. Wiltshire, *Metamaterials and Negative Refractive Index.* Science, 2004. 305: p. 788-790.
113. K. B. Alici, E. Ozbay, *Theoretical study and experimental realization of a low-loss metamaterial operating at the millimeter-wave regime: Demonstrations of flat and prism shaped samples.* IEEE Journal of Selected Topics in Quantum Electronics, 2010. 16: p. 386-393.
114. A. Alu, F. Bilotti, N. Engheta, L. Vegni, *Theory and Simulations of a Conformal Omni- Directional Subwavelength Metamaterial Leaky-Wave Antenna.* IEEE Trans. Antennas Propag., 2007. 55: p. 1698-1708.
115. F. Bilotti, A. Alu, L. Vegni, *Design of Miniaturized Metamaterial Patch Antennas with μ-Negative Loading.* IEEE Trans. Antennas Propag., 2008. 56: p. 1640-1647.
116. F. Bilotti, L. Scorrano, E. Ozbay, L. Vegni, *Enhanced Transmission Through a Sub-Wavelength Aperture: Resonant Approaches Employing Metamaterials.* J. Opt. A: Pure Appl. Opt., 2009. 11: p. 114029.
117. F. Bilotti, A.A., N. Engheta, L. Vegni, *Sub-Wavelength, Compact, Resonant Patch Antennas Loaded with Metamaterials.* IEEE Trans. Antennas Propag., 2007. 55: p. 13-25.
118. F. Qureshi, M. A. Antoniades, G. V. Eleftheriades, *A compact and low-profile metamaterial ring antenna with vertical polarization.* IEEE Antennas Wireless Propag. Lett., 2005. 4: p. 333-336.
119. N. Fang, Xiang Zhang,, *Imaging properties of a metamaterial superlens.* Appl. Phys. Lett., 2003. 82(2): p. 161-163.
120. D. J. Kern, D. H. Werner,, *A genetic algorithm approach to the design of ultra-thin electromagnetic bandgap absorbers.* Microw. Opt. Tech. Lett., 2003. 38: p. 61-64.
121. F. Bilotti, A. Alu, N. Engheta, L. Vegni, *Metamaterial sub-wavelength absorbers.* Proceedings of the 2005 Nanoscience and Nanotechnology Symposium - NN2005 (Frascati, Italy), 2005.

122. H. Mosallaei, K. Sarabandi,, *A one-layer ultra-thin meta-surface absorber.* 2005 IEEE Antennas and Propagation Society International Symposium, 2005. 1B: p. 615-618.
123. N. I. Landy, S. Sajuyigbe, J. J. Mock, D. R. Smith, W. J. Padilla, *Perfect metamaterial absorber.* Phys. Rev. Lett., 2008. 100: p. 207402.
124. F. Bilotti, L. Nucci, L. Vegni, *An SRR based microwave absorber.* Microw. Opt. Technol. Lett., 2006. 48: p. 2171-2175.
125. D. K. Ghodgaonkar, V. V. Varadan, V. K. Varadan,, *A free-space method for measurement of dielectric constants and loss tangents at microwave frequencies.* IEEE Trans. Instrum. Meas., 1989. 38: p. 789-793.
126. F. Bilotti, L. Vegni, *Design of metamaterial-based resonant microwave absorbers with reduced thickness and absence of a metallic backing.* Metamaterials and plasmonics: fundamentals, modeling, applications, 2009.
127. Hou-Tong Chen, Willie J. Padilla, Joshua M. O. Zide, Arthur C. Gossard, Antoinette J. Taylor, Richard D. Averitt, *Active terahertz metamaterial devices.* Nature, 2006. 444: p. 597-600.
128. H. A. Bethe, *Theory of diffraction by small holes.* Phys. Rev., 1944. 66: p. 163-182.
129. C. Genet, T. W. Ebbesen, *Light in tiny holes.* Nature, 2007. 445: p. 39-46.
130. E. Ozbay, *Plasmonics: Merging Photonics and Electronics at Nanoscale Dimensions.* Science, 2006. 311: p. 189-193.
131. E. D. Palik, *Handbook of optical constants of solids*. 1998, San Diego: Academic Press.
132. V. V. Nikolskiy, *Theory of electromagnetic field*. 1964, Moscow: Vysshaya Shkola Press.
133. M. Husnik, M. W. Klein, N. Feth, M. Konig, J. Niegemann, K. Busch, S. Linden, M. Wegener, *Absolute extinction cross-section of individual magnetic split-ring resonators.* Nature Photon., 2008. 2: p. 614-617.

134. A. K. Azad, Y. Zhao, W. Zhang, M. He, *Effect of dielectric properties of metals on terahertz transmission in subwavelength hole arrays.* Opt. Lett., 2006. 31: p. 2637-2639.

135. R. Marques, F. Mesa, J. Martel, F. Medina, *Comparative Analysis of Edge- and Broadside-Coupled Split Ring Resonators for Metamaterial Design—Theory and Experiments.* IEEE Trans. Antennas Propag., 2003. 51: p. 2572-2581.

136. K. B. Alici, A. Serebryannikov, E. Ozbay, *Photonic magnetic metamaterial basics.* Photonics Nanostruct., 2010. accepted: p. doi:10.1016/j.photonics.2010.07.005.

Appendix A

Publications in SCI Journals

23. Kamil Boratay Alici, Ekmel Ozbay, "*Optical magnetic resonance enhanced composite metamaterial absorber for solar, stealth, thermal isolation, photo-detector, and biosensor applications*" **submitted** (2010).

22. Kamil Boratay Alici, Filiberto Bilotti, Mehmet Deniz Caliskan, Lucio Vegni, Ekmel Ozbay, "*Experimental verification of metamaterial loaded, small, circular patch antennas*," **submitted** (2010).

21. Kamil Boratay Alici, Filiberto Bilotti, Lucio Vegni, Ekmel Ozbay, "*Experimental verification of metamaterial based electrically thin microwave absorbers*," Journal of Applied Physics, **accepted** (2010).

20. Kamil Boratay Alici, Andriy E. Serebryannikov, Ekmel Ozbay, "*Photonic Magnetic Metamaterial Basics,*" Photonics and Nanostructures – Fundamentals and Applications, **accepted** doi:10.1016/j.photonics.2010.07.005 (2010).

19. Zhaofeng Li, Rongkuo Zhao, Thomas Koschny, Maria Kafesaki, Kamil Boratay Alici, Evrim Colak, Humeyra Caglayan, Ekmel Ozbay and Costas Marcus Soukoulis, *"Chiral metamaterials with negative refractive index based on Four-U-SRRs,"* Applied Physics Letters, Vol. 97, 081901 (2010).

18. Kamil Boratay Alici, Ekmel Ozbay, "*Metamaterial inspired enhanced far field transmission through a subwavelength nano-hole,*" Physica Solidi Status - Rapid Research Letters, **accepted** doi: 10.1002/pssr.201004129 (2010).

17. Filiberto Bilotti, Alessandro Toscano, Kamil Boratay Alici, Ekmel Ozbay, Lucio Vegni, "*Design of miniaturized narrowband absorbers based on resonant magnetic inclusions*," IEEE Transactions on Electromagnetic Compatibility, **accepted**, (2010).

16. Kamil Boratay Alici, Andriy E. Serebryannikov, Ekmel Ozbay, *"Radiation properties and coupling analysis of a metamaterial based, dual polarization, dual band, multiple split ring resonator antenna*," Journal of Electromagnetic Waves and Applications, **Vol. 24**, 1183-1193 (2010).

15. Kamil Boratay Alici, Ekmel Ozbay, "*Theoretical study and experimental realization of a low-loss metamaterial operating at the millimeter-wave regime: Demonstrations of flat and prism shaped samples,*" IEEE Journal of Selected Topics in Quantum Electronics, **Vol. 16**, 386-393 (2010).

14. Kamil Boratay Alici, Ekmel Ozbay, "*Direct observation of negative refraction at the millimeter-wave regime by using a flat composite metamaterial*," Journal of the Optical Society of America B, **Vol. 26**, 1688-1692 (2009).

13. Kamil Boratay Alici, Ekmel Ozbay, "*Oblique response of a split-ring-resonator-based*
left-handed metamaterial slab," Optics Letters, **Vol. 34**, 2294-2296 (2009).

12. Kamil Boratay Alici, Filiberto Bilotti, Lucio Vegni, Ekmel Ozbay, "*Optimization and tunability of deep subwavelength resonators for metamaterial applications: complete enhanced transmission through a subwavelength aperture,*" Optics Express, **Vol. 17**, 5933 - 5943 (2009).

11. *Kamil Boratay Alici, Ekmel Ozbay, "Low-temperature behavior of magnetic metamaterial elements,"* New Journal of Physics, ***Vol. 11****, pp. 043015(1-8) (2009).*

10. Zhaofeng Li, Kamil Boratay Alici, Humeyra Caglayan, Ekmel Ozbay, "Generation of a non-diffractive Bessel beam from a metallic subwavelength aperture," Physical Review Letters, **Vol. 102**, pp. 143901(1)-143901(4) (2009).

09. Kamil Boratay Alici, Ekmel Ozbay, "*Characterization and tilted response of a fishnet metamaterial operating at 100 GHz*," Journal of Physics D: Applied Physics, **Vol. 41**, 135011 (2008).

08. Kamil Boratay Alici, Ekmel Ozbay, "*A Planar Metamaterial: Polarization independent fishnet structure*," Photonics and Nanostructures – Fundamentals and Applications, **Vol. 6**, pp. 102-107 (2008).

07. Filiberto Bilotti, Alessandro Toscano, Lucio Vegni, Koray Aydin, Kamil Boratay Alici, and Ekmel Ozbay, "*Equivalent-Circuit Models for the Design of Metamaterials Based on Artificial Magnetic Inclusions*," IEEE Transactions on Microwave Theory and Techniques, **Vol 55**, No. 12, pp. 2865-2873 (2007).

06. Kamil Boratay Alici**,** Filiberto Bilotti, Lucio Vegni, Ekmel Ozbay, "*Miniaturized negative permeability materials,"* Applied Physics Letters, **Vol. 91**, 071121 (2007).

05. Kamil Boratay Alici**,** Ekmel Ozbay, "*Electrically small split ring resonator antennas*," Journal of Applied Physics, **Vol. 101**, 083104 (2007).

04. Kamil Boratay Alici, Ekmel Ozbay, "*Radiation properties of a split ring resonator and monopole composite*," Physica Status Solidi B, **Vol. 244**, No. 4, pp. 1192-1196 (2007).

03. Ekmel Ozbay, Irfan Bulu, Koray Aydin, Humeyra Caglayan, Kamil Boratay Alici, and Kaan Guven, "*Highly Directive Radiation and Negative Refraction Using Photonic Crystals*," Laser Physics Journal, **Vol. 15**, No. 2, pp. 217-224 (2005).

02. Ekmel Ozbay, Kaan Guven, Ertugrul Cubukcu, Koray Aydin and Kamil Boratay Alici, "*Negative refraction and subwavelength focusing using photonic crystals*," Modern Physics Letters B, **Vol. 18**, No. 25, pp. 1275-1291 (2004).

01. Kaan Guven, Koray Aydin, Kamil Boratay Alici, Costas. M. Soukoulis, and Ekmel Ozbay, "*Spectral negative refraction and focusing analysis of a two-dimensional left-handed photonic crystal lens*," Physical Review B, **Vol. 70**, 205125 (2004).